DOCTOR OF ENGINEERING (ENGD)

Development of a Gait Simulator for Testing Lower Limb Prostheses

Yang, Zhanye

Award date:
2020

Awarding institution:
University of Bath

Development of a Gait Simulator for Testing Lower Limb Prostheses

Zhanye Yang

A thesis submitted for the degree of doctor of philosophy

University of Bath

Department of Mechanical Engineering

September 2019

Summary

There were 1.6 million people who suffered from limb loss in the U.S in 2005 alone. Amputation changes one's body function and life dramatically, especially lower limb losses. Prostheses can largely save the situation. Considerable effort is currently being expended on developing intelligent powered lower-limb prostheses. These prostheses require patient tuning and validation during the developing process. Present prosthesis testings are mainly based on amputees and prosthetists qualitative feedback, which is inconsistent and unsafe. It also limits the test conditions. Additionally, the recruitment of amputees is hard. This work seeks approaches to test lower limb prostheses to replace human testing.

An investigation of applying Hardware-in-the-Loop (HIL) on testing prostheses is presented. HIL testing has been used successfully for a number of years on a wide range of applications. A HIL testing system has groundbreaking potential in prostheses testing to investigate the nature of human learning of walking. However, any delay in a HIL system will cause the increase of energy. The stiff ground contact discontinuity is hard to compensate. We investigate the effect of introducing nonlinearity and discontinuity into a HIL system by comparing three types of Spring Mass System (SMS). Lead Compensation (LC) and Horiuchi Compensation (HC) are used and compared. It is concluded that the actuation system delay frequency should be 20 times greater than the system natural frequency in order to keep the system simulation stable, which is hard to realise.

Then a novel approach to test lower limb prostheses with the development of a Hydraulic Gait Simulator (HGS) and control strategy is presented. A gait simulator testing of lower-limb prostheses has the advantage of (i) removing humans from early-stage experimental testing (ii) gathering objective quantitative measurements and (iii) and permits the inspection of joint reaction forces (non-achievable without having instrumented joints in the amputees). The approach uses a leg robot with a prosthesis foot to achieve required Ground Reaction Force (GRF) of human use. The kinematics, kinetics of test prosthesis and the robot leg energy are used to evaluate the performance of the test prosthesis. It is the first robot-based lower limb prosthesis testing method that tests prostheses by generating walking gaits and performing a quantified evaluation. To address the GRF control, an Extended Iterative Learning Control (EILC) algorithm is derived. The process of achieving the required GRF can be seen as a learning process from a test prosthesis user. The algorithm is validated both in simulation and experiment. It is found effective on stationary ground, moving ground with passive ankle prostheses and active ankle prostheses. An example of testing a passive ankle prosthesis is presented in the end.

The HGS is controlled with the proposed EILC to replicate human walking GRF. Different settings of the prostheses are used. By analysing the generated gaits, the HGS has been proven to be able to identify small changes in the prosthesis. The prosthesis is observed to give insufficient power in the Powered Plantarflexion (PP) phase and this finding agrees with traditional human testing results, demonstrating the effectiveness of the proposed test approach in testing a lower leg prosthesis.

Acknowledgements

I would like to show my gratitude to my supervisors Dr.Pejman Iravani, Prof.Andrew Plummer and Dr.Min Pan, for their patient guidance and valuable advice without restraint.

Many thanks to the technician support team in 4E, 6E and 8E, especially Mr. Martin Naidu for helping me with test rig even though I am not from his department. Without their responsible work, this PhD work won't happen.

I would like to thank my friends in the UK for their company. No matter happy or sad times, I am glad to have you with me. Mr.Jerry Zheng, Mr. Jiaozi Deng have always been supportive. Appreciation also goes to Mr.Xavier Pellet and Mr.Harry Xu for listening to my complaints. I would like to thank Blackpink for inspiring and motivating me.

Lastly, Special thanks go out to my parents, my sisters and my granddad for their unlimited love and support.

Contents

List of Figures

List of Tables

Symbols and Abbreviations

F_1, F_2, F_3 Actuator measured force at base joint, hip joint and knee joint of the HGS.

θ_{m1}, θ_{m2}, θ_{m3} Measured angles at base joint, hip joint and knee joint of the HGS.

p_1 **to** p_6 Hydraulic system actuator chambers pressure.

A_p Piston side area of the actuator.

A_r Annulus side area of the actuator.

D_x Derivative gain for EILC in horizontal direction.

D_y Derivative gain for EILC in vertical direction.

E_n Spring Mass System normalised energy.

E Spring Mass System energy.

F_p Force in the piston side of the actuator .

F_r Force in the rod side of the actuator .

K_n Spring Mass System normalised stiffness.

K_x^* Horizontal foot stiffness diagonal matrix.

K_y^* Vertical foot stiffness diagonal matrix.

K Spring Mass System stiffness.

L_0 Spring Mass System natural length.

P_p Piston side chamber pressure of the actuator.

P_r Annulus side chamber pressure of the actuator.

P_x Proportional gain for EILC in horizontal direction.

P_y Proportional gain for EILC in vertical direction.

R_f Delay frequency and system natural frequency ratio of Spring Mass System.

$\mathbf{J_s}$ Jacobian matrix for two rotational joint space.

$\hat{F_{yj}}$ Vertical GRF vector during a cycle time.

$\hat{F_{yj}}$ Vertical GRF vector during a cycle time.

$\hat{e_x}$ Horizontal force error vector after a cycle.

$\hat{e_y}$ Vertical force error vector after a cycle.

$u\hat{_{\theta 2}}$ Joint space hip command vector for a cycle.

$u\hat{_{\theta 3}}$ Joint space knee command vector for a cycle.

$\hat{u}_{xj}$ Horizontal command in global coordinates for a cycle.

$\hat{u}_{yj}$ Vertical command in global coordinates for a cycle.

f_n System natural delay frequency of Spring Mass System.

k_x^* Horizontal time varying stiffness of a test prosthesis foot in a ground contact.

k_y^* Vertical time varying stiffness of a test prosthesis foot in a ground contact.

p_r Hydraulic system return pressure.

p_s Hydraulic system supply pressure.

p_{max} Maximum pressure of the hydraulic system .

BSP British Stardand Pipe.

BW body weight.

CD Controlled Dorsiflexion.

CP Controlled Plantarflexsion.

DF Dorsiflexion.

EILC Extended Iterative Learning Control.

FDA Forward Dynamic Approach.

GRF Ground Reaction Force.

HA Hybrid Approach.

HC Horiuchi Compensation.

HGS Hydraulic Gait Simulator.

HIL Hardware-in-the-Loop.

IAA Initial Ankle Angle.

IDA Inverse Dynamic Approach.

ILC Iterative Learning Control.

LC Lead Compensation.

LCSMS Linear, Continuous Spring Mass System.

NCSMS Nonlinear, Continuous Spring Mass System.

NSSMS Nonlinear, Stiff Spring Mass System.

PDW Passive Dynamic Walker.

PP Powered Plantarflexion.

SLIP Spring Loaded Inverted Pendulum.

SMS Spring Mass System.

Chapter 1

Introduction

1.1 Motivation

According to the previous research, there were 1.6 million people who suffered from limb loss in the U.S in 2005, and this number will increase to 3.6 million by 2050 [1]. Amputation changes people's body function and life quality dramatically. There are more lower limb amputations than upper limb amputations [1]. Losing lower limb is even worse because lower limb losses causes more pain, less energy and more physical disabilities [2]. The independency of life is heavily influenced. Using prostheses is one of the most important factors to maintain the quality of life for lower limb amputees [3].

In this research, I focused on lower limb prostheses. First mentioning lower limb prosthesis, one can think of the old time classic one leg pirate image. The wooden leg of a pirate could be the simplest lower limb prosthesis. However, based on the amputation level, lower limbs losses can be categorised into toe, transmetatarsal (TMA), mid-foot, below-knee (transtibial) and above-knee (transfemoral) amputations [4]. Each type of amputation requires very different size, weight, shape and function of prostheses. This means a wood stick or a unified device is not able to cover all the cases. The design and testing of these prostheses requires different types of amputees to participate, the recruitment of which is sometimes difficult.

Considerable effort is currently being expended on developing lower-limb prostheses. From the actuation point of view, the focus of developing prostheses is gradually shifting from passive elastic prosthetic foot to semi-active and active prosthesis. Active prostheses of various types of actuation have been documented in recent years. For example, electrically driven active ankles [5], [6], pneumatically driven trans-femoral prostheses [7] and a hydraulically driven active ankle [8], [9]. Control strategy design is an important part of active prosthesis development. Gradually increased control complexity makes verification and testing become more time consuming.

Current lower-limb and ankle prosthesis testing standards mainly examine material fatigue, strength and joint reliability [10], [11]. Tests are limited to focus only on mechanical properties of a prosthesis. Apart from the mentioned testing standards, developing and testing prostheses largely relies on model-based testing

[12] or human-based testing [9], [13]. Due to the lack of amputee volunteers, some modified prostheses were designed to be used by able-body human [7], [14]. Normal developing process goes from modelling to human test. For model-based testing, it is often questioned of its fidelity. Validation on human-based testing is not avoidable. For human test, the biggest problem is the lack of amputee volunteers. A developing prototype could hurt a user due to a careless mistake in a controller. The shortcomings of the human test is summarised as follows:

- Limited testing time or samples: it is hard to find participants to test prostheses
- Safety of participants: a prototype prosthesis has potential to cause injury of its user
- Limited test environments: indoor tests may not allow various test conditions: e.g. walking on rough terrain
- Lack of objectivity and repeatability: It is hard for participants to provide consistent feedback

In summary, there are some drawbacks in both model-based testing and human-based testing. Developing a gait simulator to test lower limb prostheses is very beneficial. It can remove human participants in the early stage of developing a prosthesis which can speed up the development of a product. For the choice of actuation type, hydraulic actuation system is famous for its quick response and high energy density. It is suitable for a gait simulator which is required to achieve human leg motions and apply loads that are representative of human use.

1.2 Aims and objectives

Under the background of lacking effective methods to test lower limb prostheses physically to replace human-based testing, I propose a research question of **Can I test a lower leg prosthesis with a robot and replace human-based testing?** This PhD research is proposed to investigate and develop a hydraulic gait simulator that can help testing lower limb prostheses. The detailed objectives are as follows:

- Review current lower limb prostheses testing methods
- Investigate Hardware-in-the-Loop (HIL) approach of testing prosthesis, identify the main challenges
- Investigate and develop methods to test a lower limb prosthesis
- Build a hydraulic gait simulator to test lower limb prostheses
- Achieve Ground Reaction Force (GRF) control of the robot walking on a treadmill
- Model the gait simulator rig and simulate proposed methods
- Perform experimental tests on a lower limb prosthesis with different settings

1.3 Research Methodology

In this section, the research methodology is explained. In Figure 1.1, a flow chart to summarise the research methodology is presented.

To achieve the goal of the research, firstly the literature is reviewed and the gap is identified. No systematic testing methods especially in robot-based testing category were found in the literature. However, the existing lower limb prostheses test rigs have provided ideas of designing the robotic test platform. Then possible test methods are investigated. HIL testing of the prosthesis is investigated and found not feasible. In another approach, the robot leg is required to generate a walking gait. Three possible methods to generate a walking gait are compared. The method to generate a gait by achieving the required ground reaction force with human walking is selected. The test rig requires GRF control in both vertical and anterior force control. Iterative learning control is applied to achieve the GRF control. The generated robot gait can be analysed in the end. A simulated test rig is built and the proposed ILC is tested. In the end, a case study of testing a prosthesis is carried out.

1.4 Structure of the thesis

Chapter 2 presents a review of literature related to lower limb prosthesis testing. Biomechanics of walking is first reviewed to give a basic understanding of human gaits and amputee gaits. Prostheses testing methods are examined. The limitations of the current work are identified.

Chapter 3 presents an investigation of applying Hardware-in-the-Loop to test prostheses. The Horiuchi Compensation (HC) and Lead Compensation (LC) are used to compensate three types of Spring Mass System (SMS) with delays. System stability is discussed.

Chapter 4 presents a new method to test lower limb prostheses with a gait simulator robot. The GRF control is addressed with an Extended Iterative Learning Control (EILC). The converge criterion of the method is analysed.

Chapter 5 presents the detailed description of the Hydraulic Gait Simulator (HGS). It includes an overview and components selection. Furthermore, the EILC implementation and the HGS state machine is introduced.

Chapter 6 describes the modelling process of the HGS. It consists of mechanical system, hydraulic system and controller. Also, the modelling of the ground contact is illustrated.

Chapter 7 presents the validation of the model first. Then, the EILC is tested with the model with both stationary and moving ground.

Chapter 8 presents the experimental result of applying the EILC on GRF. The EILC is tested with HGS on both stationary and moving ground. In the end, an example of testing a passive prosthesis is presented.

Chapter 9 presents the conclusions of the research. Possible future work is described.

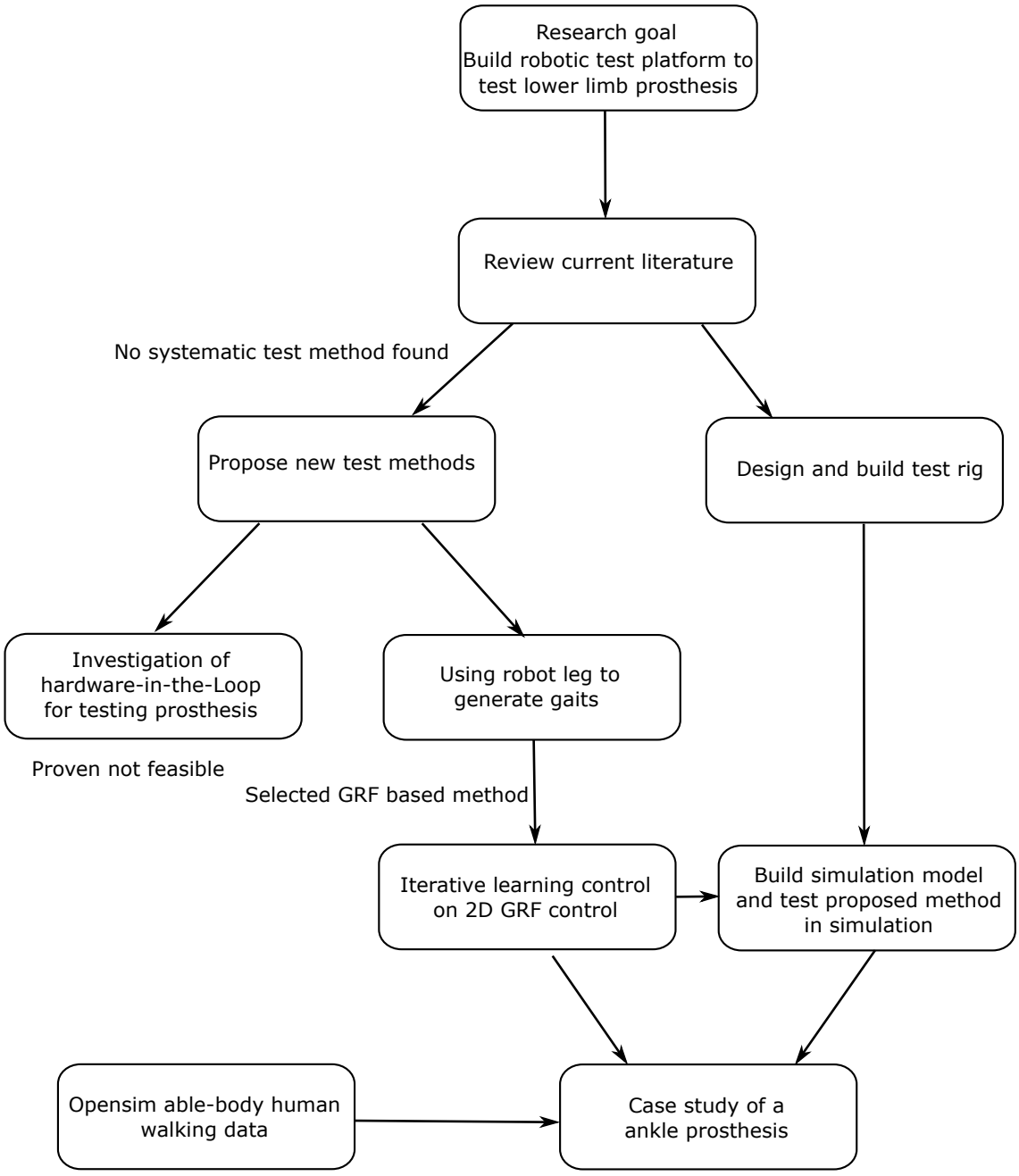

Figure 1.1: Research path.

Chapter 2

Literature Review

This chapter reviews the literature related to lower limb prostheses testings. The first section reviews human walking biomechanics to give a general foundation of our research. It includes basic definition of human walking gait, kinematics and kinetics of human walking gait and amputee walking gait. The review in the second section is about current lower limb prostheses testings. It includes model-based testing, human-based testing and testing robots.

A brief conclusion remark is given at the end of this chapter.

2.1 Biomechanics of Human walking/Running

In order to design and build a gait simulator, it is necessary to first understand normal gait. Normal is defined as a general full body function adult and it ignores differences like different sex and age. By analysing the kinetics and kinematics of human walking, it helps us to determine basic parameters of building a prosthesis testing platform, like power level of walking and running, gait speed and body lengths.

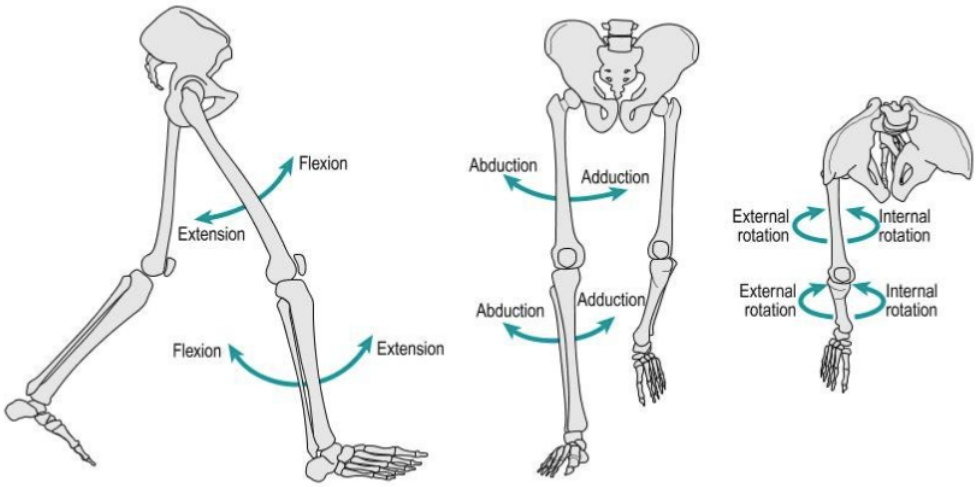

Figure 2.1: Motion definitions of a lower extremity. [15]

The motion definition of a human leg is defined in Figure 2.1. For a hip moving upwards closer to stomach is called flexion, the other direction is defined as extension. For a knee to move forwards toe is called extension and the opposite direction is called flexion. In an ankle motion, bending the front toe towards lower leg is called dorsiflexion and the opposite direction is defined as plantar flexion, see Figure 2.2.

2.1.1 Basic concepts of human walking

Human walking is a complicated motion which involves neural control and muscle actuation. However, it is a periodic motion so that an analysis can be simplified to focus on one cycle of a walking gait. A widely accepted cycle definition defines walking cycle as start with the heel strike of one foot and end at the next heel strike of the same foot [15].

A diagram of detailed phases division is shown in Figure 2.3:

Normal walking is approximately symmetric, thus I can focus on one leg. In order to compare gaits regardless of the length of a stride, human gait is commonly described in percentage of a full stride. Focus on the right foot, showed as Figure 2.3, the cycle starts from a heel strike and ends at the nest heel strike. 0% to 10% and 50% to 60% are double support phase. The rest of the cycle is single supported. Stance phase is slightly longer than 60% and swing phase is slightly shorter than 40%. It is consistent with [15], [17]. However, as speed increases, the swing phase is

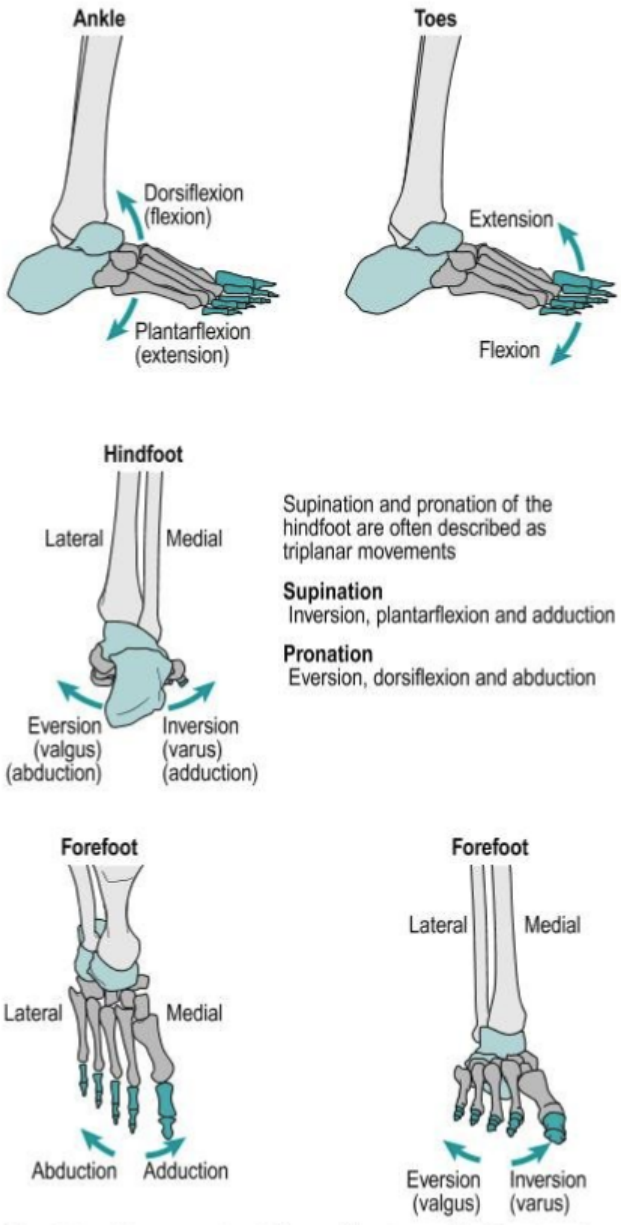

Figure 2.2: Motion definitions of foot [15].

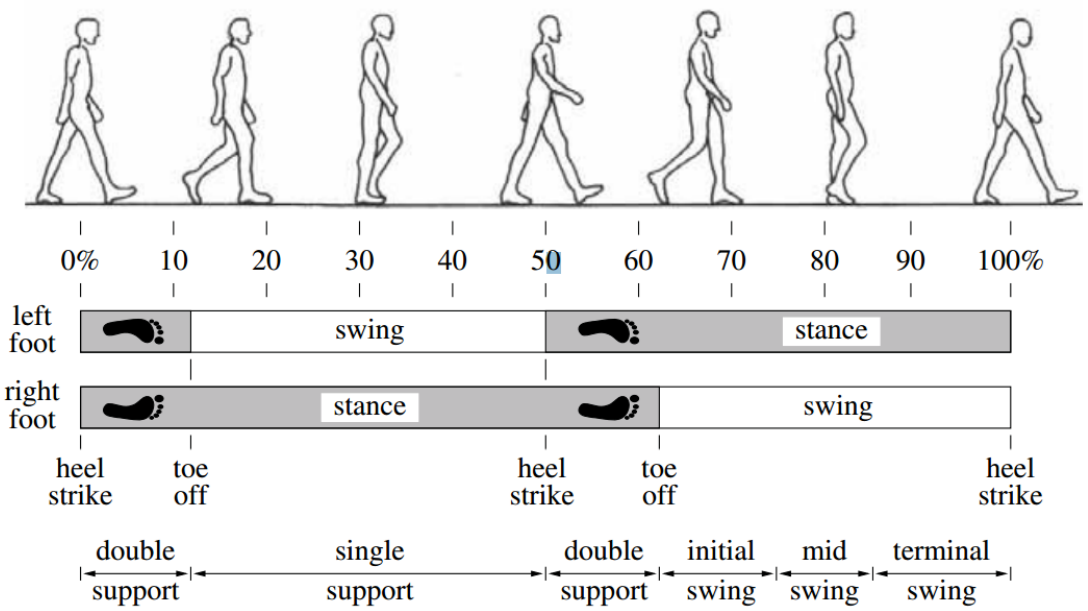

Figure 2.3: Phases of human walking gait [16].

proportionally longer and stance phase is shorter [18]. If the speed further increases, walking can transit to running, it happens from 1.3 to 2.5 m/s based on leg length [19]. Once the transition happens, a cycle can be divided into flight phase and stance phase.

Based on the research from David et al.a walking cycle can be further separated into seven events [15]:

1. Initial contact
2. Opposite Toe off
3. Heel rise
4. Opposite initial contact
5. Toe off
6. Feet adjacent
7. Tibia vertical

These events separate the gait period into seven periods. The stance phase is divided into four parts: Loading response, Mid-stance, Terminal stance and Pre-swing. The swing phase can be seperated into three parts: Initial swing, Mid-swing and Terminal swing. Detailed hip, knee and ankle motions can be found in [15].

From ankle motion perspective, stance phase can be divided into three subsections that happen during four key positions which is shown in 2.5.

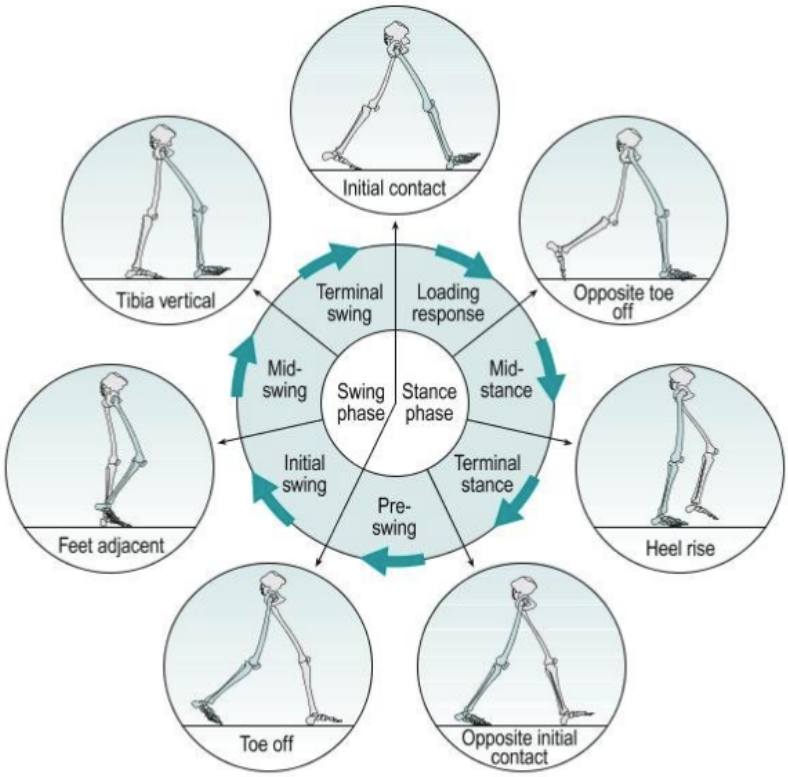

Figure 2.4: Subsections and key positions of a walking gait [15].

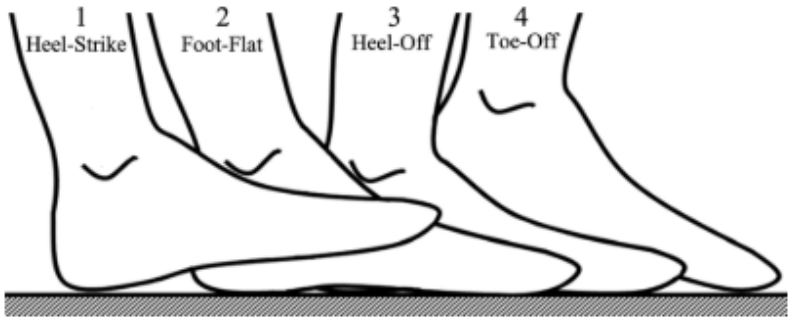

Figure 2.5: Ankle key positions during a stance phase [20].

The stance phase can be divided by these four key positions into three subsections: Controlled Plantarflexsion (CP), Controlled Dorsiflexion (CD) and Powered Plantarflexion (PP). These three subsections of a natural gait are described as below:

- Controlled Plantarflexsion (CP): This subsection starts at *Heel-Strike* and ends at *Foot-Flat*. During this phase, the foot rotates from neutral position to maximum plantar flexion. The body is slowed down and stabilized.
- Controlled Dorsiflexion (CD): This subsection at *Foot-Flat* and ends at *Heel-Off*. During this phase, the foot moves from maximum plantar flexion position to maximum dorsi flexion position. The shank rotates around the ankle joint.
- Powered Plantarflexion (PP): This subsection starts after the heel lefts ground. The ankle starts plantarflexion and propels the body to move forward.

2.1.2 Quantitative analysis of walking gait

Quantitative gait analysis has been proved to be useful in identifying normal and pathological gait. The prescription of treatment to pathological gait also benefits from quantitative gait analysis [17]. Many researchers contributed to the lower extremity kinematics with quantitative gait analysis[17], [21]–[23]. They applied various approach to data sampling, for example, Chao used electrogoniometers to get the joint rotation [21]. Interrupted light photography was used to get the motion by monitoring reflective markers[22]. A VICON (computer-aided video motion analysis system) was used to get the kinematic data of human by M.P. Kadaba[17]. S.Slajpah et al.proposed model-based extended Kalman filter for human walking motion assessment with IMUs, as a low cost motion capture system[24].

Overall quantitative data

Table 2.1: Overall quantitative data of human walking [17]

Parameter	Units	Young Men ($N = 20$)	Young Women ($N = 12$)
Cadence	steps/min	112 ± 9	115 ± 9
Velocity	m/s	1.34 ± 0.22	1.27 ± 0.16
Stride time	s	1.08 ± 0.08	1.05 ± 0.08
Step time	s	0.56 ± 0.02	0.53 ± 0.06
Stride length	m	1.41 ± 0.14	1.3 ± 0.1

A general results summary from [17] is showed in Table 2.1. From the table above, human walking speed is around $1.3\,m/s$, stride time is about $1\,s$. These two data can be a good starting point for setting parameters of walking simulation and gait simulator robot modelling. The average velocity and stride length of men are about 5 % larger than women. It means the statues might influence cadence, walking speed and stride length. Some methods of normalisation were proposed, such as

stride length divided by *leg length* [25] and some spatial-temporal research[26], [27]. For different self-select speed of walking, a walk ratio was defined using *cadence* divided by *stride length* [28], which is a speed-independent index of walking patterns.

Kinematics

Kinematics is defined as the study of movements without respect to the forces. There is large amount of literature about it. In Figure 2.6, a measured walking kinematics from Kadaba et al. [17] is shown.

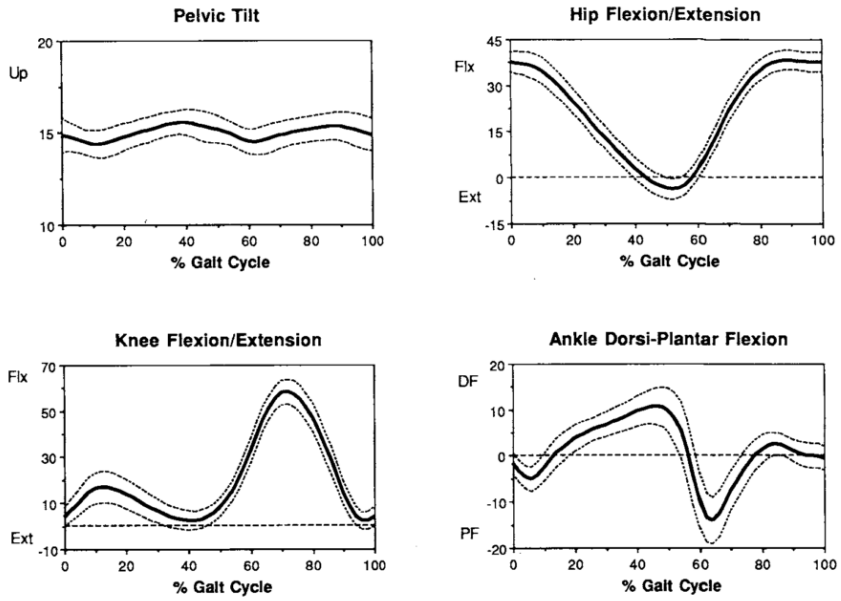

Figure 2.6: Sagittal plane angles of pelvic, hip, knee, ankle of human walking [17]. The black line is the mean average of the measured value. The dotted lines are measured value with one standard deviation.

Some other researchers have also done work on gait data analysis of lower limb kinematic analysis of human level walking. Due to different definitions of the co-ordinates, absolute values of angles cannot be compared. But the ranges of joints motion can be used to verify each other. In Table 2.2, two research groups derived similar results.

Kinetics

Kinetics is defined as studying the joint moment, power and work. It is normally worked out from an inverse dynamics approach [29]. It requires ground reaction force measurement from a force plate, which is also called external forces. It also needs measured kinematics data and estimated body segment inertial parameters. With these data, joint moments and powers for the hip, knee, and ankle can be computed.

Table 2.2: Comparison of lower limb kinematics from two different research groups (Unit: degree).

Authors	Kadaba et al.(1990)[17]	Riener et al.(2002)[23]
Method	VICON	ELITE camera-based analyser
Hip	42	41
Knee	54	52
Ankle	26	25

In Figure 2.7, hip, knee and ankle joint moment of sagittal plane is shown. The largest moment is observed in ankle during terminal stance. Although the moments in three joints varies, support moment MS coined by Winter [30] shows a much simpler variable to represent a different motion. With faster walking speed or running speed, the support moment is larger. A revised model was proposed by Hof [31]:

$$MS = 1/2MH + MK + 1/2MA$$

where, MH, MK and MA represent hip, knee and ankle moments respectively.

In Figure 2.7, hip knee and ankle joint power of level walk is presented. It is one can see that the largest power spike happens at the *Pre-swing*, which is also referred as *push-off* phase, which is almost 4 times than the amplitude of other joints. Ankle plays an important role of assisting a human body to propel forward.

Ground reaction force (GRF)

Figure 2.8 shows a typical GRF of human walking at speed of $4\,km/h$. In sagittal plane, the vertical force has two upwards peaks and anteroposterior force has two peaks in two directions.

2.1.3 Stair ascent and descent

Walking upstairs and downstairs were researched in [23], [33], [34]. These research showed similar results. It is clear that human has different kinematic patterns of stair ascent and descent compared to level walking. The results show that hip, knee and ankle flexion are all increased in ascent. In stair decent test, knee and ankle joint range is increased while only hip joint range is reduced. A comparison is shown in Figure 2.9.

From Figure 2.10, one can see that: The joints moment patterns and ranges are different in ascent, descent and level walking. Maximum hip extension moment of level walking is larger than ascent and descent. However, for the knee extension moment, the extension moment is much higher in descent and ascent. Together with

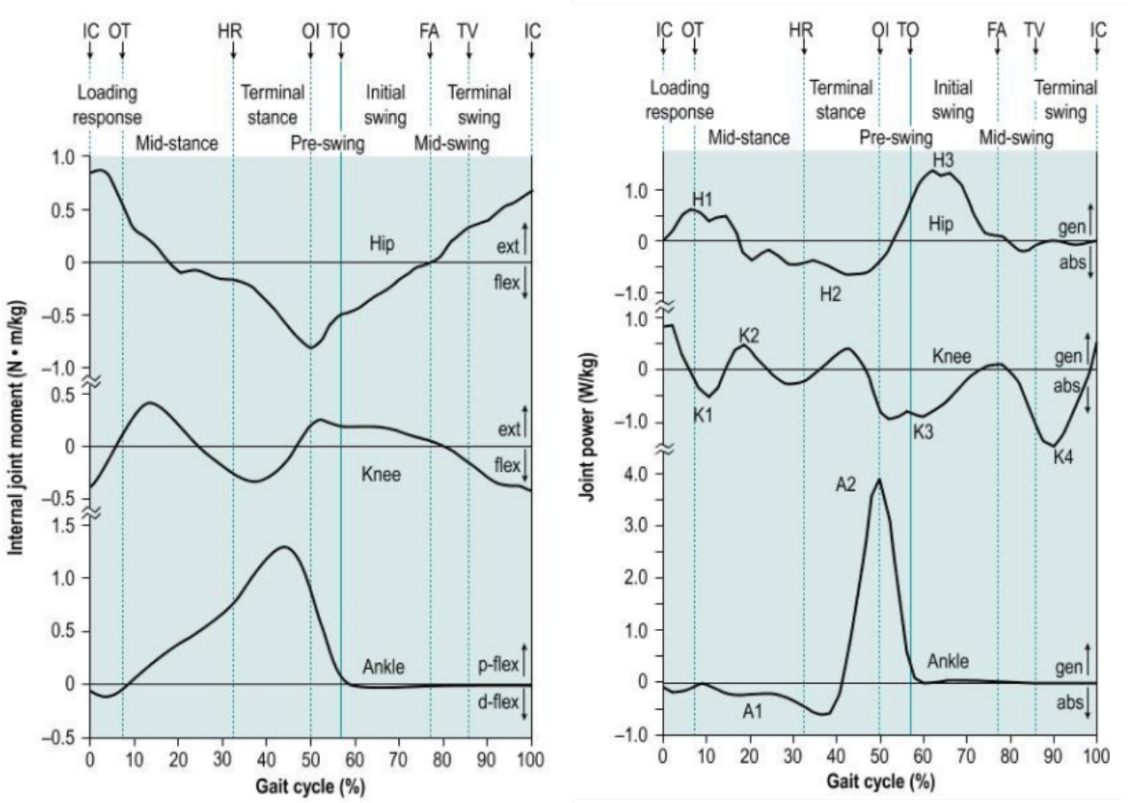

Figure 2.7: Sagittal plane joint moment and moment of hip, knee and ankle [15]. Moment power data is normalised with body weight.

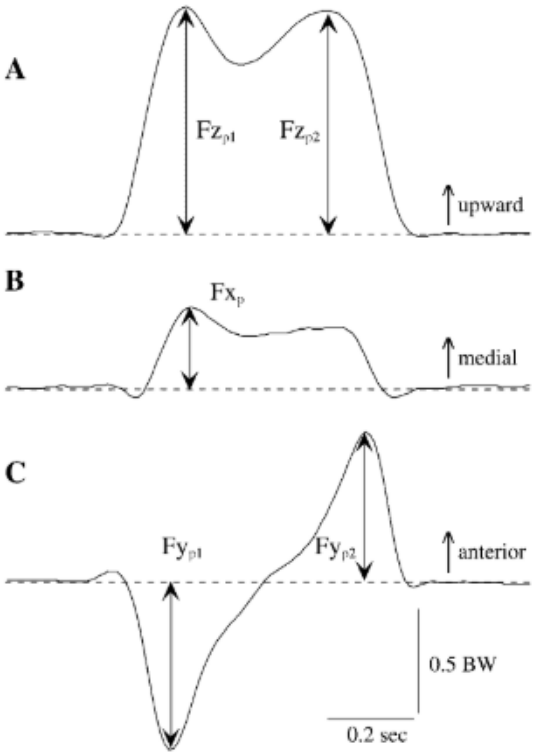

Figure 2.8: Sagittal plane GRF from literature [32]. A is vertical force, B is mediolateral force, C is anteroposterior force. The vertical bar is half body weight (BW), horizontal bar is $0.2\,s$.

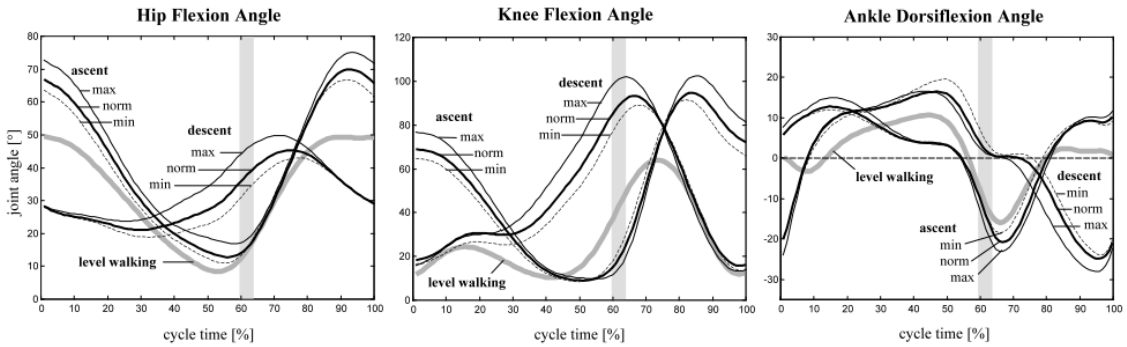

Figure 2.9: Sagittal plane angles of pelvic, hip, knee, ankle of human level walking, ascent and descent [23].

higher knee joint force measured in stair descent [35], it might explain why walk downhill often causes knee pain. As for the ankle plantarflexion moment, landing phase moment is larger in descent, push-off phase moment is larger in ascent, the level walking maximum moment is larger than descent and ascent.

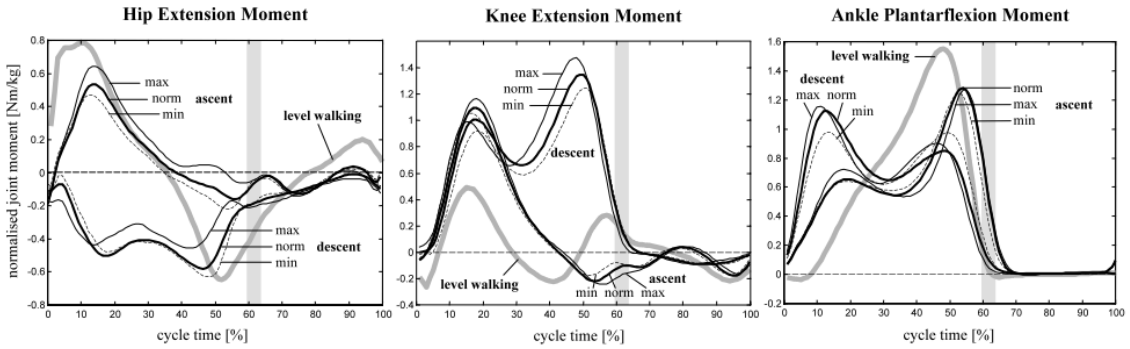

Figure 2.10: Joints moment of level walking, ascent and descent [23]. 0% stands for heel strike, 100% is the next heel strike.

During ascent, all the joints produce energy. For the hip joint, a small peak can be observed in the swing phase. It requires large power input for knee joint in the early stance phase and power input for ankle joint in the late stance phase. During descent, most negative power is observed, which means energy of body is absorbed. Hence, amputees with passive lower leg prosthesis feel it tiring to level walking and ascent, especially ascent because both knee and ankle needs to provide positive energy.

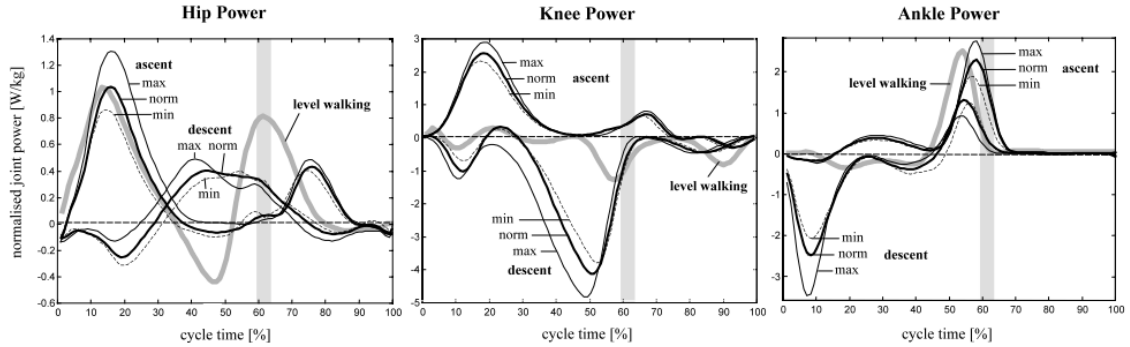

Figure 2.11: Joint power of level walking, ascent and descent [23]. 0% stands for heel strike, 100% is the next heel strike.

Ground reaction force (GRF)

Typical ground reaction force profiles are maintained similar patterns in three group of tests. However, one can see from Figure 2.12 that the descent walking has higher first peak and lower second peak in vertical ground reaction force. The ascent has slightly smaller vertical ground reaction force. As for anteroposterior force, the

second peak is smaller than it is in level walking. Mediolateral force is obvious larger in descent scenario.

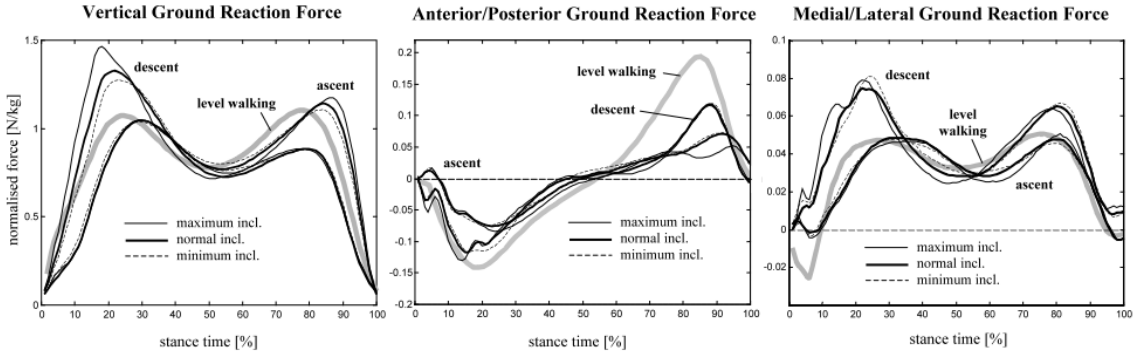

Figure 2.12: Ground reaction force of human level walking, ascent and descent. [23]. 0% stands for heel strike, 100% is the next heel strike.

2.1.4 Walking with prosthesis

Amputee walking gait with a lower extremity prosthesis is different from normal human gait. Many research have found that using a prosthetic ankle or knee for a unilateral amputee would cause an asymmetric gait pattern for both legs. With a passive foot, the foot is not able to provide enough power, especially in the PP phase. Since the the passive foot is not enough provide enough power, amputees tends to put more weight on the intact leg. Amputees usually prolong the period of propulsive force production in the non-afftected limb [36]. The non-afftected limb usually has more moment experienced at hip and knee joints and higher GRF [37], [38]. The prosthesis leg has less knee moment and GRF[36], [38], [39]. On the contrary, advanced prosthetic components were proven to positively influence the temporal and loading symmetry. Most experiment participants were found to prefer the prosthesis to improve the loading symmetry in [40].

In figure 2.13, sound leg joint moments are shown, one can see all three joint moments have different patterns and also the peak moments are increased compare to a non-amputee when a prosthesis foot is used.

Research on the sound leg for a prosthesis user provides important information on the performance of a prosthetic feet[41]. Better designed prosthesis leg would be able to reduce the intact leg joint moment and ground reaction force so that a balanced gait can be better achieved. In figure 2.14, GRF and external adduction moment of the sound leg is shown. Three groups of test results are shown, which are active prosthesis user, passive-elastic ankle prosthesis user and non-amputee. For the intact leg, the ground reaction force in the prosthesis groups is larger than the non-amputee group. As the walking speed increases, the increase on the GRF is clearer to see. The active prosthesis group has less ground reaction force and external adduction knee moment than the passive prosthesis.

More range in the prosthesis is reported to reduce the sound leg joint moments [43]. Active prosthesis foot is also found to be useful to reduce GRF and knee

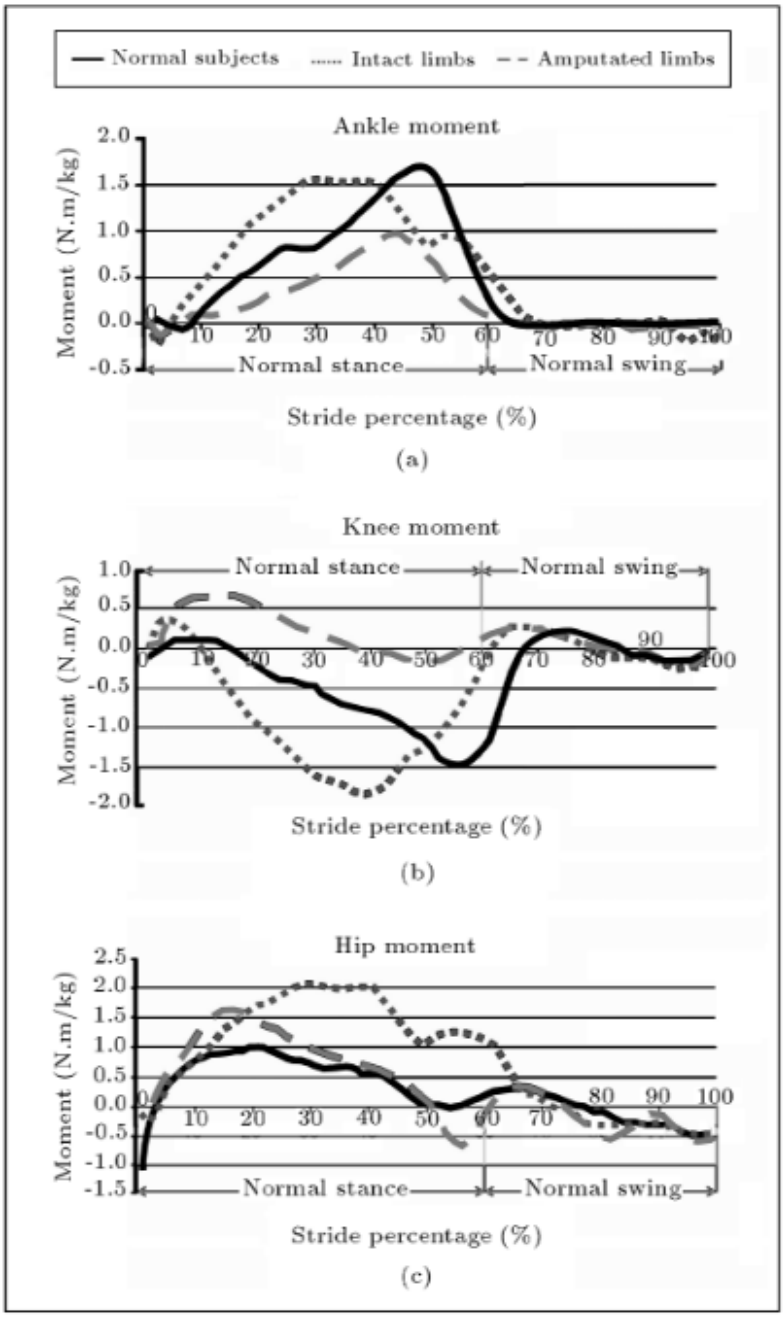

Figure 2.13: Variation patterns of the mean ankle (a), knee (b) and hip (c) joint net moments for normal subjects and intact and prosthetic limbs of amputee subjects [37].

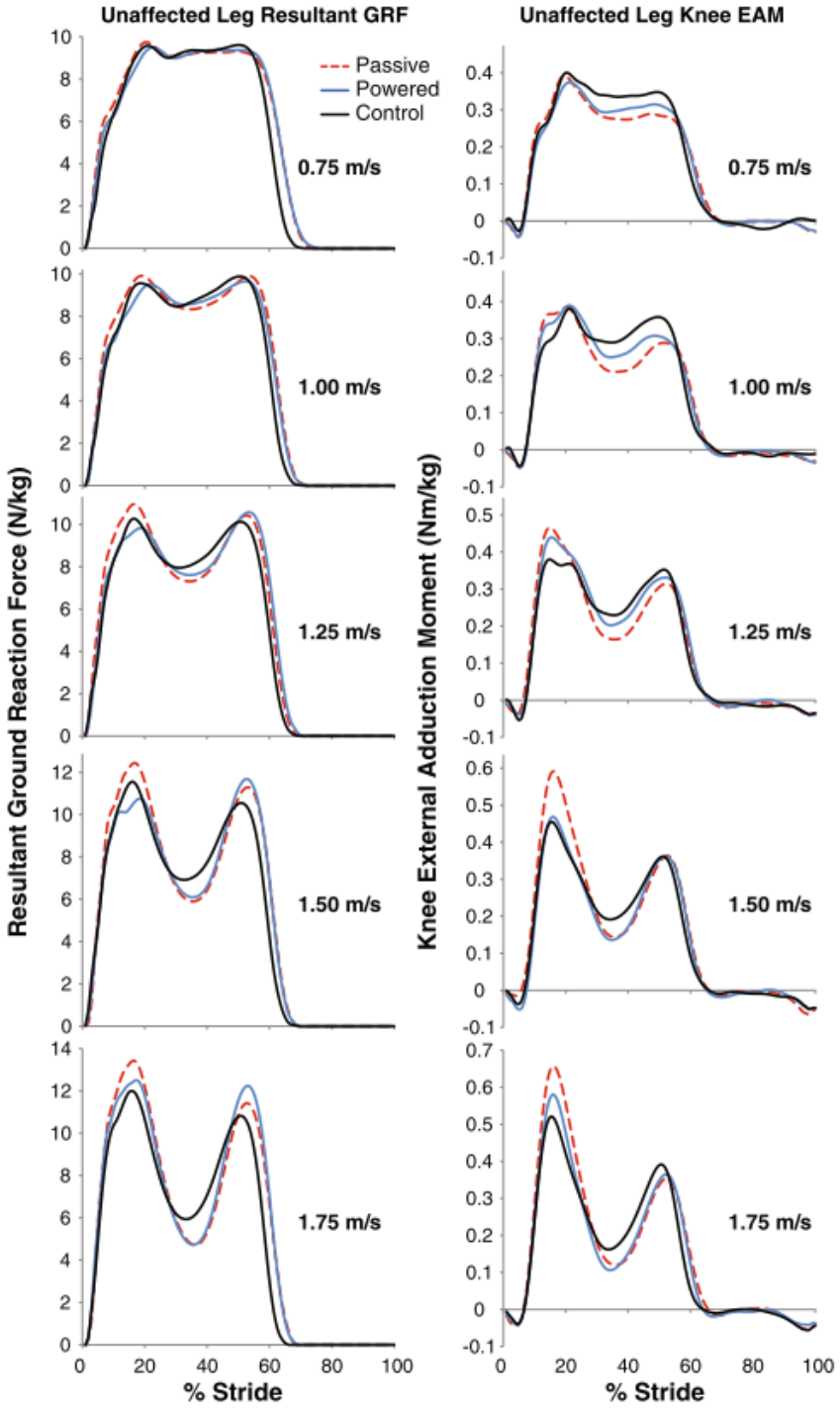

Figure 2.14: Average unaffected leg resultant ground reaction force (GRF) and knee external adduction moment for different walking speed from $0.75\,m/s$ to $1.75\,m/s$ [42]. Blue represents amputee with active prosthesis, black is non-amputee and red dashed line is passive-elastic ankle prosthesis.

moment of the non-affected limb [42]. Apart from that, research has proved that using an active prosthesis can decrease metabolic cost of walking and also increase the preferred velocity of walking [44]. The metabolic cost can be worked out experimentally from oxygen consumption and carbon dioxide production. It is used to estimate individuals' motion energy expenditure. The metabolic power calculation is shown in Subsection 2.2.1. In Figure 2.15, normalised metabolic cost of transport and preferred velocity of different groups are presented. Normalised metabolic cost is calculated by dividing metabolic cost power with body weight and velocity. The preferred walking speed of bionic prosthesis is almost the same with non-amuputee.

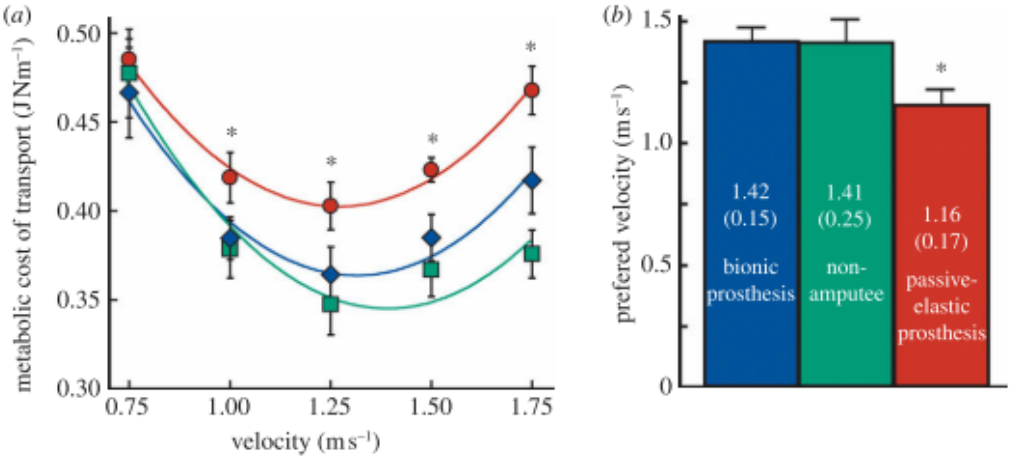

Figure 2.15: Gross metabolic cost of transport and preferred walking velocity [44]. Blue represents amputee with active prosthesis, green is nor non-amputee and red is passive ankle prosthesis.

2.2 Lower Limb Prostheses Testing

I classify the literature into three related topics. These topics are model-based testing, human-based testing and robot-based testing.

2.2.1 Model-based testing

Many research focus on the modelling of a human walking. Models serve the purpose of understanding the nature of human walking. Prosthesis design and testing benefits from these models. Some main stream models of human walking/running are introduced. The use of these walking model in testing prostheses are not much developed. Similar to [45], the models to simulate human walking can be summarised into different groups based on it complexity. Here, human walking model are classified into simplified mechanical models, dynamical model with net moment and dynamical model with muscles. I reviewed some work in these subclasses and its application on prosthesis testing or design.

Simplified Mechanical Model

One famous simplified type of model is the Spring Loaded Inverted Pendulum (SLIP) model. Despite the simplicity, the dynamics of the center of mass (CoM) during human walking and running are well demonstrated by this spring-based mechanics [46], [47]. With simple parameters like touch down angle, stiffness and energy level, a model can be fully described.

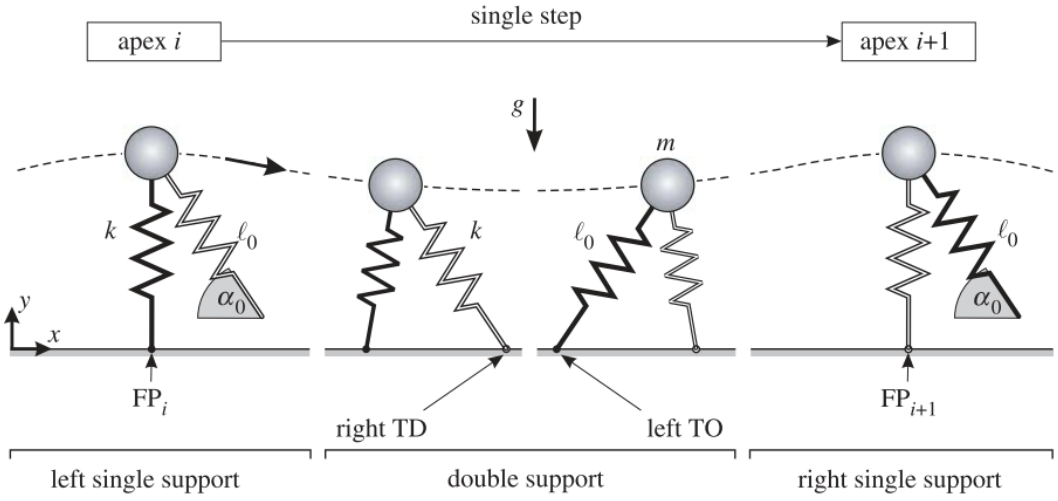

Figure 2.16: A typical SLIP walker from [46]. α_0 is touch down angle, l_0 is leg length at rest. m is the mass of the simulated body weight.

Spring-leg dynamics walking were observed for both the young and the older group with larger spring stiffness variations in older adult subjects group [48]. In [49], a compliant model with the accelerated pivot was proposed to emulate human forward progression of the center of pressure (CoP) during the stance phase. The horizantal GRF was found close to human data. A SLIP walker with foot were introduced in [50]–[52]. The SLIP walker with foot has shown allowed investigation on CoP making the model more consistent with human. A SLIP model was expanded with an off-centered curvy foot connected to the leg by a springy segment that emulates the asymmetric kinematics and kinetics of the ankle joint [51], [52]. Different from the centered foot in [50], lower limb ankle joint torque and kinematics were well described in the model.

With more complicated SLIP model like multi-joint configuration, the coordination of multi-joints can be understood. There is no work on a SLIP walker/runner with prostheses .This area could be explored more.

Another type of model is Passive Dynamic Walker (PDW) model. PDW was developed first in [53]. Once started on a shallow slope, this type of machine can settle in a steady gait quite comparable to human. In [54], a PDW model was modified to represent a unilateral transfemoral amputee. The asymmetricity was reduced when the knee location of the prosthesis was positioned below the intact knee by 36.7% of the total shank length.

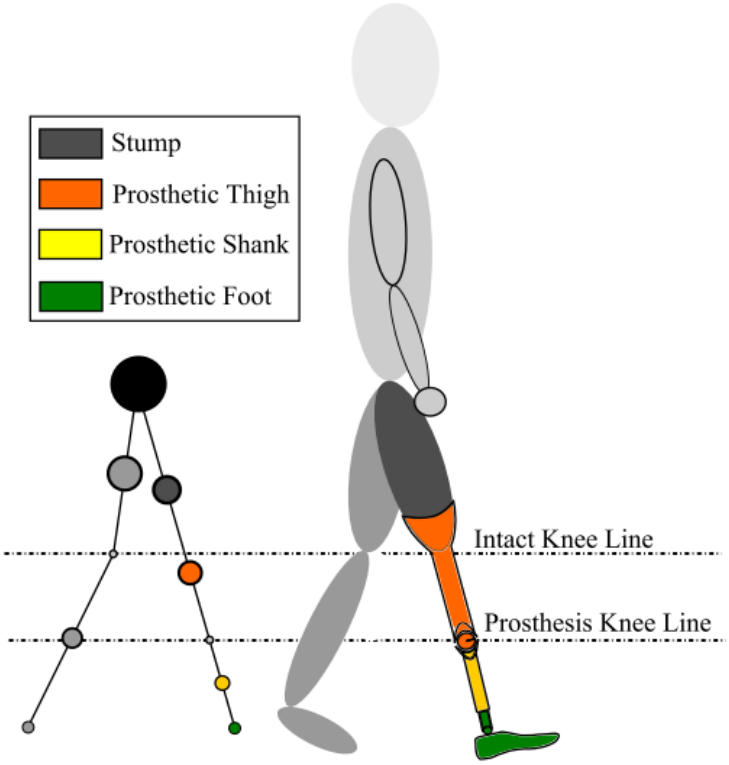

Figure 2.17: Asymmetric passive dynamic walker [54].

Dynamical models with net moment

In [55], Srinivasan et al. developed a forward-dynamic walking model. It was a hybrid model composed of models for single support (SS) and double support (DS) and transition from SS to DS model. In [56], Srinivasan model was adapted to simulate a transtibial prosthesis user. The kinematics of transtibial prosthesis walker is hypothesised to be the same for both leg. As a result, the kinetics are different. Joint power cost was used to compare the prosthesis alignment or design. The lower joint power cost is, the better alignment or design is.

Dynamical model with muscles

This type of model testing on lower limb prosthesis are much more complicated. Dynamical model with muscles refers to musculoskeletal models, where muscles are modelled on the origin and insertion points on a skeleton consisting of corrected bone geometry. The advantage of musculoskeletal models is that they can help understand the compensatory effect of individual muscles. In [12], a recent review of the design of musculoskeletal models used to optimise/analyse prosthesis design and control was carried out. In Figure 2.19, an example of skeletal model with muscles is given.

These models usually are forward dynamics simulation which gives potential to investigate how a prosthesis would influence a gait [12]. Mostly, muscles were mod-

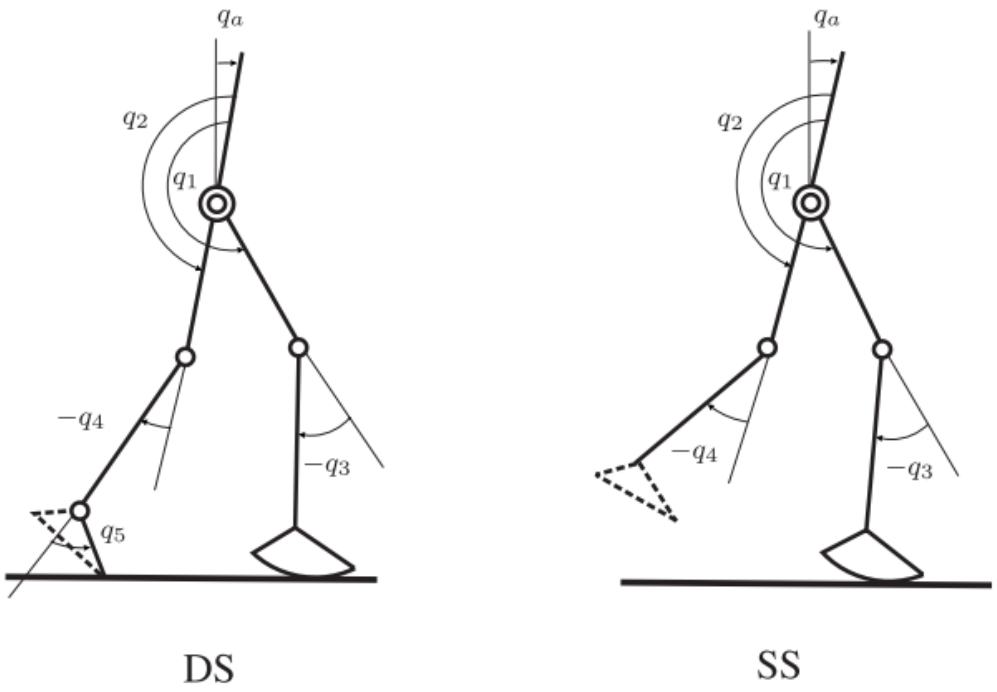

Figure 2.18: Srinivasan forward-dynamic model with a prosthesis foot [56].

Figure 2.19: Lower-limb amputee musculoskeletal model with a prostehsis [12].

elled using Hill-type actuators, which consisted of a contractile element representing the active muscle fibers, series elastic element representing the tendon, and parallel elastic element representing the passive fiber stiffness [57]–[59].

A typical muscle metabolic cost is given in Equation 2.1:

$$\dot{E} = \dot{h_A} + \dot{h_M} + \dot{h_{SL}} + \dot{W_{CE}} \tag{2.1}$$

$\dot{E}$ is energy liberation rate for each muscle, which is the sum of activation ($\dot{h_A}$), maintenance ($\dot{h_M}$), and shortening/lengthening ($\dot{h_{SL}}$) heat rates, as well as the mechanical work rate (W_{CE}) of the contractile element. This metabolic cost was usually used to run optimisation.

There are some different type of testing/design methods used. **Optimal Control** can predict muscle excitation independent from experimental data. It is achieved with minimising metabolic energy expenditure [57], [59]–[61]. **Optimal Tracking** determines muscle excitation to match model output to experimental kinematics and ground reaction force data [62]–[64]. **Reflex-Based Control** models human muscle spinal reflexes through a feedback system. In [61], reflex-based control was used in an amputee musculoskeletal model to incorporate balance control and recovery into a prosthesis controller.

2.2.2 Human-based testing

Human-based testing are the most common testing approaches nowadays. The design process of prosthetic devices has traditionally entailed intuition-based experimentation using limited subject data[12]. There are two types of human involved testing: amputee test and able-body test with modified devices.

Amputee test

Amputee test is able to get direct feedback from the users. During a development of a product, an intuitive test is to compare the kinematics between amputee and able-body. In [13], a lightweight hybrid robotic knee prosthesis was developed. In the amputee test, the knee kinematics was compared and proven to be closer to able-body. In [9], Tian et al. developed an intergrated electrohydrostatic powered ankle prosthesis. In the test, the control strategy was verified and ankle motion was compared to able-body data.

To further consider the dynamic performance of a product, moment-torque (force-position) are usually used [6], [20], [44], [65]. For active prosthesis, mechanical energy level of an active prosthesis is often examined as well [44], [66].

Another common approach to evaluate the performance of a leg prosthesis is to measure the amputees rate of oxygen consumption and carbon dioxide production in walking, as these measures correlate with metabolic rate[65]. Active prosthesis were proven to reduce human walking metabolic rate [44], [65].

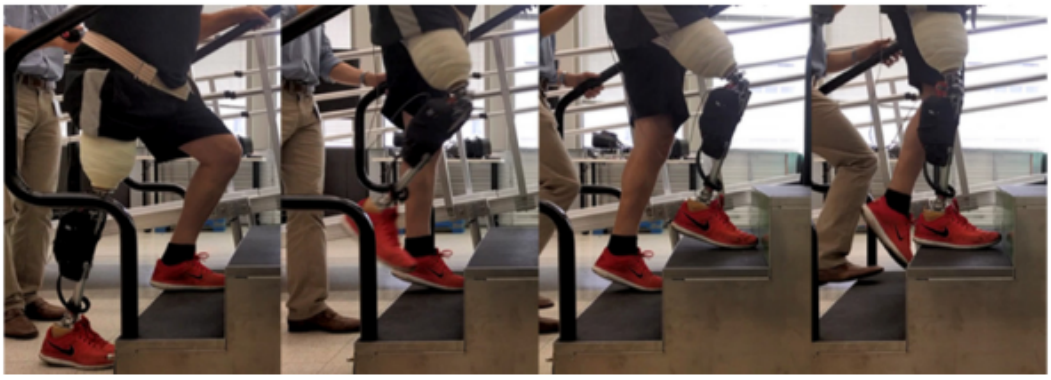

Figure 2.20: An example of amputee testing transfemoral prosthesis [13]

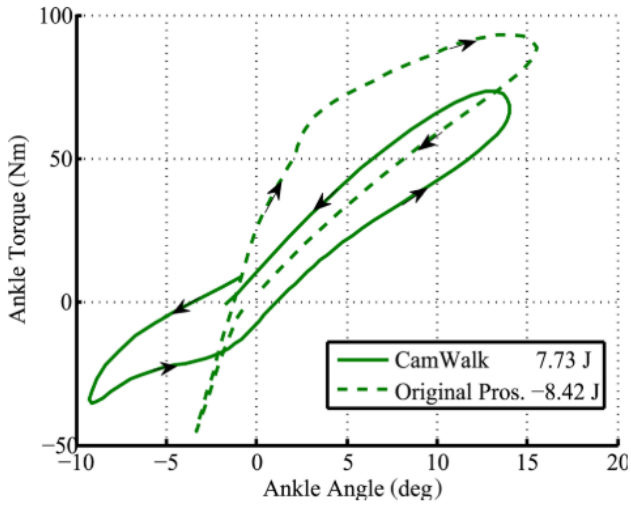

Figure 2.21: Ankle torque-angle curve of foot prostheses in walking [20]. CamWalk is an active prosthesis, Original Pros is a passive prosthesis. Anti-clockwise is positive energy output and clockwise is negative energy output.

Modified device testing

To overcome the lack of amputees test objectives, some gait emulators were developed to be used with able-body human [67], [68]. The robotic anklefoot prosthesis system that enables rapid exploration of a wide range of dynamical behaviours in experiments with human subjects. The push-off timing was studied in [14], it came out the push-off time has a strong effect on metabolic cost of the push-off power.

Asymmetric unilateral transfemoral prosthetic simulators were developed and tested with able-body [7], [69].

Figure 2.22: An example of testing with modified prosthetic knee simulator [69]

2.2.3 Testing Robots

Current lower-limb and ankle prosthesis testing standards mainly examine material fatigue, strength and joint reliability [10], [11]. Tests are limited to focus only on mechanical properties of a prosthesis. There were not many robots which tests lower limb prosthesis developed. Three types of lower limb related testing machines are reviewed. They are cadaveric gait simulators, sorcket interface test simulator and lower limb prosthesis testing robots.

Cadaveric gait simulator

A big group of researchers developed cadaveric gait simulators, for example [70]–[75]. These simulators focus on generating same load for the tested cadaveric feet. Cadaver studies are important to understand normal and pathologic foot function during a stride. Guo et al. did a good summary of current state of these cadaver gait simulators in [75].

Most of them generate less than 100 % BW and longer than normal stance phase duration. And also only vertical direction of load or load along tibia is considered. However, the loading methods that applied in cadaveric gait simulators can be used in prosthesis test robots. A summary of these cadaveric gait simulator is shown in Table 2.3.

Socket Interface Test Simulator.

In [76], the motion of 10 amputees walking were recorded. The 3D movement of the shank was recalculated to Euler angles to be used as input for the robot. A

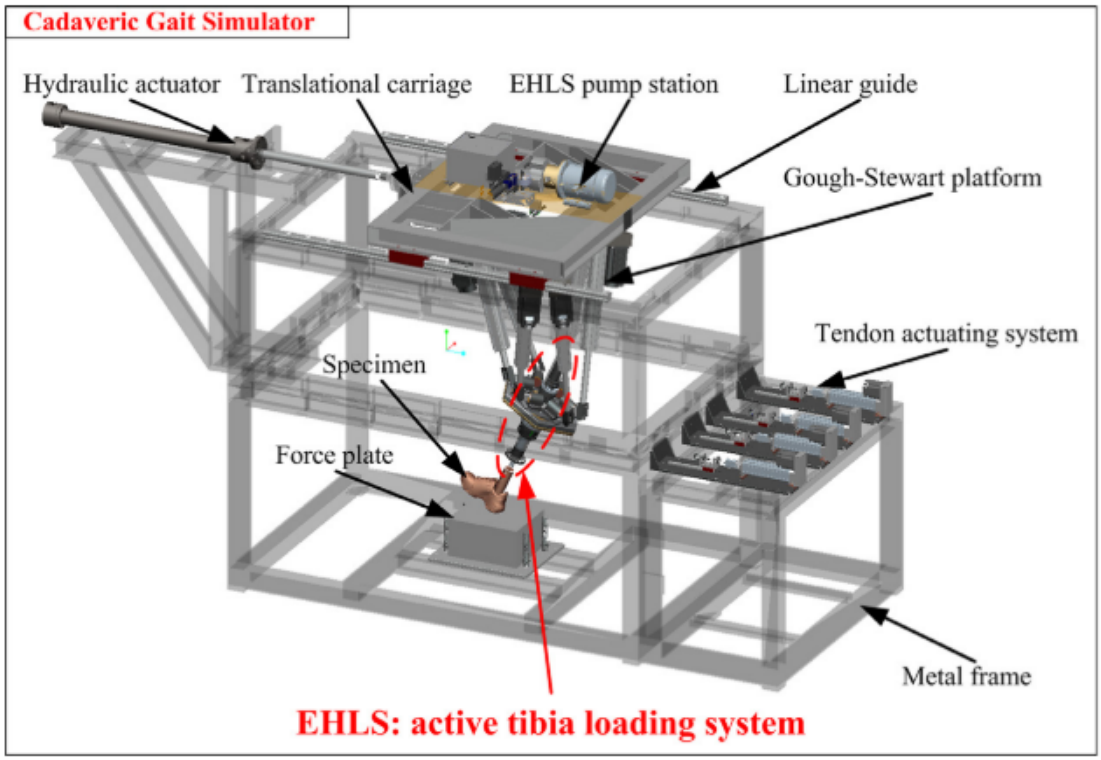

Figure 2.23: An example schematic of a cadaveric simulator [75].

Table 2.3: Review of cadeviric gait simulator.

Author	Tibia loading method and control mehold	Simulated BW	Stance phase duration
Sharkey [70]	Active tibia loading system, open loop control	1 BW	12 s
Aubin [71]	Active ground system, iterative learning control	0.75 BW	1.5s
Aubin [72]	Active ground system, fuzzy iterative learning control	1 BW	2.7s
Peeters [74]	Active ground system, inertial force feedback control	25kg	10s
Guo [75]	Active tibia loading system, iterative learning control	60 kg	5s

stump which includes 3D printed bones and soft tissue allows pressure measurement between stump and socket. The pressure can be used to represent patient comfort of different alignments. The detailed test results are not shown. McGrath developed a socket interface simulator which is compatible with uniaxial mechanical test machine [77]. The vertical load data from an amputee was applied and compression sagittal bending and anteriorposterior (AP) shear were collected and compared.

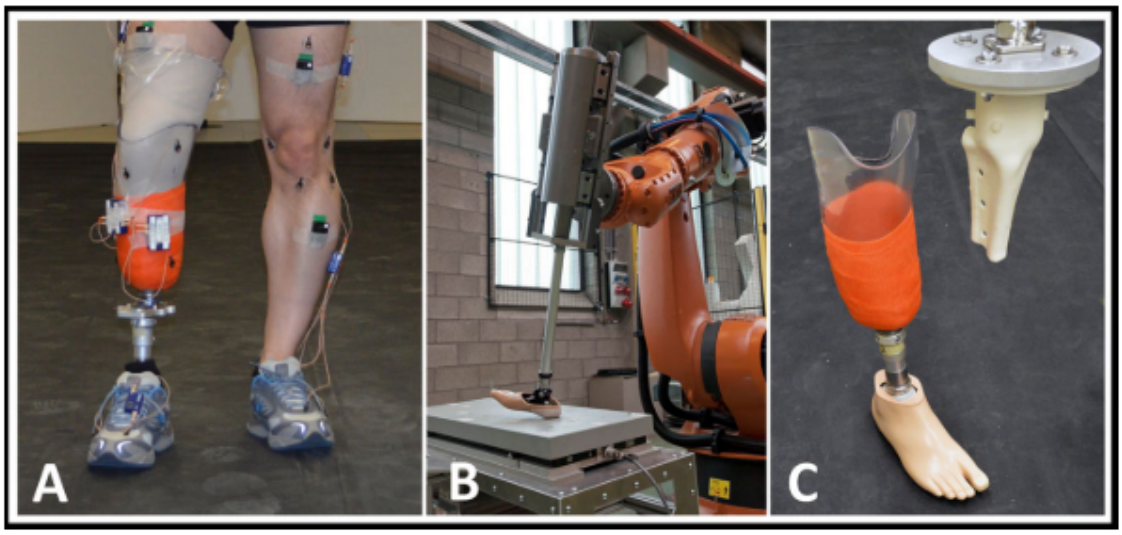

Figure 2.24: A. gait analyses of an amputee B. robotic gait simulator C. artificial stump[76]

Lower limb Prosthesis Test robot

There are not many research groups developed testing platform specialised for lower limb prostheses. Two relatively developed prosthesis test platforms are described.

The first example:

Cleveland State University developed a gait simulator leg prosthesis testing robot and published some related work since 2014 [78]–[82], as showed in Figure 2.25. The gait simulator has three degree of freedoms, which are hip vertical displacement, thigh angle and knee angle. The knee and ankle part are testing parts. The robot walks on a treadmill. If the knee joint is a passive prosthesis, then the test robot is underactuated.

In [78], a hybrid dynamic model was developed which employed a constraint lagrangian motion equation. The model has swing mode and stance mode. In the swing phase, the robot is modelled as a 3-link rigid robot with a prismatic-revolute-revolute (PRR) configuration. The Denavit-Hartenberg (DH) coordinate frame assignments is shown in Figure 2.26. In the stance mode, the ground contact model is a non-slip model. The foot horizontal velocity is constrained to match treadmill belt moving speed. The knee joint angle is derived from kinematics. The foot is allowed to deflect the treadmill belt in vertical direction with purely elastic effect.

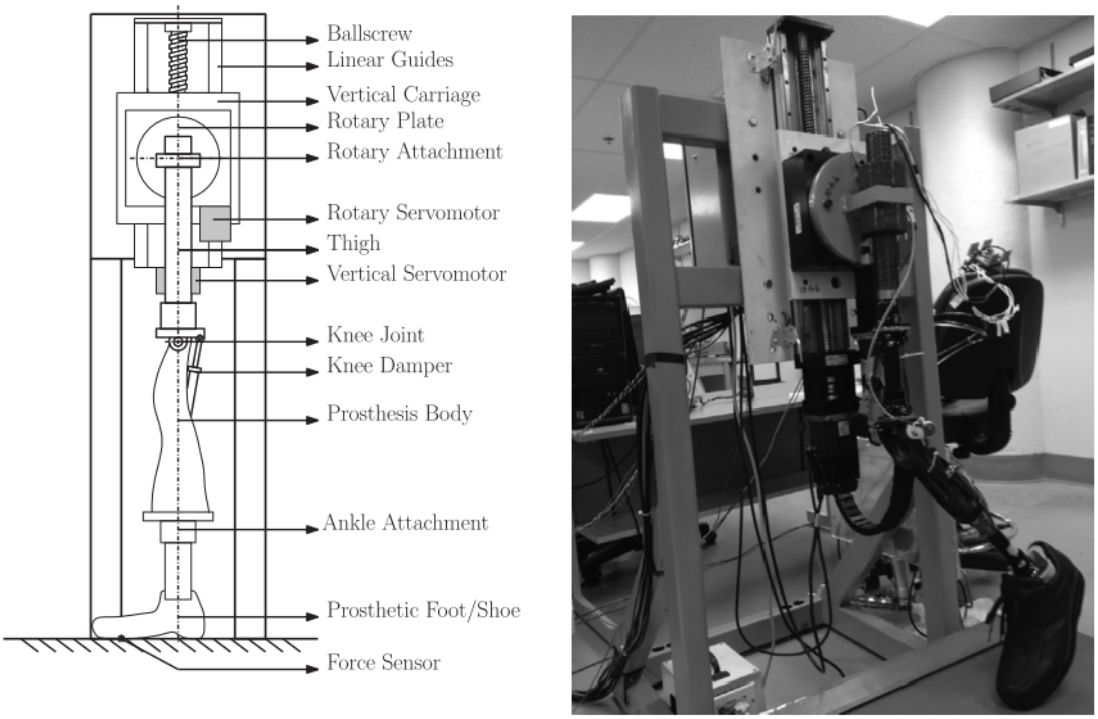

Figure 2.25: Left: Prosthesis testing robot schematic. Right: physical construction of a prosthesis testing robot [78].

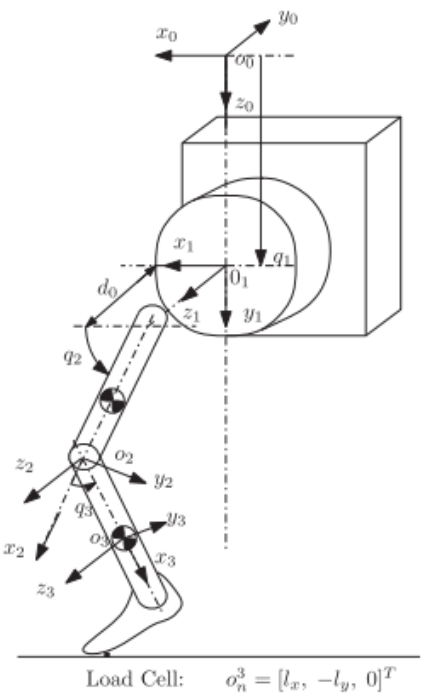

Figure 2.26: Denavit-Hartenberg (DH) coordinate frame assignments. [78]

In [81], a novel testing method was proposed with using biogeography-based optimisation (BBO). Biogeography is the study of the speciation, migration, mutation, and extinction of organisms. BBO simulates this process with the goal of optimisation [83]. It was applied to achieve GRF control. The robot starts with hip height and thigh angle motion of able-body data. The hip vertical displacement and thigh joint angle control singal are gradually adapted to improve the ground reaction force with BBO. 62 % lower GRF than the initial contact force was achieved. This process is seen as a compensation that a amputee would do when using the same prosthesis product.

Some research on control system has also been carried out on the platform. In [80], a passivity-based controller was proposed to reduce tracking error in the presence of parametric uncertainties and disturbance forces from ground contact during the stance phase. In [82], a robust adaptive impedance control was developed for the test rig, a trade-off between tracking performance and GRF was achieved.

Second example: Berlin Institute of Technology deleloped a gait simulator for lower limb exoprostheses [79]. The test rig employs five hydraulic actuators in the rig. Three actuators are used to achieve hip flexion/extension (A1), of adduction/abduction (A2) and of inversion/ eversion (A3). Two actuators are used for vertical (B1) and horizontal movement (B2) of the instrumented foot plate which records ground reaction forces. The test rig has position control in the swing phase and force control in stance phase. State machine for the gait simulator is shown in Figure 2.27b. The force controller in the state machine and its performance were

not explained in detail.

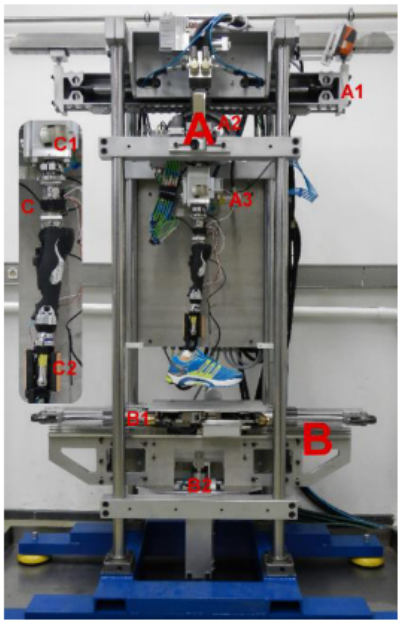

(a) Gait simulator rig setup.

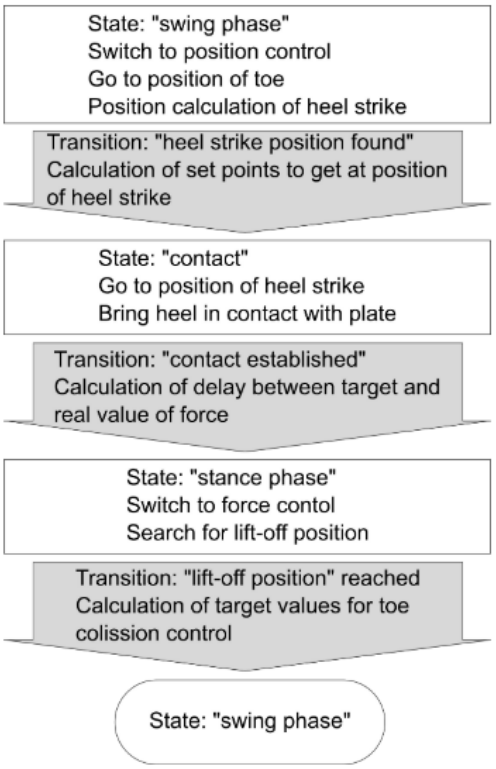

(b) State machine of test rig.

Figure 2.27: Gait simulator developed by Berlin Institute of Technology A: hip module, B: foot module, C: Oktapod force measuring system [79]

An example of testing two microprocessor controlled knee (MPK) joints are carried out in [79]. The testing method is that the test rig is controlled to replicate kinematic and kinetics reference data from an able-body walking. Maximum position of knee joint during the gait was recorded with different walking speeds. The rig has successfully identify the difference of two microprocessor controlled knee (MPK) joints, which agrees with their previous lab testing result with small difference [84].

Other primary studies of test platform: An conceptional design is shown in [85], the robot has three degrees of freedoms. It was designed to have two control loops which are position tracking in swing phase and force control stance phase. Only simulation result were shown. The detailed controller design and testing methods were not described.

In [86], a primary conceptional design of a gait simulator for testing lower-limb active prostheses was presented. It uses commercial 6 axis robot to replicate hip motion, the test prosthesis is attached on the end-effector. The control has two control loop which has position control during a gait swing phase and force control during a gait stance phase. In order to address the large disturbance forces arises at the initial contact, a moving force platform is introduced into the system, see Figure 2.28. The detailed controller design and testing methods are not clear.

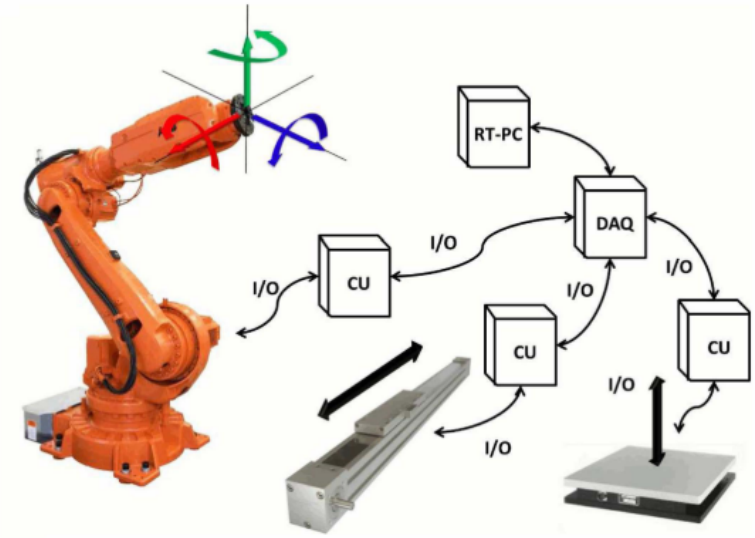

Figure 2.28: Concept design from Marinelli et al.[86].

Other contributions

There are some other work done related to prosthesis test gait simulator. A prosthetic knee angle measurement was validated in a robotic simulator [87]. Zhang et al.developed a lower leg robot to simulate normal human gait [88], this work was an primary research on developing lower limb prosthesis. The gait simulator successfully imitate human walking gait in terms of kinematics and kinetics. Some potential balancing control can be investigated with the platform.

Figure 2.29: Two leg lower prostheses walker and its force test table [88]

2.3 Concluding Remarks

Human walking/running biomechanics are well understood in terms of kinematic and dynamics data analysis. Amputee's walking gait is different from able-body's gait. With a passive prosthesis, amputees tend to weight more and prolong the period of stance in the non-affected limb. More moment are experienced at hip and knee joints of the non-affected limb and less moment are measured on the prosthesis side. This unbalance usage of both legs is believed to cause osteoarthritis, osteoporosis and joint pain. Active prostheses are found to reduce the unbalance.

Prostheses play an important role of improving an amputee's life quality. Many lower limb prostheses were developed. There are three main testing classifications to test lower limb prosthesis, which are model-based testing, human-based testing and robot-based testing.

Model-based testing mainly focused on musculoskeletal models which use forward dynamic model to run gait optimisation subject to minimising difference of kinematics compared to able-body, muscle metabolic energy expenditure. The effects of using prosthesis in a musculoskeletal system were investigated. However, current musculoskeletal models are computationally expensive, lack model validation and prosthesis device validation, collectively limiting the integrity of device designs optimisation through musculoskeletal modelling.

Human-based testing provides the most direct feedback of the test prosthesis. It is commonly used during a prosthesis development.

There were many cadaveric gait simulators developed, their goal are applying the load of a able-body human and investigate normal and pathologic foot function during a stride. Load control techniques were developed such as ILC on tibia load and fuzzy logic control. There wasn't much work carried out for gait simulator designed for testing prostheses. Two groups of researchers have developed relatively complete gait simulators. The others' studies were in primary stage. Most testing approaches of these benches focused on input motion/force on test prostheses, they haven't described how to evaluate the test prostheses.

In summary, both Model-based testing and Human-based testing have their limitations. Robot-based testing is a developing area which doesn't have much work done. In Table 2.4, the current testing state of art is presented:

Table 2.4: Summary of literature.

Test Method Classification	Model-based Testing	Human-based Testing	Robot-based Testing
Existing Literature	Simplified mechanical model [46]–[54] ; Mechanical models with net moment [55], [56]; Musculoskeletal model [57]–[59], [61]–[64]	Amputee test [6], [9], [13], [20], [44], [65], [66]; Modified device test [14], [67], [68]	Replicated motion/vertical force [78]–[82]; Product fatigue test [10], [11]; **Robot with a systematic approach to evaluating the performance of a test lower limb prosthesis** ;
Advantage	Fast test; Consistent results	Direct feedback; Reliable results	Fast test; Consistent results; Reliable results; Various test environments
Disadvantage/ Not achieved	Lack of fidelity	Low objectivity, Limited test environments, Hard to recruit volunteers, Safety concern	**No existing systematic test approach; No test result analysis apart from [79]; No existing approach to achieve not only vertical GRF but also horizontal GRF**

In this P.hD, emphasis has been put on developing a robot with a systematic approach to evaluating the performance of a test lower limb prosthesis. The work will explore the subclassfication which is in bold text in Table 2.4 and fill the gap in the literature.

Chapter 3

Preliminary Hardware-in-the-Loop testing Investigation

Hardware-in-the-Loop (HIL) testing has been used successfully for a number of years on a wide range of applications. Any delay in actuation systems will increase the system energy if it is not properly compensated for due to the negative damping effect. A HIL walking/running testing system has advantages for testing lower-limb prosthetics over traditional human-based testing, i.e. safer, more objective. However, the stiff ground contact discontinuity is hard to compensate. This chapter investigates the effect of introducing nonlinearity and discontinuity into a HIL system by comparing three types of Spring Mass System (SMS). A dimensionless variable R_f was introduced to describe a HIL system, referred as the delay frequency. It is the ratio of the actuation delay and system natural frequency. It will be shown that R_f is larger than 20. This informs the requirements of actuation response time in future experiment setup. The HIL testing was abandoned due to the extremely fast speed response actuation requirement.

This chapter is organised as following: the first section reviews the background knowledge of HIL. The second section describes three spring mass systems and models delay compensation process. In the third section, delay frequency and system natural frequency ratio R_f are investigated. In the end, a conclusion is drawn.

3.1 Introduction

Hardware-in-the-Loop (HIL) technology is known as Hybrid testing or Model-in-the-Loop Simulation (MIL). There are various definitions of HIL simulations [89], [90]. Here, HIL testing is defined as a test system which is implemented with both a numerical model and a physical system. Hybrid testing technology has a wide range of applications in the aircraft, automotive, seismic and defence industries [91]–[93]. These applications benefit from the advantages of HIL testing: (1) High fidelity (2)Low cost (3) Flexibility (4)Concurrent systems engineering.

To authors' best knowledge, no one has implemented walking simulation with HIL. A HIL walking simulation could be used to develop walking robot parts and testing lower limb prosthetics.

An example HIL testing with an industrial robot on a lower leg prosthesis is shown in Figure 3.1. The testing system consists of a virtual system, a transfer system and a physical system. In the virtual system, a human walking model is simulated. Different from a normal walking simulation, an interface point is created and located at one of the lower legs just like an amputee. The simulation is outputting the interface point position to a robot controller. In the transfer system, an industrial robot is position controlled to move the prosthetic foot to the position demand from the simulation. In the physical system, a real prosthetic foot makes contact with ground. A force sensor is used to connect the end-effector of the robot and the top of the prosthetic foot. It measures torques and forces at the physical interface and feeds them back to the walking simulation.

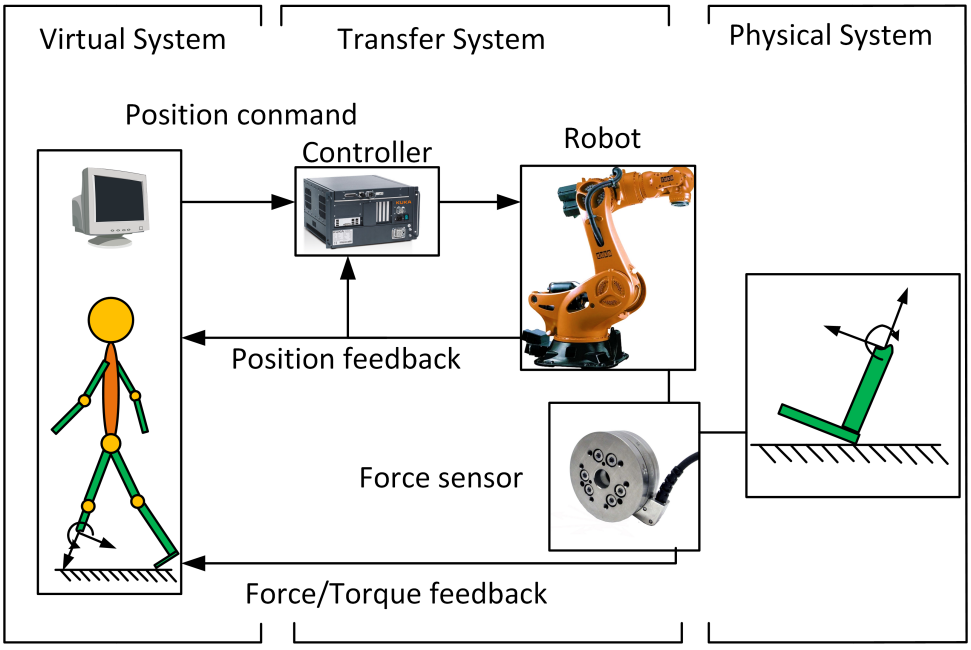

Figure 3.1: An example of HIL walking simulation architecture for testing a foot prothesis.

For HIL testing, a delay in the actuation system is inevitable. Such a feature will lead to an effect equivalent to negative damping[93]. If the negative damping is larger than system damping, a system will be unstable. To solve this problem,

compensation of delay is necessary. Walking is a dynamic process with nonlinearity and discontinuity. Ground contact can be regarded as a high natural frequency system due to very large stiffness of the ground. Therefore, HIL testing for such a system is challenging. This might be one of the reasons why no one has developed a HIL in walking or running test system before. In this chapter, a Spring Mass System (SMS) is used as a simple example to study a HIL hopping or running system.

In the remainder of this chapter, a Lead Compensation (LC) and Horiuchi Compensation (HC) [93] are implemented on a HIL SMS with different properties to investigate system stability.

3.2 Preliminary Analysis with Spring Mass System

3.2.1 Three types of Spring Mass System

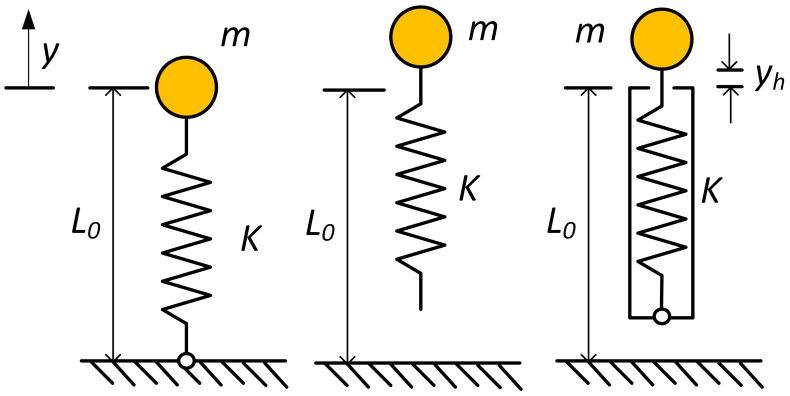

Figure 3.2: Left: SMS with fixed foot. Middle: SMS hopper Right: SMS hopper with a hard stop.

Figure 3.2 shows three simple SMS. The SMS consists of a mass and a spring under the mass. The mass is able to move vertically. y is the displacement of the point mass starting from the spring in equilibrium.

The initial parameters of these SMS are shown in Table 3.1. This gives the system normalised system energy E_n and normalised stiffness K_n :

$$\begin{cases} E_n = \frac{E}{L_0 mg} = 1.05 \\ K_n = \frac{KL_0}{mg} = 20 \end{cases} \tag{3.1}$$

This set of parameters gives a human-like characteristic in the Spring Loaded Inverted Pendulum (SLIP) walker [47]. The natural frequency of the system is similar to human walking body frequency so that I consider it as a starting point for the investigation of HIL walking testing.

Linear, Continuous Spring Mass System (LCSMS): In the left of Figure 3.2, the SMS has a fixed foot on the ground. The force applied on the system is

Table 3.1: SMS simulation parameters

m(Mass)	L_0 (Length of Spring)	K(Stiffness)	f_n(Natural frequency)	E(Total Energy)
70 kg	1 m	13 734 N m^{-1}	2.23 Hz	721.03 J

linear and continuous. The dynamic equation of the SMS is:

$$(\ddot{y} + g)m = F_s = -yK \tag{3.2}$$

Nonlinear, Continuous Spring Mass System (NCSMS): Unlike the left SMS, the middle SMS is free to hop. Thus, it will have two phases i.e. air phase and stance phase. In the air phase, the mass takes zero spring force. In the stance phase, the mass takes spring force proportionally to the compression of spring. The combined force of both phases that is nonlinear and continuous. The dynamic equation of the SMS is:

$$(\ddot{y} + g)m = \begin{cases} 0 & \text{for } \ y \geq 0 \\ -yK & \text{for } \ y < 0 \end{cases} \tag{3.3}$$

Nonlinear, Stiff Spring Mass System (NSSMS): The last one in the right has a "hard stop" on the spring when the spring is compressed over y_h, $i.e. y < -y_h$. The "hard stop" is simulated as another very stiff spring. This "hard stop" is considered to be close to a sudden hard contact with ground. The dynamic equation of the SMS system is:

$$(\ddot{y} + g)m = \begin{cases} 0 & \text{for } \ y \geq 0 \\ -yK & \text{for } \ -y_h \leq y < 0 \\ -y_h K + (y - y_h)K_h & \text{for } \ y < -y_h \end{cases} \tag{3.4}$$

y_h is assumed to be 0.05 m. K_h is set to $20K$ to create the discontinuous force. I consider it is good enough to represent a "hard stop" from the ground.

3.2.2 HIL Testing of SMS and Compensation Method

In Figure 3.3, HIL testing of SMS configuration is shown. It has a similar configuration with the HIL prosthetic foot testing in Figure 3.1. All parts of this system are simulated in a computer to do preliminary analysis. In this initial investigation, the actuation system is defined as a pure time delay:

$$A(s) = e^{-s\delta t} \tag{3.5}$$

A dimensionless variable R_f is introduced to describe the simulated system, see Equation 3.6. f_n is the system natural frequency. This variable relates the actuation delay and the system natural frequency. The higher R_f is, the faster response the actuator has compared to the system.

$$R_f = \frac{1}{\delta t \cdot f_n} \tag{3.6}$$

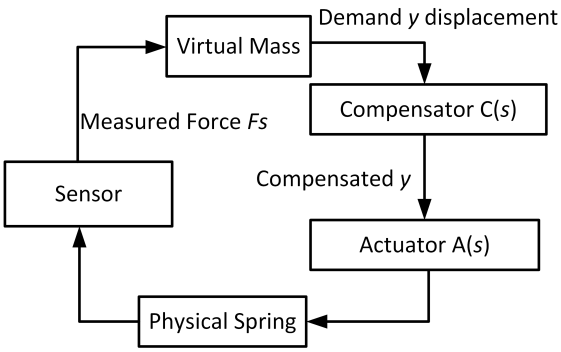

Figure 3.3: HIL testing of SMS configuration. Note: all parts are simulated in this investigation.

Without compensation, due to the lack of damping in this system, SMS will often be unstable. In Figure 3.4, an example of LCSMS is shown. With $R_f = 45$, roughly 0.01 s delay, the system is unstable. One way to solve the problem is introducing a compensator to the input signal.

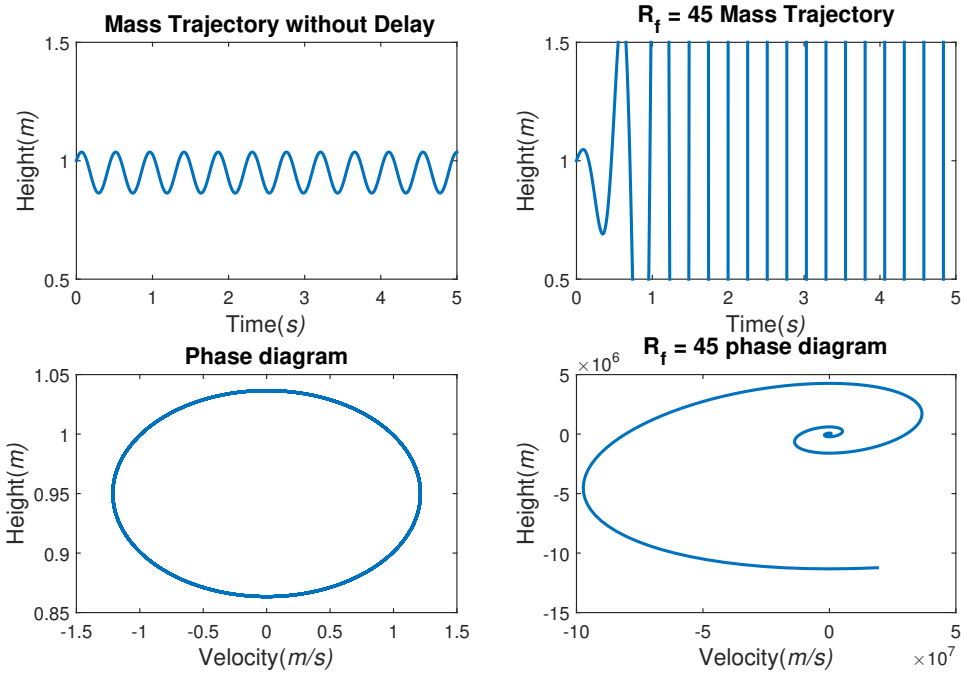

Figure 3.4: An example of delay effect in HIL testing of the linear continuous SMS.

A time domain schematic of a compensation process is shown in Figure 3.5. Due to the actuation delay, the resulting signal has a delay of δt relative to the input signal. With predicted input signal (or compensated), the target signal becomes almost identical to the resulting signal.

Two types of compensation are tested in this paper:

(1).Lead Compensation (LC): The constant delay actuation in the simulation is estimated as a first order lag in Equation 3.7:

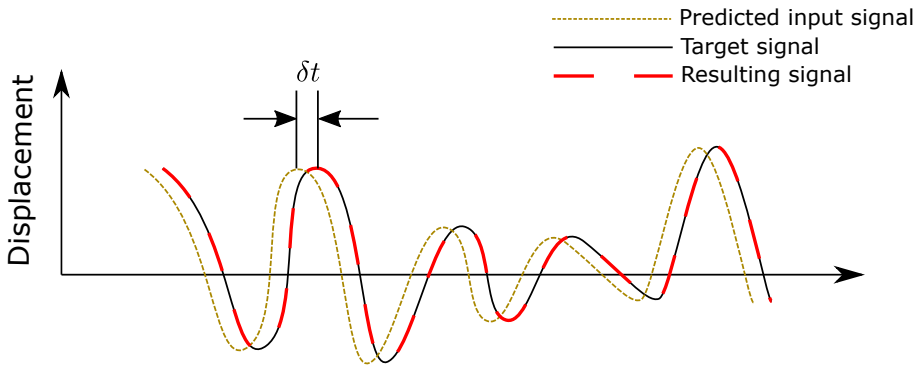

Figure 3.5: Schematic of a compensation process.

$$A(s) = \frac{1}{\tau s + 1} = \frac{1}{\delta t s + 1} \tag{3.7}$$

In Figure 3.6, a comparison of bode diagram of first order lag system and constant delay is shown, in which, the constant delay and the time constant τ of the first order lag system are both $0.1s$. One can see, the estimation is rather good when the frequency is lower than the cut-off frequency, which is $10Hz$. It also shows that if the simulated system frequency is close or higher than the cut-off frequency of the first order lag, the compensation will lose accuracy.

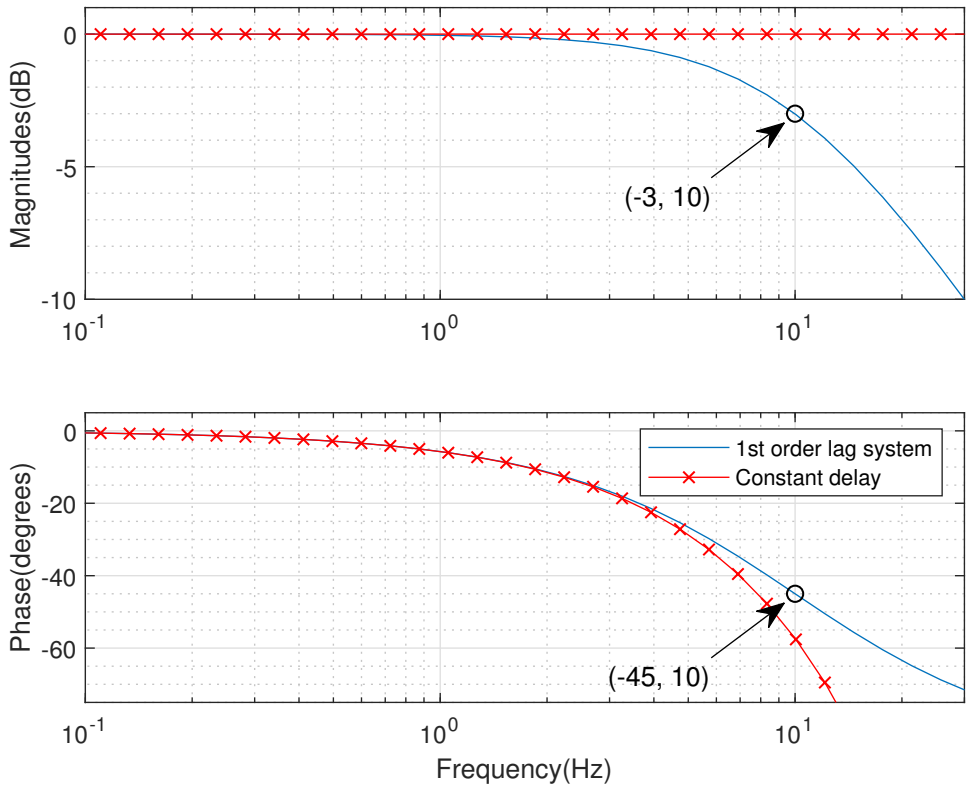

Figure 3.6: Bode diagram of a first order system and constant delay.

The first order lead compensation uses the inverse model of the estimated first order lag. It is presented in Equation 3.8:

$$C_0(s) = \frac{1}{A(s)} = \tau s + 1 \tag{3.8}$$

where τ is the simulated actuator delay. A large pole, $s = -1/D = -10^4$ is added to make the lead compensation implementable, which has little effect of the system:

$$C(s) = \frac{\tau s + 1}{Ds + 1} \tag{3.9}$$

(2).Horiuchi Compensation (HC): Horiuchi proposed a delay compensation using a polynomial function [93]:

$$x_{new} = \sum_{i=0}^{n} a_i x_i \tag{3.10}$$

where a_i are coefficient constants. x_i is the measured position i samples previously. n is the order of the equation. x_{new} is compensated position signal that feeds into the actuation system. The predicted value x_{new} was obtained by extrapolating a *nth*-order polynomial function based on present and n previous calculated values, see Figure 3.7.

$n = 1$ will be explained here. The extrapolation function $P(x)$ can be presented as Equation 3.11:

$$P(t) = (x_0 \cdot (t - t_0 - \delta t) - x_1 \cdot (t - t_0))/\delta t \tag{3.11}$$

$P(x)$ equals to x_0 when $t = t_0$ and it equals to x_1 when $t = t_0 - \delta t$. Letting $t = t_0 + \delta t$, the coefficients of the polynomial can then be determined. Equation 3.11 is simplified as Equation 3.12:

$$P(t) = a_0 x_0 + a_1 x_1 = 2x_0 - x_1 \tag{3.12}$$

Similar higher-order extrapolation functions can be constructed in this way. The coefficients a_n are listed in Table 3.2:

Table 3.2: Coefficients of Horiuchi Compensation.

Order	a_0	a_1	a_2	a_3
n = 0	1			
n = 1	2	-1		
n = 2	3	-3	1	
n = 3	4	-6	4	-1

The higher the order is, the higher damping effect can be introduced into the simulated system, the more stable system is, however the accuracy goes down [94]. The order of the Horiuchi compensation is selected to be $n = 3$. It gives the relatively high positive damping region and accuracy.

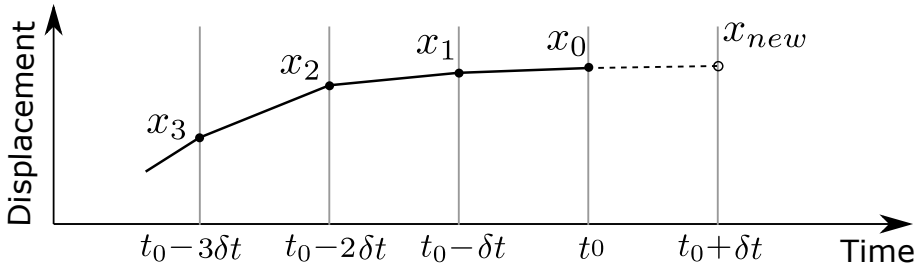

Figure 3.7: Horiuchi compensation schematic.

3.2.3 Results

The simulation is implemented in the MATLAB/Simulink environment. The solver is *ode*8. The time step is 10^{-4} s. R_f is selected to be 40, which means 0.011 s delay in actuation system. The *ode* solver is accurate because the time step is much smaller than the simulated actuation delay. The model is executed for 15 cycles. The phase diagrams of the simulations are shown in Figure 3.8.

Without compensation, the three systems all lose accuracy very quickly. The LC and the HC work fine for LCSMS and NCSMS despite the lead compensation causing a slight energy increase. However, both compensations fail in NSSMS due to the "hard stop" from the very stiff ground spring. The ground stiffness, K_h, leads to a high natural frequency system. The delay frequency and natural frequency ratio R_f for the ground in this case is calculated to be 8.95, which seems too small. It is necessary to determine the accepted range for R_f.

3.3 R_f Limit Test on the LCSMS

The "hard stop" from the ground in the NSSMS is equivalent to a high stiffness LCSMS. An investigation on LCSMS can be useful to tell the reason why the compensations fail in NSSMS. SMS is expected to be energy conservative. It is possible to evaluate the simulated system accuracy by examining system energy. In this section, a range of R_f values are tested on LCSMS. After the simulation being executed for 15 cycles, system energy is recorded. In Figure 3.9, the simulated results are shown.

From the bar graph, one can notice system energy change increases as R_f decreases. This means HIL emulation of HIL is less accurate when the actuation delay is longer, which meets our expectation. Also, Lead Compensation increases energy while Horiuchi Compensation decreases energy.

Assume that about 1% of energy change for every cycle is acceptable. After 15 cycles, energy change is required to be roughly smaller than 100 J. Up to now, I can say that $R_f = 20$ is currently the lowest value to meet our requirement. For the "hard stop" from Section 3.2, $R_f = 8.95$ is much smaller than the requirement, that is why the phase diagram was not close to the expectation. A further analysis is needed to give a clearer idea of the accepted range.

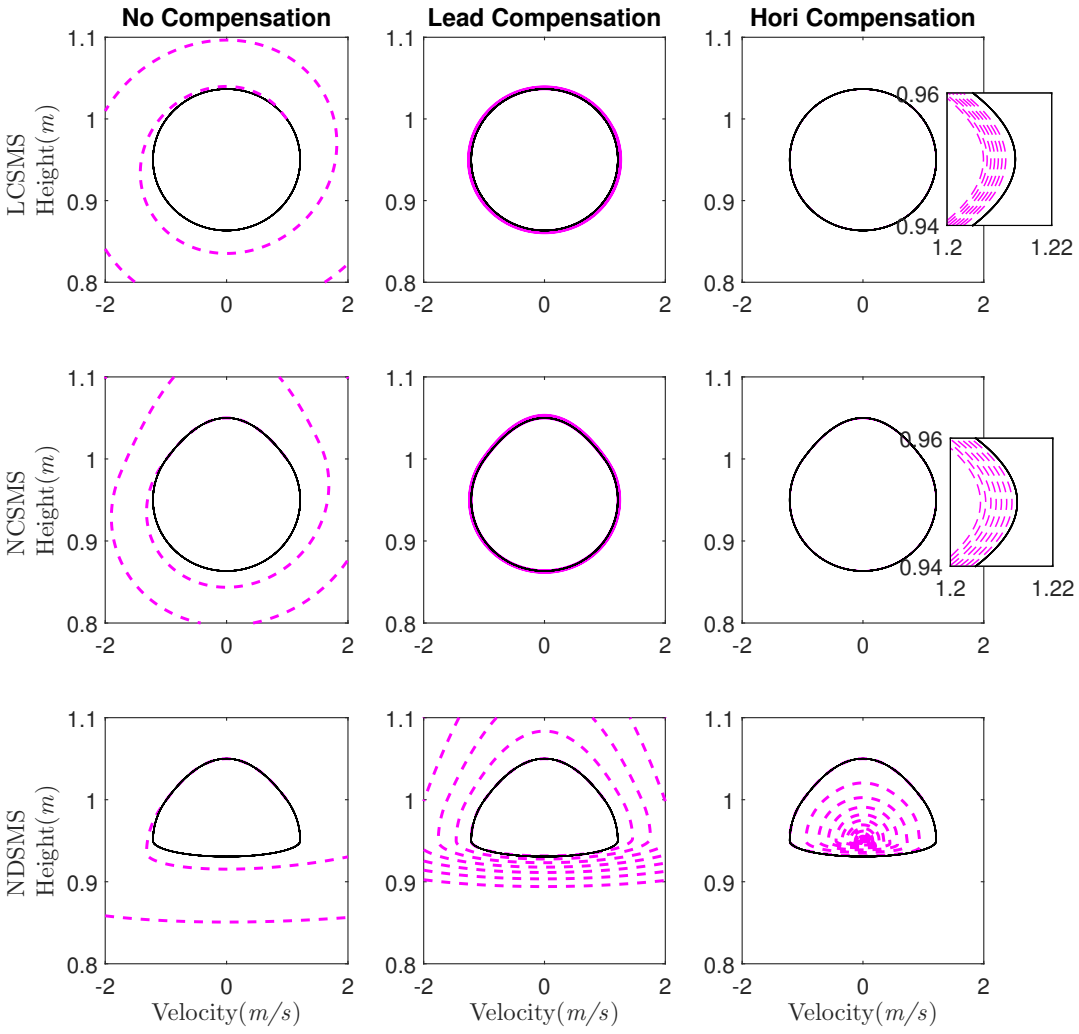

Figure 3.8: Comparison of three types of SMS with LC and HC Phase Diagram. Black solid curves represent expected original phase curve. Magenta dashed curves represent actual simulated phase curve. Two partial enlarged diagrams are displayed in the boxes on the right side.

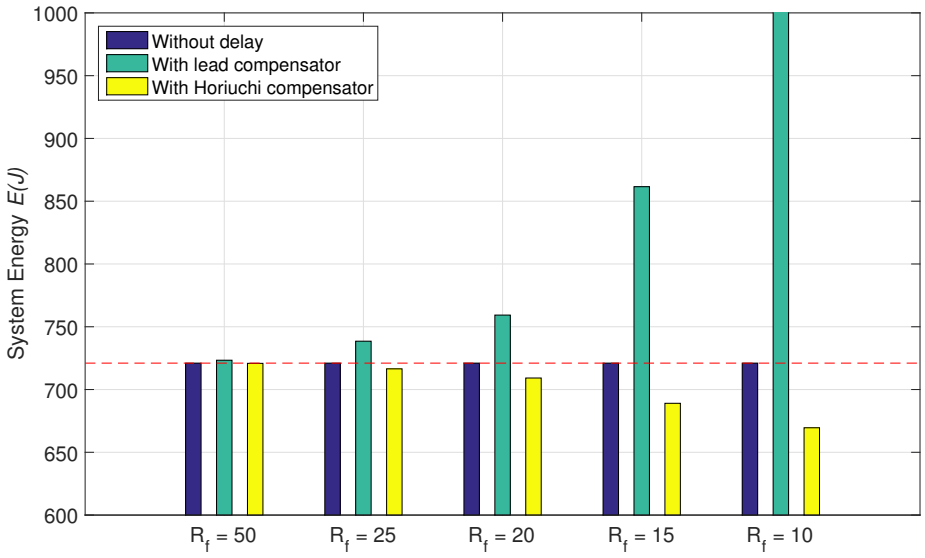

Figure 3.9: LCSMS System Energy with different R_f values and different compensations. The original system energy is shown with red dashed line. The left dark blue bars also represent original energy of the systems.

3.4 Conclusion

This chapter proposed a new potential HIL application for prosthetic testing. Three types of Spring Mass System (SMS) were tested in simulation to investigate the main obstacle of such an application. It was found that the very large stiffness from the ground caused a loss of fidelity in the Nonlinear, Stiff Spring Mass System (NSSMS). A dimensionless variable R_f was introduced to describe a HIL system with the actuation delay and system natural frequency, reffered to as the delay frequency. It will be shown that the required value of R_f is analysed and determined to be larger than 20. This informs the actuation system requirement of performing a real time HIL testing for walking.

For a Spring Loaded Inverted Pendulum (SLIP) walker model, there is no real "hard stop" from the ground, so it is similar to NCSMS. In this case, the dominant factor is the body or leg swing frequency (about 2 Hz). HIL testing should be easy to implement. However, in experimental testing, walking system with HIL may also exhibit a high frequency mode from the ground contact, which will lead to a loss of fidelity in testing. The typical stiffness of an ankle prosthesis for walking ranges from $20\,kN/m$ to $50\,kN/m$. With the current conclusion, $R_f > 20$, it requires the position controlled actuation delay be less than $3\,ms$. Building a HIL test rig usually uses hydraulic actuation because of its load ability and power rating. However the required response of this actuation system is challenging. The lack of a numerical human walking model control and a standard to evaluate prosthesis also limits the HIL prosthesis testing. The HIL testing solution is abandoned.

There are some potential solutions that could be explored in the future: force controlled HIL testing, improve actuator control to reduce actuation delay and pseudo

dynamics HIL testing. In the pseudo dynamics HIL testing, the applied time scaling have the advantage that actuators with inadequate response speed and power rating could be used. However, active prosthesis devices cannot be tested in pseudo dynamic HIL testing.

Chapter 4

Testing method on lower limb prosthesis

This chapter will illustrate a new method on lower limb prosthesis testing. With a general robot leg, Three possible testing approaches were proposed: Forward Dynamic Approach (FDA), Inverse Dynamic Approach (IDA), Hybrid Approach (HA). The first section is a general introduction of the new testing approach. The second section presents a novel Iterative Learning Control (ILC) on ground reaction force control. It includes the derivation of the Extended Iterative Learning Control (EILC) of force algorithm, an analyse of the converge criterion of the EILC and delay compensation of the EILC.

4.1 Testing approach

To better describe the testing methods, a simple robot testing robot is presented in Figure 4.1. It has hip and knee joints just like a human leg. The test prosthesis is connected to the lower leg of the robot. To test prosthesis, a gait needs to be generated for the robot. Inspired from techniques in skeletal modellings, prosthesis testing methods are categorised into three groups based on gait generations :

- Forward Dynamic Approach (FDA): Use a test rig to replicate leg motion of a human gait. Then prosthesis performance and gait analysis can be conducted.
- Inverse Dynamic Approach (IDA): Replicate the required GRF from a human gait. Then prosthesis performance and gait analysis can be conducted.
- Hybrid Approach (HA): Both GRF and motion of human natural gait are considered. The test prosthesis are tuned that GRF and motion are compromised to achieve the best performance overall.

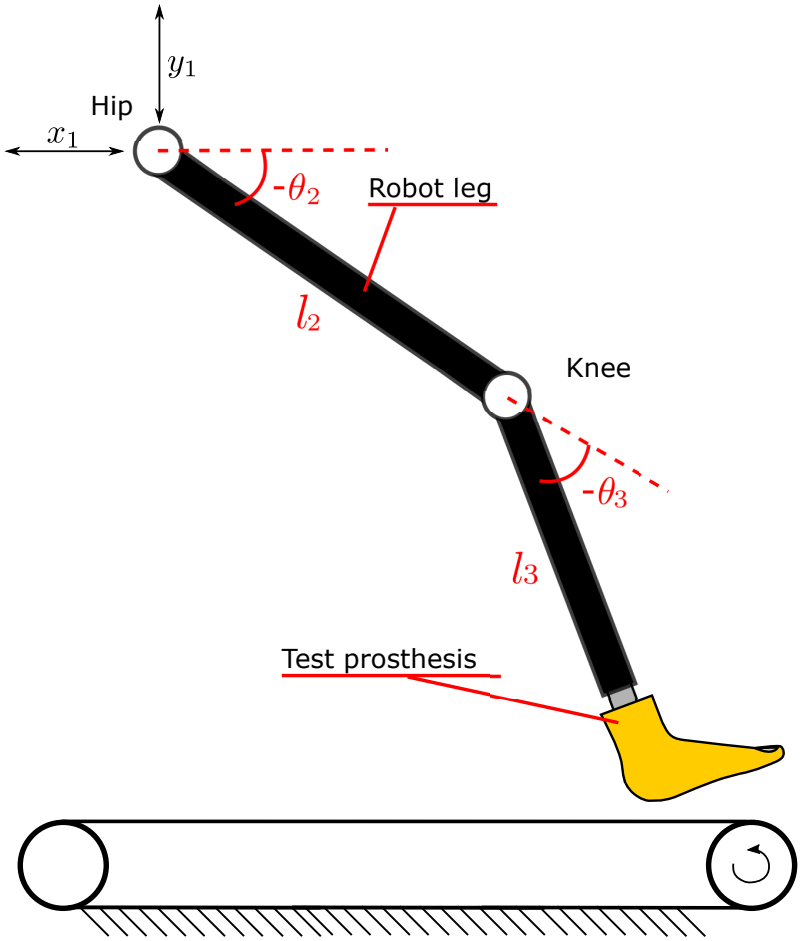

Figure 4.1: A simple lower limb prosthesis testing robot schematic.

For the FDA, the core challenge is to have an accurate motion control of the robot leg. Also, it requires well-calibrated relative position between the robot leg

and the treadmill to make sure the ankle contact the ground in correct time. The drawback is that the testing process may not be able to provide the same human load to the tested prosthesis in the beginning, which some active prostheses control system relies on. For the HA, similar idea is used often in skeletal models [59], [62]. In those simulations, muscles activities are optimised to achieve both motion and ground reaction forces. However, in the test rig, there isn't enough degree of freedoms and actuation to achieve them at the same time. Also, the criterion to evaluate a prosthesis needs to be further investigated.

The IDA is selected. It mainly has two reasons. First, providing the correct GRF can avoid overloading the prosthesis. The second, it has a simple and clear control target compare to HA. How the robot leg alter its gait when prosthesis changes can be compared to human. In the IDA, the GRF of natural human gait is chosen for this research because the result is compared to able-body gait. The process is shown in Figure 4.2.

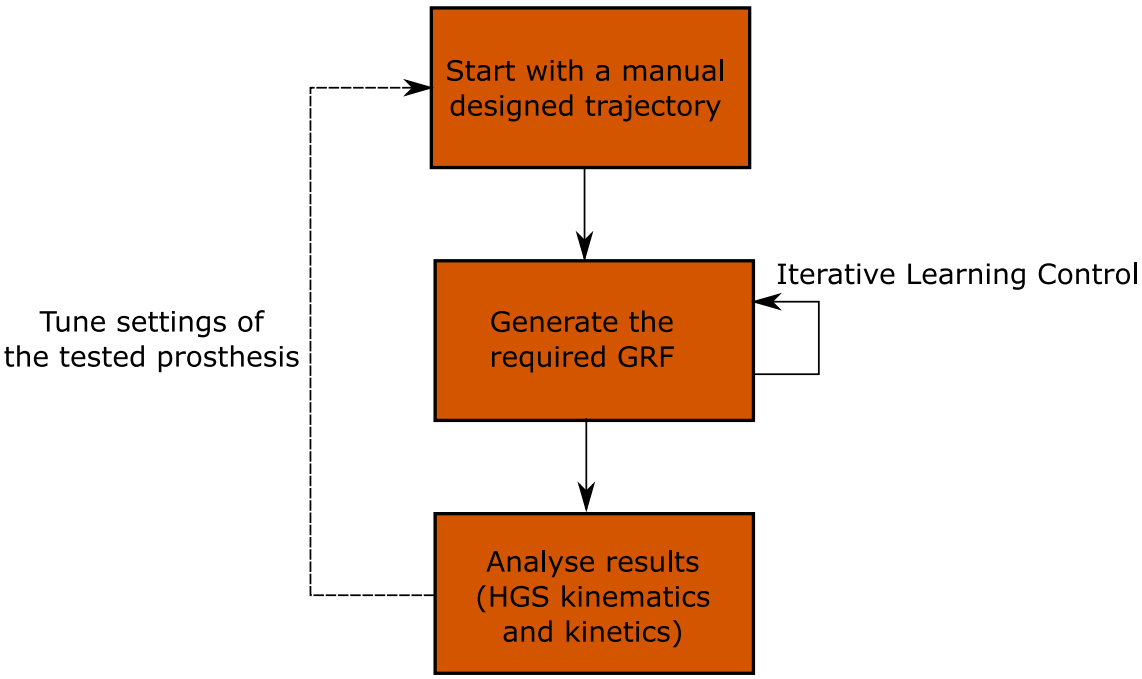

Figure 4.2: Prosthesis testing iterative chart.

A challenge is how to achieve the 2D GRF control with the HGS. Achieving the required GRF in vertical direction has been successfully applied in previous research [71]. However, it is very important to realise the horizontal force control since the horizontal force is vital to develop the correct ground reaction force (GRF) impulse. It means the generated gait could possibly help a human body centre of mass moves in a human-like trajectory. Also, the correct GRF will avoid overloaded friction or vertical force, which will protect the test prosthesis. Thus, I extended it into two dimensions to control horizontal and vertical contact forces. The proposed controller can be used with moving ground surface.

4.2 Proposed 2D Extended ILC controller

4.2.1 Introduction of iterative learning control

ILC is a technique to improve control precision for a system to operate in a repetitive and periodic manner in a fixed time interval. Each attempt is called a "trial", "cycle" or "iterative". ILC is widely applied in industry like stroke gait recovery, machine tool control, space engineering, military, robotics [95]–[97]. The idea behind the ILC is to use the information from previous trials and gradually reduce the error of the control signal. Unlike other type of learning-type control strategies, such as adaptive control and neural networks, ILC modifies commands instead of the controller [98]. It has the advantage of fast converge within few cycles.

A classical ILC requires certain conditions [97], [99]:

1. Every cycle ends in a fixed time of duration.

2. Repetition of the initial setting is satisfied. The initial state of the system can be set to the same at the beginning of each iteration.

3. Invariance of the system dynamics is ensured throughout these repeated trials.

4. Output is measured in a deterministic way so that it can be utilised in construction of the next input.

5. The system dynamics are deterministic, that is, no randomness is involved in the development of future states of the system.

In recent studies, some of the conditions are relaxed, such as: the varying cycle lengths are studied in [100]–[102] and nonrepetitive uncertain systems are studied in [103], [104]. Since a gait simulator usually operates in a fixed time interval, ILC can be easily applied. In gait simulator applications, it has been applied in cadaveric gait simulators to control vertical force or tibia loading [71], [75]. In this section, I propose an extended ILC ground reaction force control to generate both required horizontal and vertical forces. It is the first time that ILC is applied on a 2 dimensional contact force control.

4.2.2 PID type of ILC

A PID ILC algorithm is explained here. A typical process of ILC in iterative domain is shown in Figure 4.3.

For the system, the input is $u_j(i)$ and output is $y_j(i)$. The number of iteration is denoted as j, the time discrete index in a cycle is i. The ILC update law is shown as following:

$$u_{j+1} = u_j(i) + \delta u_j(i) \tag{4.1}$$

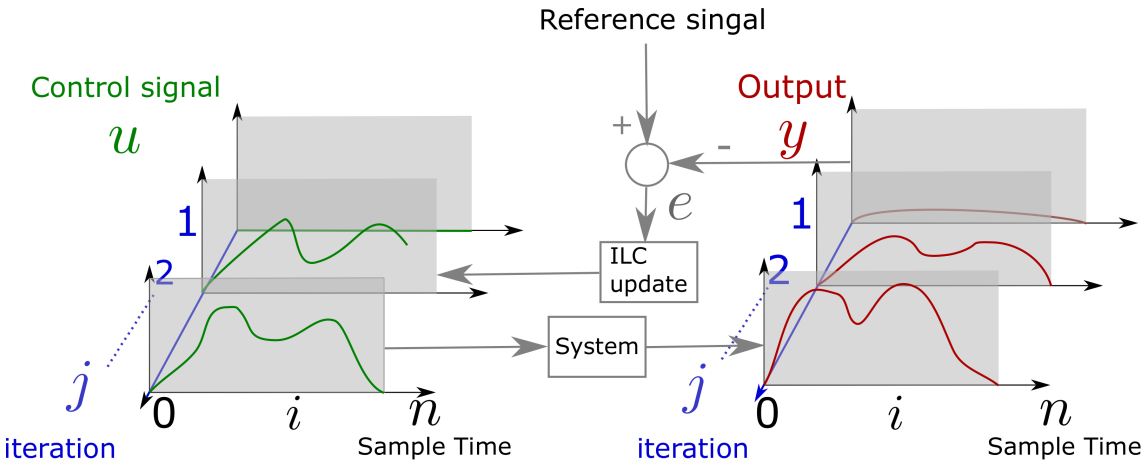

Figure 4.3: Iterative learning control schematic.

where δu_j is the modifier of the controller. For a PID type of ILC, the modifier can be represented as:

$$\delta u_j(i) = k_P e_j(i) + k_I \sum_{m=1}^{i} e_j(m) + k_D(e_j(i+1) - e_j(i)) \tag{4.2}$$

where the error e_j is calculated from:

$$e_j(i) = y_d(i) - y_j(i) \tag{4.3}$$

In Equation 4.2, the modifier has proportional, integral and differential term. Different from the PID definition in classical control theory, the PID terms in ILC control are explained below:

1. Proportional term $k_p e_j(i)$ is proportional to the error at the i time instant from cycle j.

2. Integral term $k_I \sum_{m=1}^{i} e_j(m)$ is proportional to the sum of the error from 1 to i from cycle j.

3. Differential term $k_D(e_j(i+1) - e_j(i))$ is proportional to difference of the error between two time instant $i+1$ and i from cycle j.

The advantages of each term was summarised [105]. The proportional term is the stabiliser role of the ILC. The integral term can reduce the non-zero initial errors (i.e. $e(0) \neq 0$) and increase the convergence rate. Differential term can reduce the disturbance inputs.

4.2.3 Extended ILC ground reaction force control

Description of the problem and variables

In this subsection, the formulation of ILC to control GRF is explained. Traditionally, ILC is used in position control. To achieve the force control, the force and position

relationship during the ground contact is used to convert force demand into position demand. During the stance phase of walk, the prosthesis ankle foot roll over the ground. It means the ankle prosthesis is compressed from different angle as a gait progresses. Thus, the ground contact can be seen as a nonlinear and time-varying spring contact. Here, the ankle prosthetic foot contact with ground is modelled as a time-varying spring, which has two separate stiffness for the horizontal and vertical direction, $k_x^*(i)$, $k_y^*(i)$, where i represents of discrete time instant during a trial, $i \in Z$. The GRF is generated from elastic deformation of the foot. The deformation can be estimated roughly from the relative position of the ground and the ankle point.

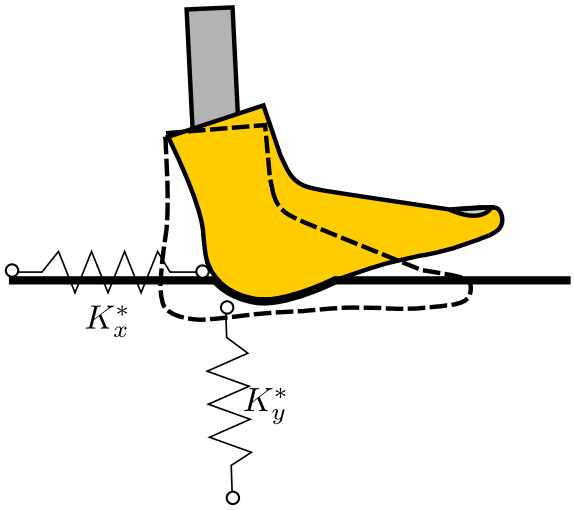

Figure 4.4: Model of foot contact with two independent springs.

Let j denotes the iterative number and n denotes the maximum i. The measured GRF due to the compressed prosthetic foot is defined as discrete variables, $\hat{F_{yj}}_j$ and $\hat{F_{yj}}_j$. They have the same definition as:

$$\hat{F_j} = \begin{bmatrix} F_j(1) \\ F_j(2) \\ \vdots \\ F_j(n) \end{bmatrix} \tag{4.4}$$

Define $\hat{u}_{xj}$ and $\hat{u}_{yj}$ as ankle joint position demand vectors in global coordinates. They have the same definition as:

$$\hat{u_j} = \begin{bmatrix} u_j(1) \\ u_j(2) \\ \vdots \\ u_j(n) \end{bmatrix} \tag{4.5}$$

K_x^* and K_y^* are defined similarly to the diagonal matrix below:

$$K^* = \begin{bmatrix} k^*(1) & & & \\ & k^*(2) & & \\ & & \ddots & \\ & & & k^*(n) \end{bmatrix} \tag{4.6}$$

With these definitions, one can derive a foot contact model to work out the forces at the ankle joint (equivalent to ground reaction force):

$$\begin{cases} \hat{F}_{xj} = K_x^* \hat{u}_{xj} \\ \hat{F}_{yj} = K_y^* \hat{u}_{yj} \end{cases} \tag{4.7}$$

This model is used in the convergence analysis in Section 4.2.4.

Two directional reference force profile vectors are defined as $\hat{F_{xt}}$ and $\hat{F_{yt}}$. The measured forces are $\hat{F_{xm}}$ and $\hat{F_{ym}}$. Then error vectors are then found as:

$$\begin{cases} \hat{e_{xj}} = \hat{F_{xtj}} - \hat{F_{xmj}} \\ \hat{e_{yj}} = \hat{F_{ytj}} - \hat{F_{ymj}} \end{cases} \tag{4.8}$$

Propose controller

In order to generate the desired force profile, an ILC control is proposed in global Cartesian coordinates at the foot contact point. The ILC is applied to work out the required change of motion in global Cartesian coordinates. In the end, the signal is converted into local joint coordinates to be implementable. The process is shown in Figure 4.5.

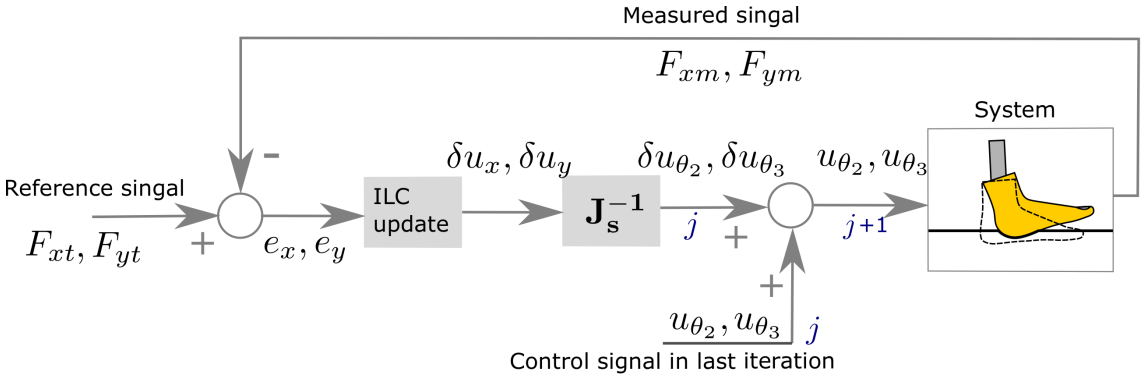

Figure 4.5: Control schematic of proposed EILC force control.

The ILC in the global Cartesian coordinates can is given in Equation 4.9.

$$\begin{cases} \hat{u_{xj+1}} = \hat{u_{xj}} + \delta\hat{u_{xj}} \\ \hat{u_{yj+1}} = \hat{u_{yj}} + \delta\hat{u_{yj}} \end{cases} \tag{4.9}$$

where $\delta\hat{u}_{xj}$ and $\delta\hat{u}_{y_j}$ are modifier terms. The modifier terms are calculated based on proportional-derivative (PD) type ILC controller in Equation 4.10. The reason that PID type is not used is because integral term rejects non-zero initial errors which is not useful in our case [105].

$$\begin{cases} \delta\hat{u}_{xj} = [(P_x + D_x)\boldsymbol{I} - D_x\boldsymbol{H}]\hat{e_{xj}} \\ \delta\hat{u}_{y_j} = [(P_y + D_y)\boldsymbol{I} - D_y\boldsymbol{H}]\hat{e_{y_j}} \end{cases} \tag{4.10}$$

where $\boldsymbol{I}$ is a $n \times n$ identical matrix. $\boldsymbol{H}$ is a $n \times n$ lower triangular matrix defined as below:

$$\boldsymbol{H} = \begin{bmatrix} 0 & & & & \\ 1 & 0 & & & \\ 0 & 1 & 0 & & \\ \vdots & \vdots & \ddots & \ddots & \\ 0 & 0 & \dots & 1 & 0 \end{bmatrix} \tag{4.11}$$

Choice of learning gains and convergence analysis are conducted in Section 4.2.4.

These global inputs modifiers are then converted into local two rotational joint space inputs for joint 2 and joint 3 in Equation 4.12 for every time instant during a iteration.

$$\begin{bmatrix} \delta u_{\theta_2}(i) \\ \delta u_{\theta_3}(i) \end{bmatrix} = \mathbf{J_s^{-1}(i)} \begin{bmatrix} \delta u_x(i) \\ \delta u_y(i) \end{bmatrix} \tag{4.12}$$

where the Jacobian matrix, $\mathbf{J_s}$ is defined in Equation 4.13. S,C represents sin and cos respectively.

$$\mathbf{J_s} = \begin{bmatrix} -l_2S(\theta_2) - l_3S(\theta_2 + \theta_3) & -l_3S(\theta_1 + \theta_2) \\ l_2C(\theta_2) + l_2C(\theta_2 + \theta_3) & l_3C(\theta_2 + \theta_3) \end{bmatrix} \tag{4.13}$$

Finally, the modifiers in local coordinates are added to joint 2 and joint 3 controller commands. In practice, Equation 4.14 is used rather than Equation 4.9.

$$\begin{cases} \hat{u_{\theta 2_{j+1}}} = \hat{u_{\theta 2_j}} + \delta\hat{u_{\theta 2_j}} \\ \hat{u_{\theta 3_{j+1}}} = \hat{u_{\theta 3_j}} + \delta\hat{u_{\theta 3_j}} \end{cases} \tag{4.14}$$

4.2.4 Converge Analysis and Learning Gain Selection

First consider the vertical direction force control. Combining the foot contact model Equation 4.7 and update control law Equation 4.9, the iterative domain error can be derived as:

$$\hat{e_{y_{j+1}}} = \hat{e_{y_j}} - [(P_y + D_y)\boldsymbol{I} - D_y\boldsymbol{H}]K_y^*\hat{e_{y_j}} \tag{4.15}$$

Simplifying Equation 4.15,

$$\hat{e_{y_{j+1}}} = [(1 - (P_y + D_y)K_y^*)\boldsymbol{I} + D_yK_y^*\boldsymbol{H}]^j\hat{e_{y_0}} \tag{4.16}$$

The stability of the controller in iterative domain is then requiring the eigenvalues of $[(1-(P_y+D_y)K_y^*)\boldsymbol{I}+D_yK_y^*\boldsymbol{H}]$ to be smaller than 1:

$$\mid \lambda[(1-(P_x+D_x)K_y^*)\boldsymbol{I}+D_yK_y^*\boldsymbol{H}] \mid < 1 \tag{4.17}$$

Since the matrix is lower triangular matrix, so the condition can be reduced to values on the diagonal:

$$\mid 1-(P_y+D_y)K_y^*(i) \mid < 1 \tag{4.18}$$

A similar criterion of convergence can be derived for horizontal force F_x :

$$\mid 1-(P_x+D_x)K_x^*(i) \mid < 1 \tag{4.19}$$

The stiffness K_x^* and K_y^* are assumed unknown before testing, however the magnitude of the stiffness can be estimated. This condition provides a rough idea where to start with when setting gains for ILC control in experiments. A large value of gains should be carefully avoided. During the experiments, small gains are used to start with and increased carefully within the range of satisfying these conditions.

4.2.5 Noise and Delay Compensation

There is noise on measured signals and delays in actuation of the system. The delay will cause the system to go unstable if not carefully dealt with. For the noise, since the position commands are generated after a cycle is complete, an aggressive low-pass filter can be applied as phase delay can be compensated. The measured signals are filtered and shifted. For the delay in actuation, the updated control signal for the joint position controller is shifted based on the estimated actuation delay. A first order lag is used to model the actuation dynamics. The time constant of these first order lags are used to workout the number of shifted samples for each joints.

A simple example in simulation is given to demonstrate the delay effect in an ILC system. A spring damper mass system is simulated. The mass block is actuated to push against a spring and damper. The spring is $10000\,N/m$ and the damping coefficient is $20\,Ns/m$. A PD ILC update law is given based on Section 4.2 to achieve the required force. The maximum of the sum of P and D term in ILC is calculated to be 10^{-4} based on Equation 4.18. The P and D are selected to be both 5×10^{-5}.

A transfer function is given to represent the actuation part of a spring damper mass system:

$$TF=\frac{-14.75s+1058}{s^2+24.75s+1051} \tag{4.20}$$

One can estimate the system delay of TF by consider TF as a first order lead and second order lag. The system group delay is estimated to be $0.039\,s$, so 39 samples are shifted because the sampling rate is $1000\,Hz$. The ILC is simulated for 15 cycles and the result is shown in Figure 4.8. Without signal shift, the measured force has diverged. On the contrary, with signal shift, the measured force is identical to the target force.

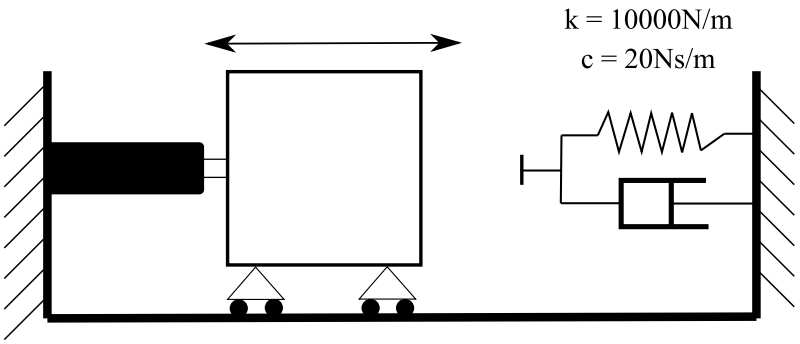

Figure 4.6: A simple spring damper mass system to demonstrate ILC.

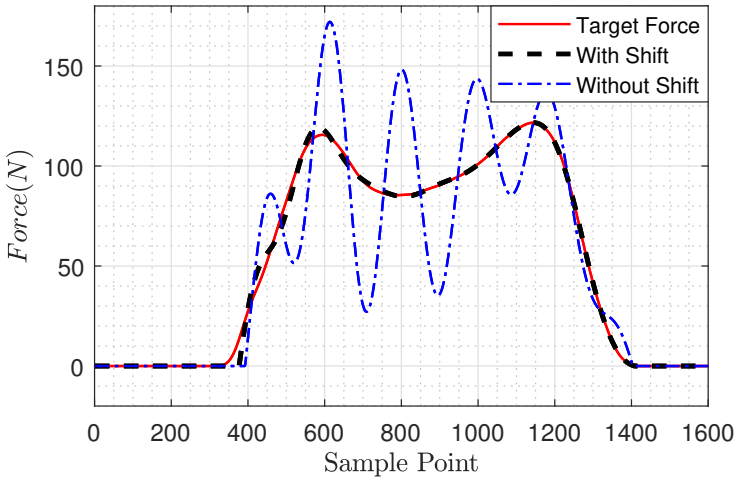

Figure 4.7: Simulated force measurement result after 15 cycles of ILC on spring mass system.

4.3 Limitation of the EILC and impact of using bio-inspired joints

The proposed method has some limitations. During the process of converting global coordinates change to local coordinates change in Equation 4.12, Jacobian matrix is used. The matrix will be singular if the knee joint is at 0° (upright position). From kinematic point of view, the knee joint will have an infinitely large speed command in this case. This will cause control instability which should be carefully avoided. Due to the limit length of the physical robot leg, the required foot position can be out of reach if the hip is too high. In actual experiment, the hip height is tuned so that the knee position can be avoided to be at 0°.

This requirement of not having pin joint at its upright position is common in robotic design. It is quite different from a real human joint. Human joint can be locked at upright position during the stance phase, achieving efficient walking.

Using bio-inspired joints might be able to solve the problem. For example, the four bar mechanism bio-inspired knee joint [106]. In this case, the mechanical energy distribution could be very different from pin joint robot leg gait.

Figure 4.8: A bio-inspired robotic condylar hinge joint [106].

Chapter 5

Experiment setup

This chapter gives a description of the three-axis Hydraulic Gait Simulator (HGS) system which is developed for the validation of the proposed ground reaction control and testing prostheses. Firstly, an overview is provided to introduce the system schematic. Comprehensive description of the HGS including the geometry and specifications is provided in the second section. The third section describes the hydraulic components. After that, the sensors and calibration are explained. In the last section, the signal processing and the real-time test platform are described.

5.1 Overview of the Hydraulic Gait Simulator (HGS)

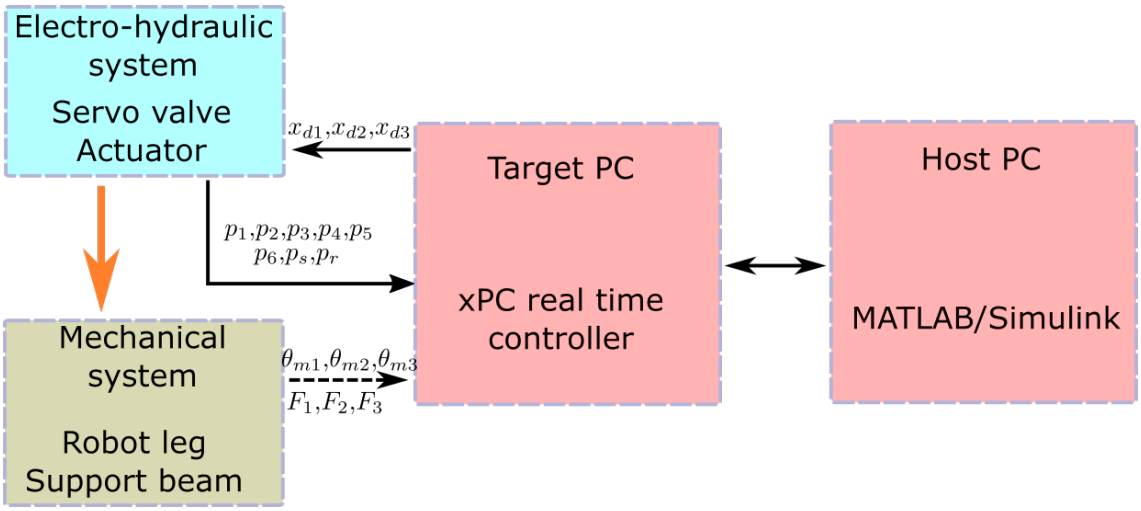

Figure 5.1: Overview of the HGS, brown part is mechanical system cyan part is hydraulic syste and red part is control system.

The HGS has three main parts, mechanical system, eletro-hydraulic system and control system, which is shown in Figure 5.1. The HGS is operated in MATLAB xpc environment. The control program is written in the host PC. It is then compiled in to target PC and run in real time. The target PC transmits three valve demand signals x_{d1}, x_{d2} and x_{d3} to the electro-hydraulic system. Three actuators are driven to actuate the robot leg and the support beam in the mechanical system. The angular positions θ_{m1}, θ_{m2}, θ_{m3} and actuator axial forces F_1, F_2, F_3 are measured and feedback to the target PC. In addition, pressure of the actuators chambers, p_1 to p_6, supply pressure p_s and return pressure p_r are measured to monitor the hydraulic system states.

The mechanical system incorporates a HyQ leg from Italian Institute of Technology (IIT) [107]. I modified the motion range of knee joint to 0° - 90°, which is capable to do a full range knee motion of human gait. The leg is bolted under a beam which can pivot at one end of the beam, which is actuated with a hydraulic actuator at the middle. The beam is able to hold the leg in the air during the swing phase of a walking gait, and it applies vertical load on the foot in the stance phase. The test prosthesis attached at the end of the HyQ leg replaces the original piglet foot. The result mechanical system has three degrees of freedom which are base joint (joint 1), hip joint (joint 2) and knee joint (joint 3).

The hydraulic circuit is shown in Figure 5.3. The system has a fixed displacement gear pump and motor powerpack. It provides a constant pressure and flow to the system. Three servo valves receive analogue voltage signals from the controller. The valves control the flow into the actuators. Three actuators actuate base joint, hip joint and knee joint, see Figure 5.4.

The control system adopts the xPC Target to implement real time control. It complies MATLAB/Simulink model from the host PC to the target PC. Two data

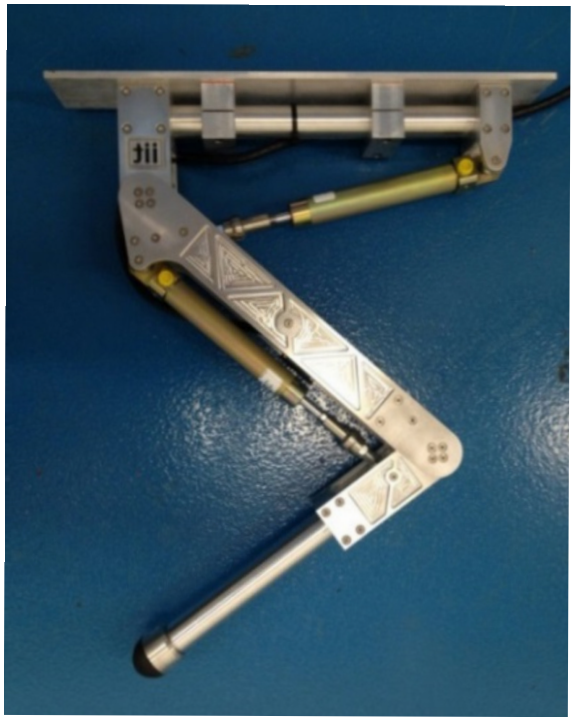

Figure 5.2: The HyQ leg from IIT.

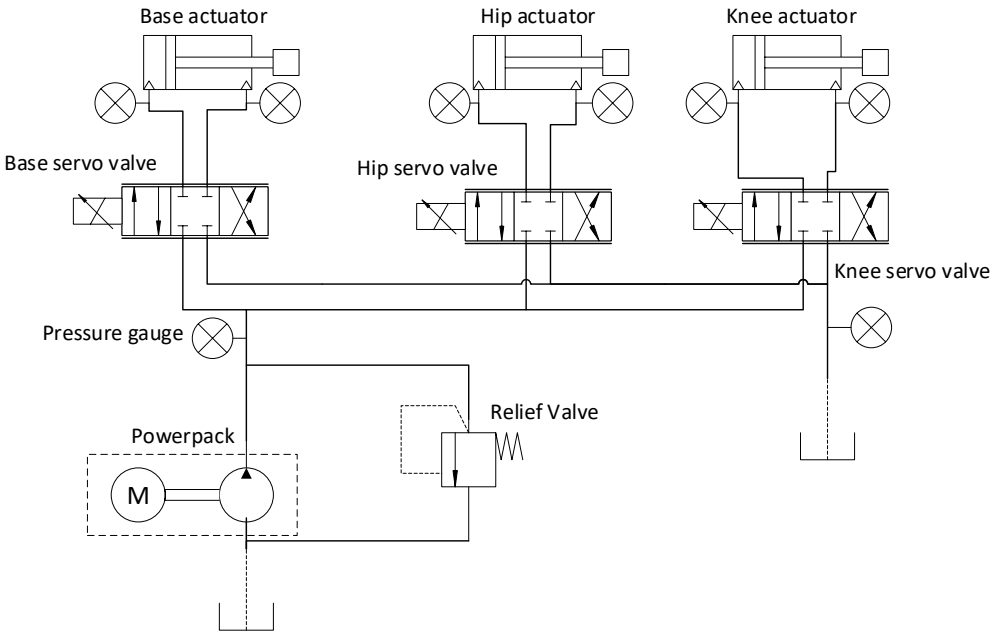

Figure 5.3: Hydraulic circuit of the HGS.

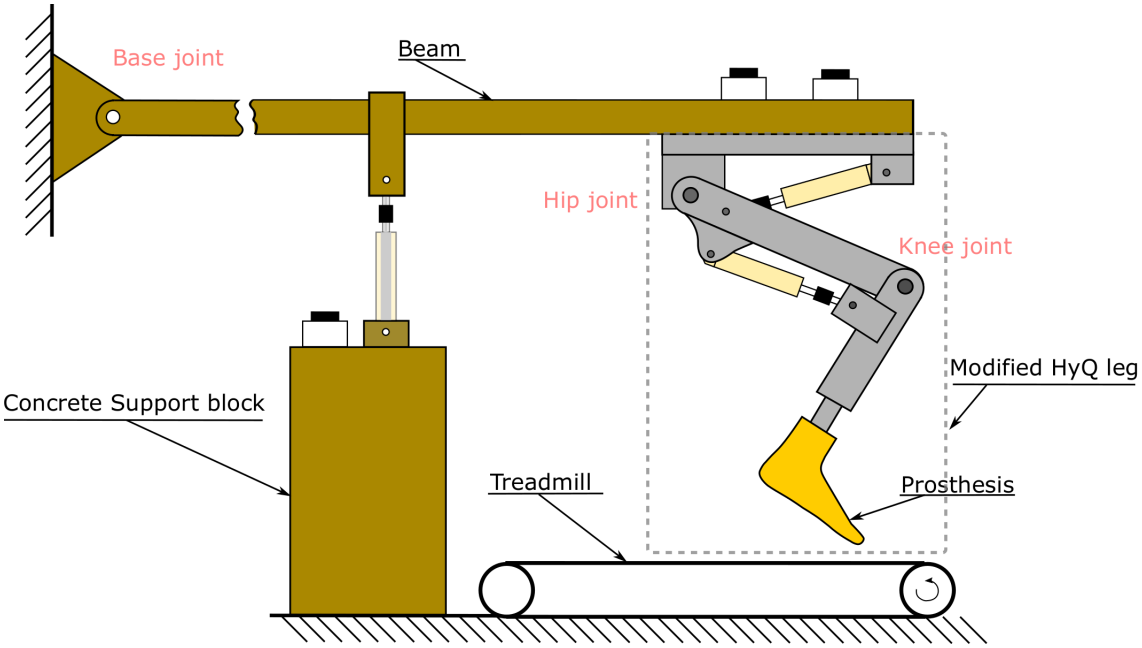

Figure 5.4: Mechanical system schematic of the HGS.

acquisition cards from National Instruments are used in the target PC.

5.2 Hydraulic System

The hydraulic system includes three main parts, powerpack, servo valve and actuators. In this section, the components which are used to build the hydraulic system of the rig are described.

5.2.1 Powerpack

The pump is selected based on the maximum system pressure and maximum system flowrate. The actuators used are incorporated with HyQ leg V2.1, which has the maximum operation pressure is 160 bar, so the powerpack selected should be able to provide at least 160 bar. The minimum flowrate is determined with simulation(See Chapter 6), which is determined to be at least 2 L/m. In our experiments, a fixed displacement gear pump with constant speed motor is sufficient. Thus, a simple powerpack from Rexroth Bosch was selected. The specification is given Table 5.1

Model	**Rexroth Bosch Power Unit**
Operating Pressure Max	250 bar
Flow rate max	5 L/m

Table 5.1: Rexroth Bosch group powerpack specifications.

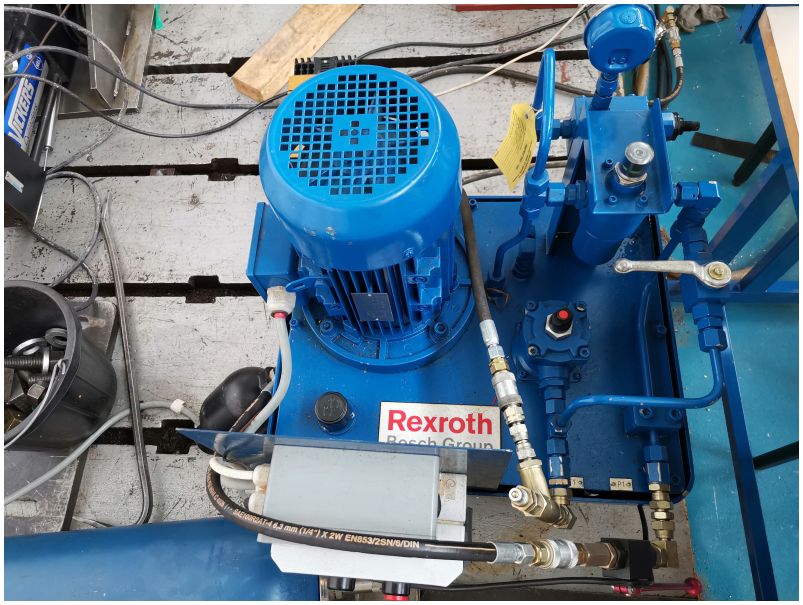

Figure 5.5: Powerpack from Rexroth Bosch group.

5.2.2 Servo Valve

The servo valves used in our research are G760 series from Moog. The valve takes in $\pm 10\,V$ signal, and opens proportionally to the input voltage. The detailed specification is shown in Table 5.2. The frequency response is shown in Figure 5.6. The cut-off frequency is over 100 Hz. It is sufficient for prosthesis testing application of which the typical motion is 1-2 Hz.

Figure 5.6: Moog G760 servo valve.

5.2.3 Actuator

The actuator used in the HyQ leg is Hoerbiger LB6-1610-0080-4M. It is an unequal area cylinder. The stroke is 80 mm. The piston diameter is 16 mm and the rod diameter is 10 mm. The maximum operating pressure is 160 bar. The maximum

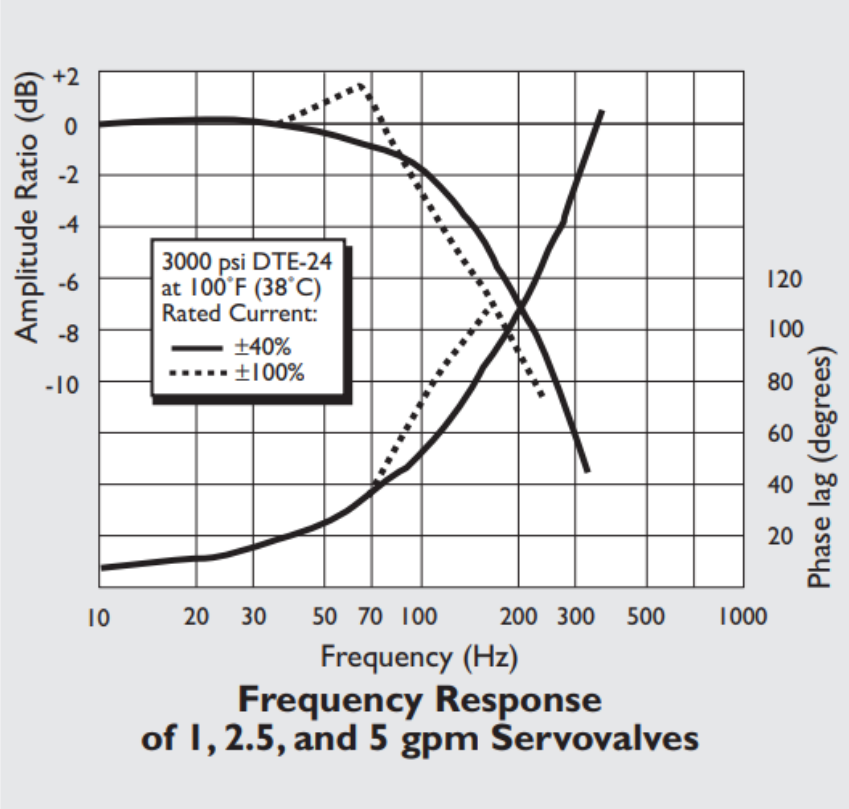

Figure 5.7: Moog servo valve frequency response.

Model	**Moog G760**
Operating Pressure Max	200 bar
Rated Flow@70 bar	9.464 L/m
Hysteresis	3 %
Response Time@250 bar	6 ms

Table 5.2: Moog G760 servo valve specifications.

operating loads on both direction are calculated:

$$F_p = p_{max}(D_p/2)^2 \tag{5.1}$$
$$F_r = p_{max}(D_r/2)^2 \tag{5.2}$$

Figure 5.8: Hoerbiger LB6-1610-0080-4M actuator.

Model	**Hoerbiger LB6-1610-0080-4M**
Type	Single-ended
Stroke	$80\,mm$
Piston/rod diameter	$16mm/10mm$
Piston area	$2.01cm^2$
Annular area	$1.23cm^2$
Max operating pressure	$160\,bar$
Max/Min piston speed	$4\,m/s$
Connection ports	M10 $\times$ 1(metric thread)
Max Load	$3125\,N$ /$1256\,N$

Table 5.3: Hoerbiger LB6-1610-0080-4M actuator specifications.

5.3 Mechanical System

5.3.1 General Description

The mechanical system includes the HyQ robotic leg, beam, support block and a treadmill. I aimed at representing a human leg walking on a treadmill. The HyQ robotic leg is incorporated in our test rig. The HyQ robotic leg is originally designed for the hydraulically-powered quadruped robot (HyQ) robot. The HyQ robot stands 1 meter tall, weighs roughly 90kg. It is a platform to study highly dynamic motions

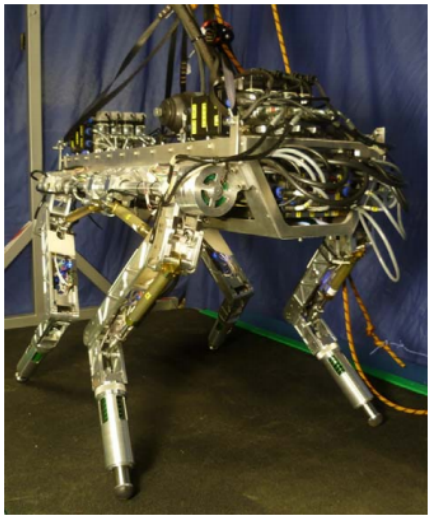

Figure 5.9: HyQ robotic leg in the HyQ robot.

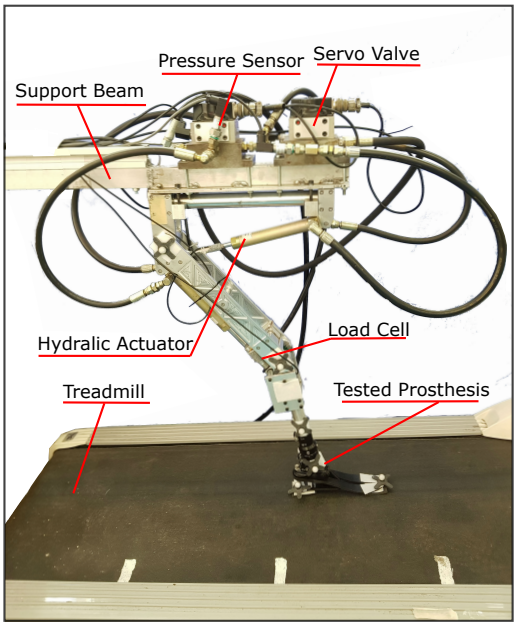

Figure 5.10: Modified HyQ leg in Hydraulic Gait Simulator(HGS).

control and navigation over rough terrains[108]. The Figure 5.9 shows the HyQ leg used in the HyQ robot.

I bolted the HyQ leg under a aluminium beam, the beam is pivoted around its one end on the wall. In the middle of the beam, an actuator is used to support the beam. Along the actuator, a potentiometer displacement sensor is used to measured its length. The length of the actuator can be converted to beam height, see next Subsection 5.3.2. In the hyQ leg, two hydraulic actuators are used to actuate upper and lower joints. Two encoders are integrated into the robot leg hip and knee joints to measure the joint angles. Three strain gauge based force sensors are put in the rod of three actuators to measure the load along the actuators. The rig is capable to simulate prosthesis loading that is representative of human use.

The leg length of the robot is compared with literature in Table 5.4. The shank length of the leg is influenced by the test prosthesis. The total leg length of HyQ is roughly 4/5 of an adult human. To compare the test result between the HGS and human data, the normalised data is used. Normalised data is generated by dividing the measured data with body weight.

5.3.2 Physical parameters and geometry

The physical rig construction and geometry definitions is shown in Figure 5.11 and Figure 5.12. The corresponding detailed parameters and geometry is given in Table 5.5 and Table 5.6. The physical parameters are estimated from modelling and optimisation, see Chapter 6.

Data	Human leg mean data [109]	HyQ (Modified)
Thigh length (m)	0.422	0.350
Shank length (m)	0.434	0.310 (Min)
Total Leg length (m)	0.856	0.660 (Min)
Thigh/Shank ratio (m)	0.972	1.13 (Max)

Table 5.4: HyQ leg sizing compare to human leg.

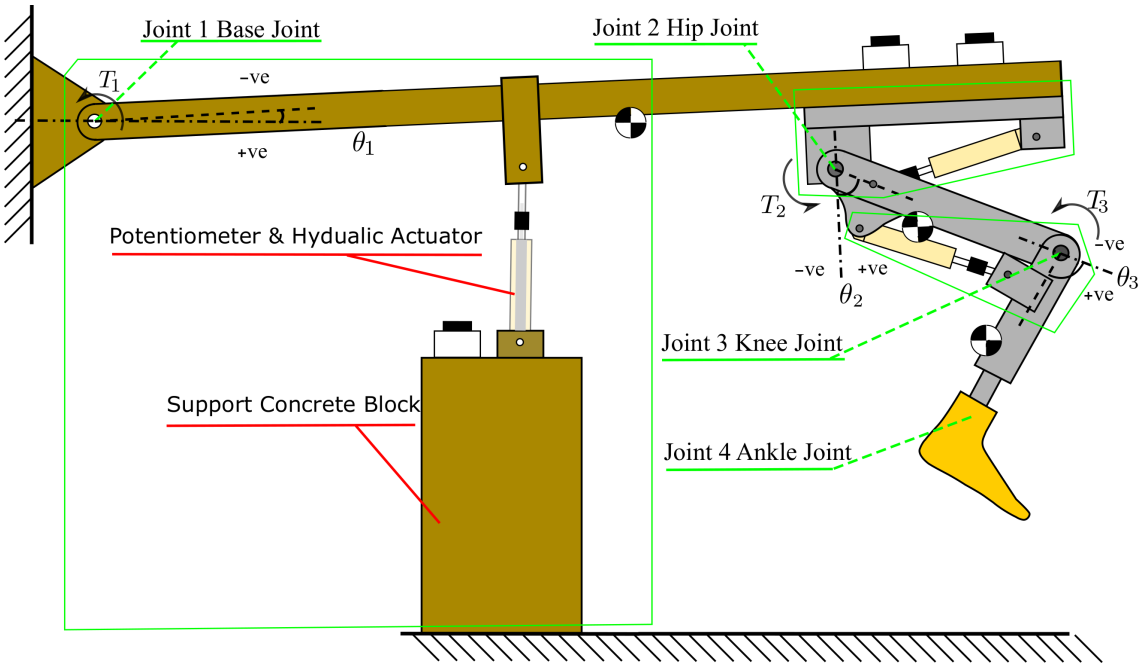

Figure 5.11: HGS mechanical system components and joint definitions.

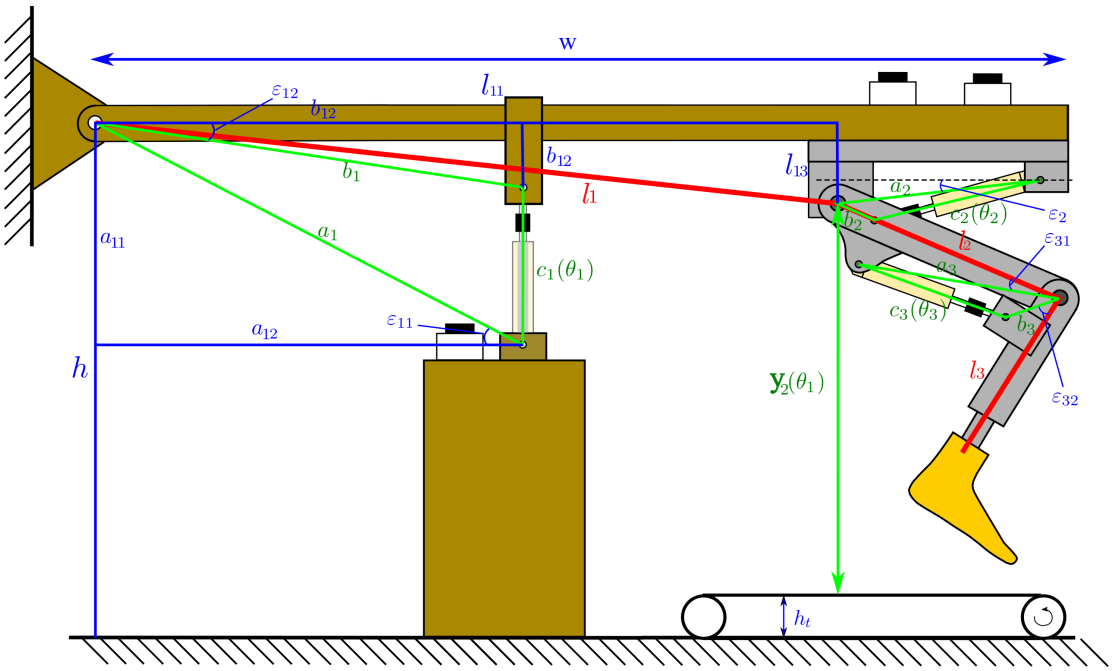

Figure 5.12: HGS mechanical system geometry.

Table 5.5: Physical parameters of the mechanical system.

Physical parameters		
m_1	Link 1 mass	$20.0\,kg$
m_2	Link 2 mass	$1.455\,kg$
m_3	Link 3 mass	$0.6594\,kg$
I_1	Link 1 Moment of Inertia	$26.56\,kg.m^2$
I_2	Link 2 Moment of Inertia	$0.0512\,kg.m^2$
I_3	Link 3 Moment of Inertia	$0.0331\,kg.m^2$
D_1	Joint 1 damping	$110.6\,N.s/m$
D_2	Joint 2 damping	$1.109\,N.s/m$
D_3	Joint 3 damping	$0.3419\,N.s/m$

Overall Sizing			
l_{11}	$1.444\,m$	l_{13}	$0.15\,m$
l_1	$1.45\,m$	l_2	$0.35\,m$
l_3	$0.31\,m$	h	$1.032\,m$
w	$1.844\,m$	h_t	$0.16\,m$
Joint 1 Base Joint			
a_{11}	$0.380\,m$	a_{12}	$0.642\,m$
a_1	$1.032\,m$	b_{11}	$0.060\,m$
b_{12}	$0.652\,m$	b_1	$0.655\,m$
ε_{11}	5.26°	ε_{12}	30.62°
Joint 2 Hip Joint			
a_2	$0.3219\,m$	b_2	$0.0450\,m$
ε_2	6.24°		
Joint 3 Knee Joint			
a_3	$0.3218\,m$	b_3	$0.0491\,m$
ε_{31}	8.04°	ε_{32}	44.96°

Table 5.6: The dimensions of the HGS mechanical system.

5.3.3 Motion range and the maximum load

The hydraulic actuators drive three revolute joints. The relationship between the actuator length and joint angle needs to be determined. The motion range of the hip height, hip joint angle and knee joint angle should be able to cover human walking corresponding kinematics. For the base joint, it is important to decide the appropriate height h and distance between pivot point and actuation support point b_{12}, a_{12} to allow the robot leg walk on the treadmill and provide enough vertical load on the leg.

The Equation 5.3, 5.4 and 5.5 describes the relationship between joint angles and actuator lengths. The motion range is presented in Table 5.7. The result joint 1 range is from $-3.53°$ to $3.49°$. This angle is corresponding hip height from $0.663\,m$ to $0.810\,m$. This hip height lower than normal human walking hip height because the leg length is shorter than human adults. The hip height range of the test rig is enough to simulate human walking hip motion which has about $0.04\,m$ movement in vertical direction [110].

$$c_1(\theta_1) = \sqrt{a_1^2 + b_1^2 - 2a_1 b_1 \cos(\theta_1 + \varepsilon_{11} - \varepsilon_{12})} \tag{5.3}$$

$$c_2(\theta_2) = \sqrt{a_2^2 + b_2^2 - 2a_2 b_2 \cos(\pi/2 - \theta_2 + \varepsilon_2)} \tag{5.4}$$

$$c_3(\theta_3) = \sqrt{a_3^2 + b_3^2 - 2a_3 b_3 \cos(\pi - \theta_3 - \varepsilon_{31} - \varepsilon_{32})} \tag{5.5}$$

The hip height range can be roughly calculated by Equation 5.6:

$$y_2(\theta_1) \ = h - h_t - l_{13} + l_{11} cos\theta_1 \tag{5.6}$$

	Joint 1 Base Joint	
$c_1(\theta_1)$	$0.28\,m$	$0.36\,m$
θ_1	-3.53°	3.49°
$y_2(\theta_1)$	$0.633\,m$	$0.810\,m$
	Joint 2 Hip Joint	
$c_2(\theta_2)$	$0.2822\,m$	$0.3602\,m$
θ_1	70°	-50°
	Joint 3 Knee Joint	
$c_3(\theta_3)$	$0.2841\,m$	$0.3535\,m$
θ_3	90°	0°

Table 5.7: The motion range of the HGS mechanical system.

Torques at the joints are not measured directly, forces measured along the actuators with strain gauges can be converted to torques using Equation 5.7, 5.8 and 5.9.

$$T_1 = F_1 a_1 \sin(\cos^{-1}(\frac{a_1^2 + c_1^2 - b_1^2}{2a_1 c_1})) \tag{5.7}$$

$$T_2 = F_2 a_2 \sin(\cos^{-1}(\frac{a_2^2 + c_2^2 - b_2^2}{2a_2 c_2})) \tag{5.8}$$

$$T_3 = F_3 a_3 \sin(\cos^{-1}(\frac{a_3^2 + c_3^2 - b_3^2}{2a_3 c_3})) \tag{5.9}$$

The maximum load that the test rig can apply to the test prosthesis is determined by joint 1. The free body diagram of the test rig in swing and stance phase is shown in Figure 5.13. Neglecting the inertia generated from the dynamics of the rig, in the swing phase, the joint 1 actuator acts as a support to hold the test rig own weight. In the stance phase, the joint 1 in applying a downwards force on the robot leg. The maximum force that possible on the joint 1 is calculated by Equation 5.10.

$$\begin{cases} F_1 b_{12} = G_t l_g & \text{Swing phase} \\ F_1 b_{12} = F_y l_{11} - G_t l_g & \text{Stance phase} \end{cases} \tag{5.10}$$

G_t is the total rig weight. the horizontal moment arm the total rig weight l_g is estimated to be roughly $w/2$. The maximum weight of the rig is determined by Equation 5.11. The maximum extension load is $3125\,N$, so the maximum rig weight is calculated to be $2218\,N$. The maximum load can be applied during the stance phase is estimated with Equation 5.12. The maximum retraction of the actuator is $1256\,N$. So, the maximum load that can be applied on foot is calculated to be $1076\,N$. The peak of a $70\,kg$ male man walking vertical ground reaction force is around $800\,N$. It is safe to say, the test rig is able to simulate adult walking of an average weight.

$$G_t = \frac{F_{emax} b_{12}}{l_g} \tag{5.11}$$

$$F_y = \frac{F_{rmax} b_{12} + G_t l_g}{l_{11}} \tag{5.12}$$

Actuator max extension load	$3125\,N$	Max rig weight	$226\,kg$
Actuator max retraction load	$1256\,N$	Max load apply on the leg	$1076\,N$

Table 5.8: Load limits of the HGS.

5.4 Sensors

5.4.1 Pressure transducer

The pressure sensors are used monitor the system states to avoid cavitation. Also, it was used to calibrate force sensors as well as estimate actuator frictions. Keller

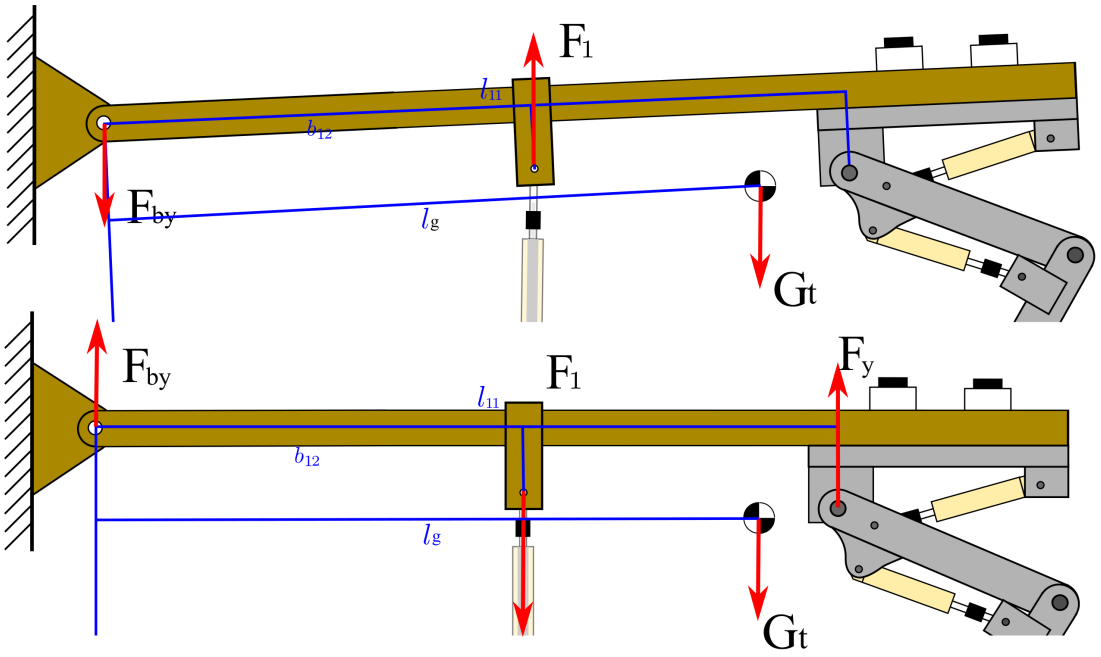

Figure 5.13: Free body diagram of swing and stance phase.

PA-21Y series transducers are used to measure supply pressure, return pressure and both chamber pressures of three actuators. The specifications are listed in Table 5.9.

Figure 5.14: Keller PA-21Y series pressure transducer [111].

5.4.2 Encoder

The encoders are used to measure knee and hip joint angles. AVAGO AEDA-3300-BE1 encoder is used. It is a three-channel optical incremental encoder and

Model	Keller PA-21Y
Operating Pressure Max	200 bar
Output Voltage	0...10 V
Accuracy	0.25%
Port style	G1/4 BSP
Storage-/Operating Temperature	40...100 ℃
Response Time	$< 5\,ms$

Table 5.9: The specifications Keller PA-21Y pressure transducer.

ultra-miniature (diameter 17 mm) which is easy to be mounted in the joints.

Figure 5.15: AVAGO AEDA-3300-BE1 encoder.

Model	AVAGO AEDA-3300-BE1
Counts per revolution	20000 (80000 counts with 4X decoding)
Principle of operation	Optical disc
Output signal Three digital channels	A, B and index Z
Power supply	5V
Max rotational speed	12000 RPM

Table 5.10: The specifications of AVAGO AEDA-3300-BE1 encoder.

5.4.3 ATI 6 axis force sensor

I use an ATI 6 axis force transducer to verify stationary GRF control and verify actuator load cell calibrations. The ATI sensor is shown in Figure 5.16. The specification of the transducer is given in Table 5.11.

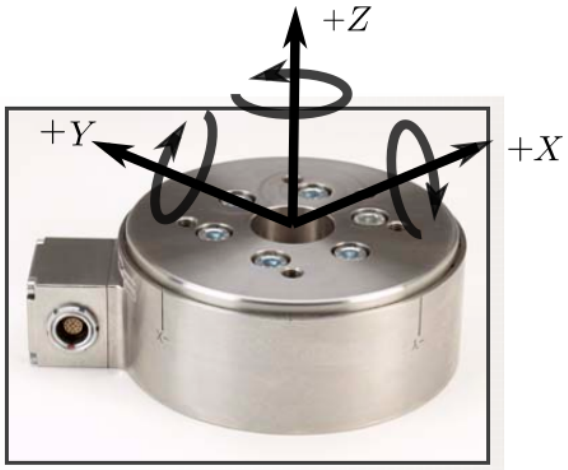

Figure 5.16: ATI Omega160 IP65/IP68 [112].

Model	**Omega160 IP65/IP68**
F_x, F_y	$\pm 2500\,N$
F_z	$\pm 6250\,N$
T_x, T_y, T_z	$\pm 6250\,N$
Weight	$7.26\,kg$
Diameter	$165\,mm$
Height	$65.9\,mm$

Table 5.11: The specifications of ATI Omega160 IP65/IP68 6 axis transducer.

5.4.4 Force sensor

Force sensors are made in full bridge strain gauges. It is placed to connect the rod ends and actuator rods, Figure 5.17. They are used to measure the actuator axial forces which can be converted to joint torques.

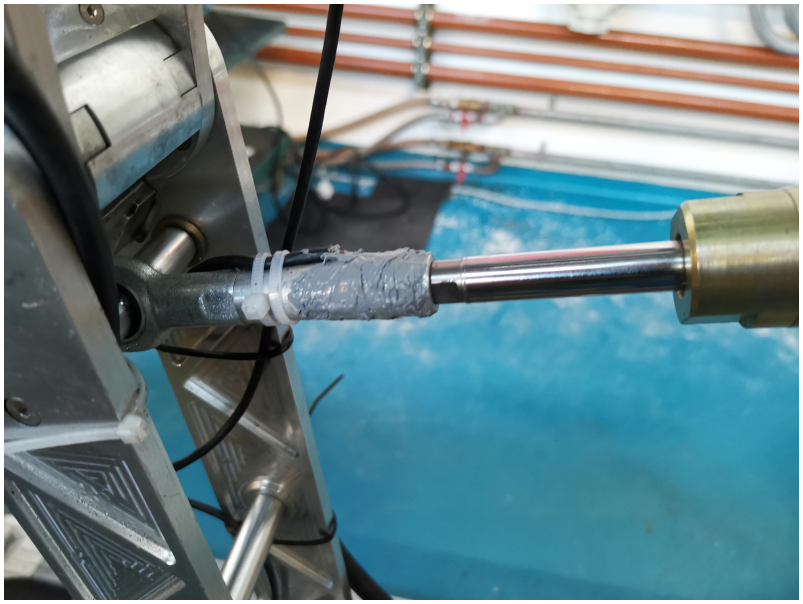

Figure 5.17: Full bridge force sensor covered in silica gel.

Force sensor calibration

The sensor calibration is not carried out on a material testing machine traditionally. It is because the installation process of the aluminium connector which has the strain gauges on will have slight deformation due to the tightening of the connection. So, the force sensors are calibrated with a optimisation process after they have been mounted on the rig. Random motion signals are transmitted to the HGS. The pressures at both sides of the actuators are measured using pressure gauges described in Section 5.4.1. With these measured pressures, the force provided from hydraulic force can be worked out with Equation 5.13.

$$F_h = P_p A_p - P_r A_r \tag{5.13}$$

F_h is calculated hydraulic force. P_p is piston side chamber pressure of the actuator. P_r is annulus side chamber pressure of the actuator. The force balance along the actuator is:

$$F_l = F_h - F_f \tag{5.14}$$

where F_l is the measured force from load cell. F_f is friction force.

Equation 5.15 gives the relationship between force sensor voltage and its measurement. F_l is calculated with K_l the gain of load cell and D_l is the offset of load cell.

$$F_l = K_l \cdot V_l + D_l \tag{5.15}$$

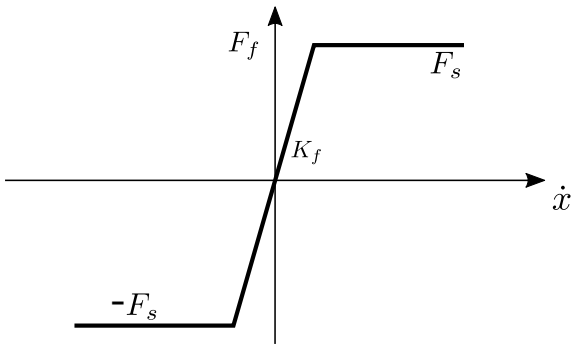

Figure 5.18: Viscous and coulomb friction model.

The friction in the actuator is modelled in Equation 5.16:

$$F_f = \begin{cases} sign(\dot{x}) \cdot K_f \cdot \dot{x} & |K_f \cdot \dot{x}| < F_s \\ F_s & |K_f \cdot \dot{x}| >= F_s \end{cases} \tag{5.16}$$

where $\dot{x}$ is the piston velocity. K_f is friction coefficient. F_s is the maximum static friction.

The function in Equation 5.17 is used to run optimisation. The sum of actuator friction and measured force in load cell should equals to hydraulic force. 4 parameters K_l, D_l, K_f, F_s are optimised to make $f(K_l, D_l, K_f, F_s)$ as close to 0 as possible.

$$\begin{aligned} f(K_l, D_l, K_f, F_s) &= F_h - F_f - F_l \\ &= P_p \cdot A_p - P_r \cdot A_r - F_f - K_l \cdot V_l - D_l \end{aligned} \tag{5.17}$$

Calibrated result is shown in Figure 5.19 and Table 5.12. From the result, one can see that the friction coefficient is big enough to have instant change. The static friction agrees with previous research on the same actuator. In [113], the friction was found by calculating the pressure increase while the piston is stalled.

Force sensor calibration result				
Joint	Load cell gain	Offset	Friction coefficient	Static Friction
Base Joint	$299.05\,N/V$	$-23.31\,N$	$-8.00 \times 10^4\,N/\dot{m}$	$28.74\,N$
Hip Joint	$360.30\,N/V$	$-105.98\,N$	$7.48 \times 10^5\,N/\dot{m}$	$39.61\,N$
Knee Joint	$-295.07\,N/V$	$-43.31\,N$	$5.01 \times 10^4\,N/\dot{m}$	$41.98\,N$

Table 5.12: The result of force sensors optimisation.

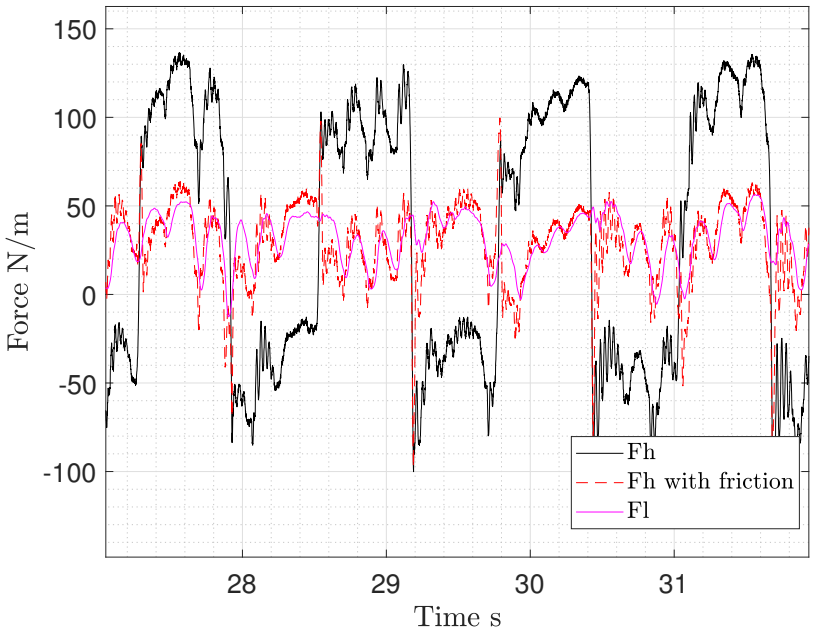

Figure 5.19: Optimisation result of knee joint force sensor. The hydraulic force, hydraulic force with friction and load cell reading are shown.

5.4.5 Ground Reaction Force (GRF) Measurement

The HGS walks on a treadmill. Forces from the ground will apply to the foot during the test. The forces from the ground can be converted to F_x, F_y and T_z equivalently at the ankle joint of a tested prosthesis. Finding a suitable size of multi-axis force sensor on the required position is challenging. So in this thesis, an indirect measurement of forces applying Jecobian transformation matrix is developed. The HGS has three degrees of freedom, which means the three forces around prosthesis ankle point can be measured indirectly through measuring the torques of joint 1, joint 2 and joint 3. The force definition is shown in Figure 5.20.

The external force at joint 4 due to the contact from the ground is defined as a column vector in Equation 5.18:

$$\mathbf{F_4} = \begin{bmatrix} F_x \\ F_y \\ T_z \end{bmatrix} \tag{5.18}$$

Ignoring the inertia of the foot, the GRF equals to the F_4 in horizontal and vertical direction. The T_z is related to the position of the centre of pressure under the prosthesis. The $\mathbf{F_{GRF}}$ is:

$$\mathbf{F_{GRF}} = \begin{bmatrix} F'_x \\ F'_y \end{bmatrix} = \begin{bmatrix} F_x \\ F_y \end{bmatrix} \tag{5.19}$$

The system dynamics model can be written with Lagrangian motion equation. (the detailed model is presented in Chapter 6):

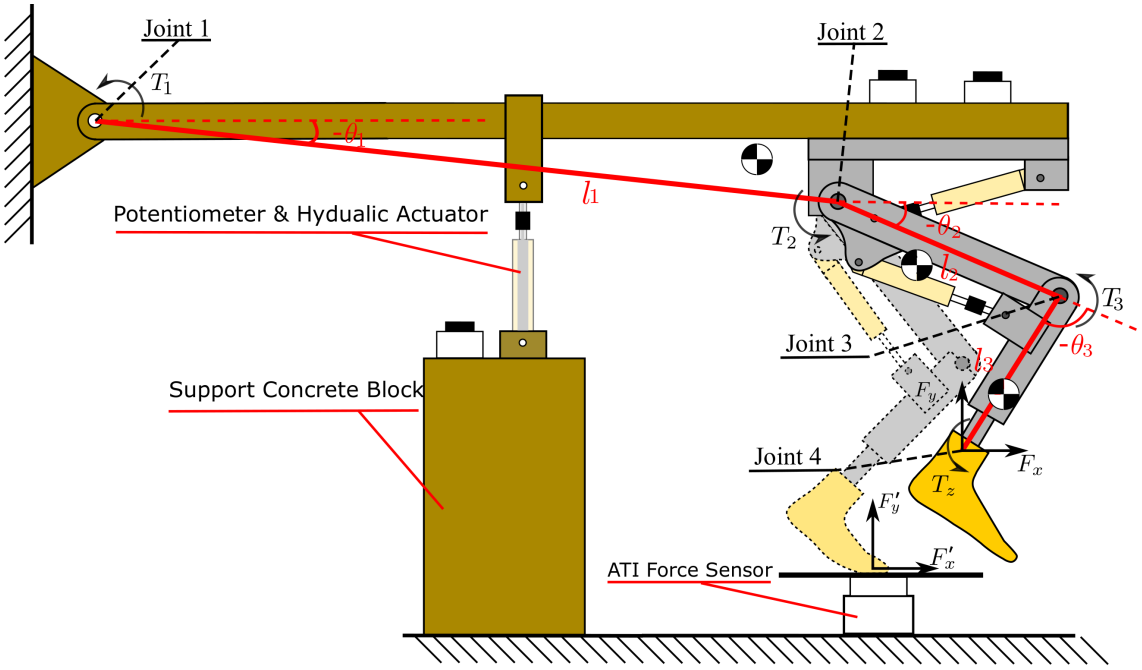

Figure 5.20: Experiment of verify GRF measurement. The physical parameters are defined in the diagram. 4 points are marked out, which are beam pivot point, hip point, knee point and ankle point respectively. Three parts of masses and inertia are shown in the rig.

$$\mathbf{M}(\mathbf{q}) \cdot \ddot{\mathbf{q}} + \mathbf{C}(\mathbf{q}, \dot{\mathbf{q}}) + \mathbf{G}(\mathbf{q}) = \mathbf{Q_u} \tag{5.20}$$

Where $\mathbf{M}(\mathbf{q})$ represents mass matrix, $\mathbf{C}(\mathbf{q}, \dot{\mathbf{q}})$ is centrifugal and coriolis torques and $\mathbf{G}(\mathbf{q})$ is gravity forces. $\mathbf{Q_u}$ is the required torque input of the rig. The model parameters is calibrated dynamically so that $\mathbf{Q_u}$ can be worked out relatively accurate. The measured torque is the sum of model predicted torque and torque caused by external loads:

$$\mathbf{Q_m} = \mathbf{Q_u} + \mathbf{Q_e} \tag{5.21}$$

where $\mathbf{Q_m}$ is measured torque. $\mathbf{Q_e}$ is the generalised external torque from the impact of the ground , i.e. the GRF. With inverse dynamics process, $\mathbf{Q_u}$ can be calculated with Equation 5.20. Then after measuring the forces along the actuators, the $\mathbf{Q_e}$ can be then worked out:

$$\mathbf{Q_e} = \mathbf{Q_m} - \mathbf{Q_u} \tag{5.22}$$

Applying Jacobian force transformation, the forces at joint 4 can be derived:

$$\mathbf{F_4} = \mathbf{J^T} \cdot \mathbf{Q_e} \tag{5.23}$$

where Jacobian matrix definition can be found in Appendix.

In the end, a filter with cut-off frequency of 5 Hz is applied on the measurement to filter out high frequency noise which comes from the mechanical vibration introduced

by the rig especially when the robot leg is lifting in the air. It works because an iterative learning control is applied (Section 4.2.3), which updates offline, so that the delay caused by the filter can be compensated. The HGS is controlled to push against a 6 ATI force sensor to verify the proposed approach of force measurement. The result is shown in Figure 5.21. Since the T_z measurement from the ATI sensor is related to the contact point on the sensor, it is hard to compare the results. The other two forces are proven to be reasonable close to ATI forces measurement.

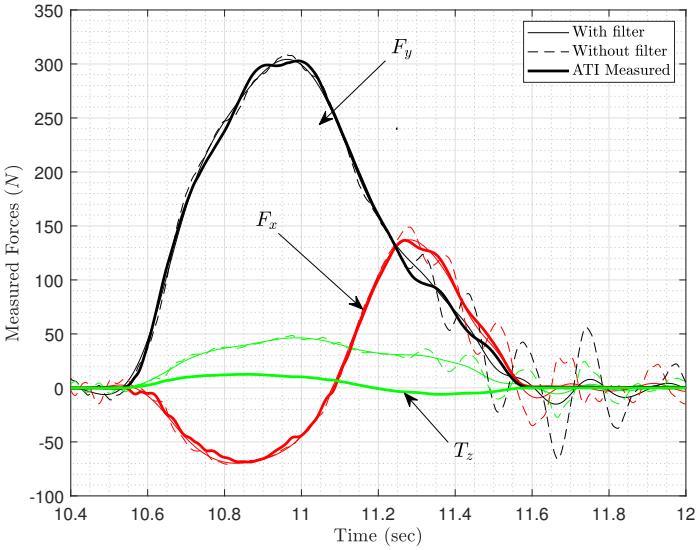

Figure 5.21: Results of two measurement methods. Red lines represent F_x. Black lines represent F_y. Green lines represent T_z. Thin lines are filtered F_j. Dashed lines are original F_j and thick solid lines are forces measured by ATI 6 axis forces sensor. The filtered F_j and ATI measured forces are close to identical apart from T_z.

5.5 Data Acquisition and Control

The control system is built with MATLAB/Simulink Real-Time platform. A host PC is used to build the system model. The model is then complied in C language and downloaded to the target PC. The target PC sends out and receives the signals with the physical system by data acquisition cards. The controller runs in $1000\,Hz$. This section will introduce the interfacing and the EILC implementation.

5.5.1 Data acquisition card and specifications of signals

Data acquisition is run by two data acquisition boards NI PCI-6221 (37pin) from National Instruments, Figure 5.22. Each data acquisition card has 16 analogue input channels (range option:$\pm 10\,V$, $\pm 5\,V$,$\pm 1\,V$ and $\pm 0.5\,V$), 2 analogue outputs ($\pm 10\,V$) and two encoder channel. They are inserted into the target PC's PCI slots.

Each board has its individual connector block for signal wiring. The detailed pin allocation is described in Table 5.13.

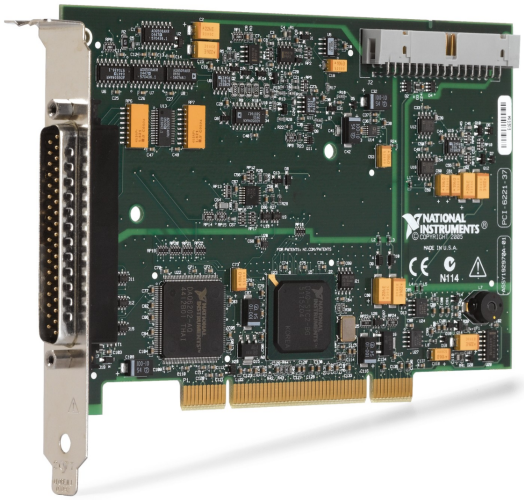

Figure 5.22: NI PCI-6221 (37pin) data acquisition card.

Data acquisition card 1 Analog Input AI			
AI 0	Base potentiometer	AI 1	Base actuator force
AI 2	Hip actuator force	AI 3	Knee actuator force
AI 4	Actuator 1 piston side pressure	AI 5	Actuator 1 annulus side pressure
AI 6	Actuator 2 piston side pressure	AI 7	Actuator 2 annulus side pressure
AI 8	Actuator 3 piston side pressure	AI 9	Actuator 3 annulus side pressure
AI 14	Supply pressure	AI 15	Return pressure
Data acquisition card 1 Analog Output AO			
AO 0	Hip joint servo valve	AO 1	Knee joint servo valve
Data acquisition card 2 Analog Input AI			
AI 0-5	ATI 6 axis force sensor		
Data acquisition card 2 Analog Output AO			
AO 1	Base joint servo valve		
Data acquisition card 2 Encoder			
ENC 0	Hip joint	ENC 1	Knee joint

Table 5.13: Pin allocation of two NI PCI-6221 data acquisition card. Actuator 1,2,3 refers to base joint, hip joint and knee joint.

5.5.2 Implementation of EILC

Iterative learning control updates the command signal after each cycle of motion is finished. So, layers of control are presented. The top layer control is an iterative learning control (ILC) in the host PC, where a reference GRF is taken in. An updated position command is then generated and sent to a lower layer controller in the target PC. In the target PC, a PI position controller generates signals to hydraulic servo valves in the physical system. The HGS executes the required motion. Motion and forces are measured and feedback to the top and low layer controllers. The control block diagram is shown in Figure 5.23.

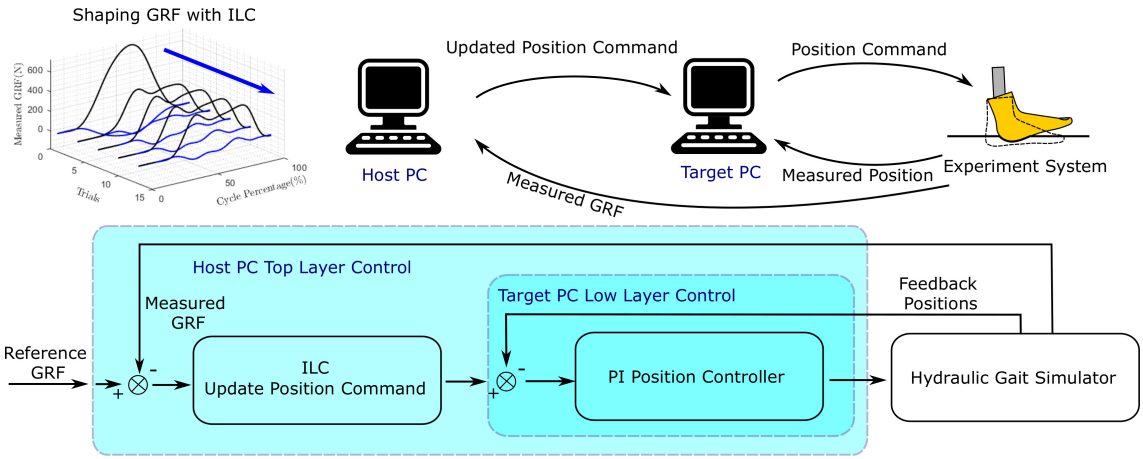

Figure 5.23: The implementation of EILC in the test rig.

5.5.3 HGS state machine

The state machine of HGS is shown in Figure 5.24. There are 4 states for the HGS, Initialisation, Execute, Homing, Finishing in the Target PC. The command update is executed in the Host PC. The conditions of changing states are presented in blue. Position tracking error is not zero when the robot is moving.

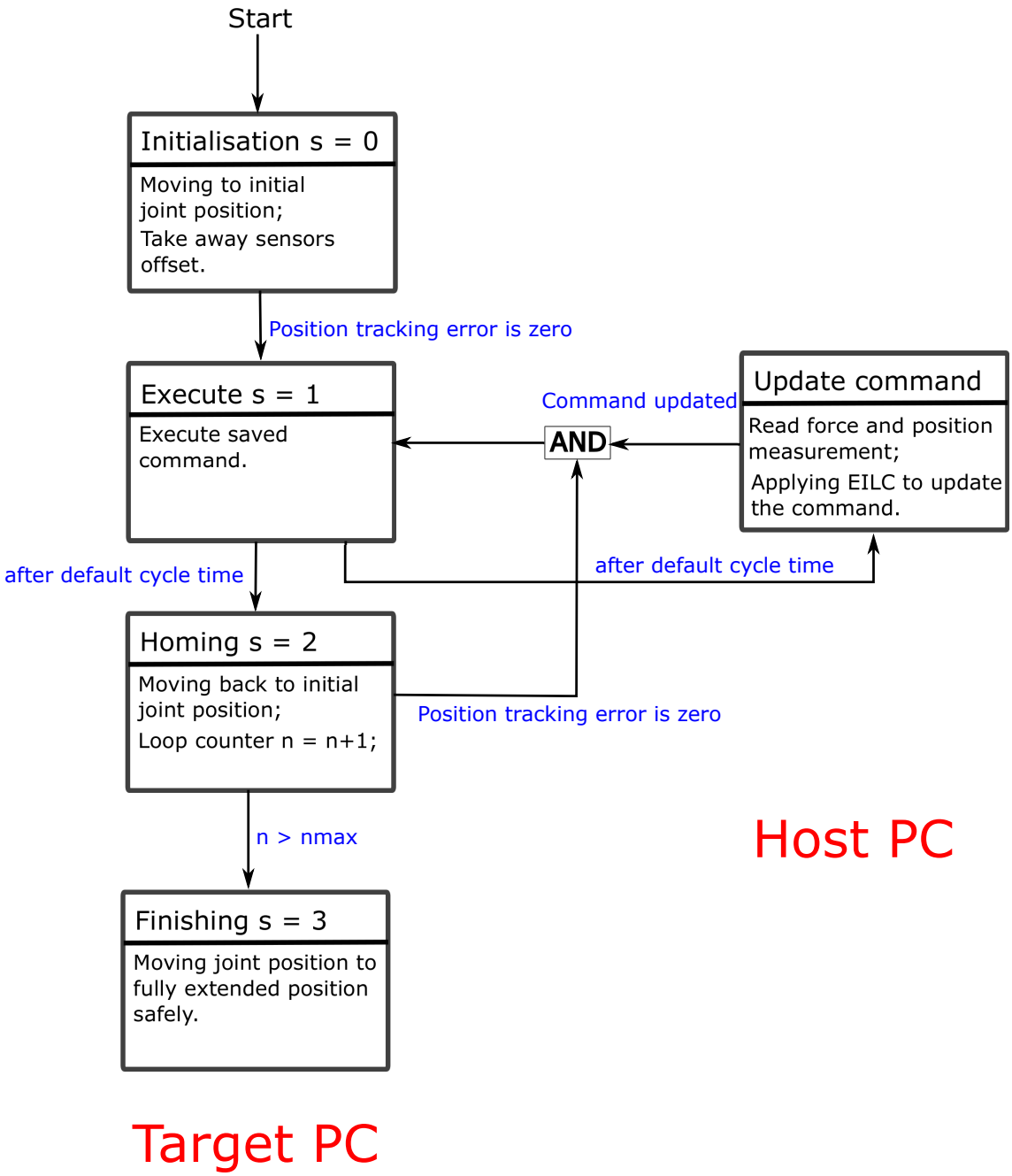

Figure 5.24: State machine of the HGS.

Chapter 6

System Modelling

This chapter introduces the modelling of the system. The overall construction of the system model is outlined first. Then the model is explained in three parts: hydraulic model, mechanical model and controller. The system model is used to verify the developed control strategy before I implement it on the real experiment rig. In addition, the modelling system is useful to predict some critical system physical values to help decide experiment size. e.g hydraulic system total flow rate in the simulation is used to choose the pump size.

6.1 Overview

The system model includes three parts, controller, hydraulic system and mechanical system. The PI type position controller transmits valve signals into hydraulic system. The hydraulic system output the force and drive the mechanical system. The mechanical system uses forces and integrate motion equations to get actual joint positions. The joint positions are then feedback to the controller and hydraulic system. The overall model construction is shown in Figure 6.1.

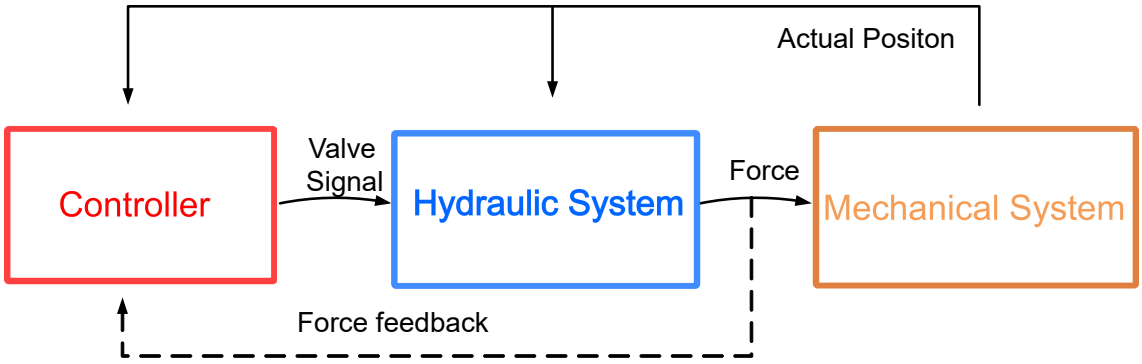

Figure 6.1: Hydraulic Gait Simulator (HGS) overall model construction.

6.2 Mechanical System Model

The robot is modelled with two approaches and they are compared with each other to verified the model accuracy. The first approach is Lagrangian equation of motion. This approach takes relatively low computational power. It is used in real time controller to work out ground reaction force (See Section 5.4.5). The second approach is Simscape Multibody tool. It is a multibody simulation environment for 3D mechanical systems within MATLAB/Simulink. I use the Simscape Multibody as a main simulation develop tool.

The mechanical system model includes three main parts, 3 link robot model, prosthesis model and ground contact model. The prosthesis model is a subsystem of the 3 link model.

3 Link robot model

Lagrangian motion equation model takes less computational power compare to Simscape multibody model. I use the model to optimise the physical parameters. The ground contact model is not included here. The gait simulator rig can be considered as a three-link robot which has three degree of freedom, Figure 6.3. θ_1, θ_2, θ_3 are chosen to be generated coordinates.

The model has damping D_1, D_2 and D_3 for each joint. At joint 2, two big hoses of the actuator 2 bend when the joint is rotating. The hoses are modelled as a spring around joint 2 which the stiffness of K_2 balanced at θ_{20}. Each joint has its own mass and moment of inertia. The centre of mass is described by each local coordinates

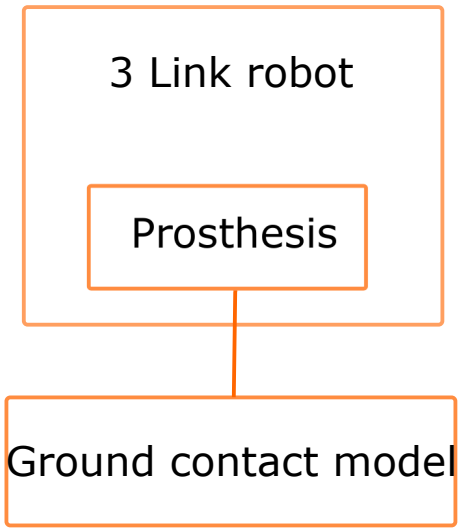

Figure 6.2: Overview of the mechanical system model.

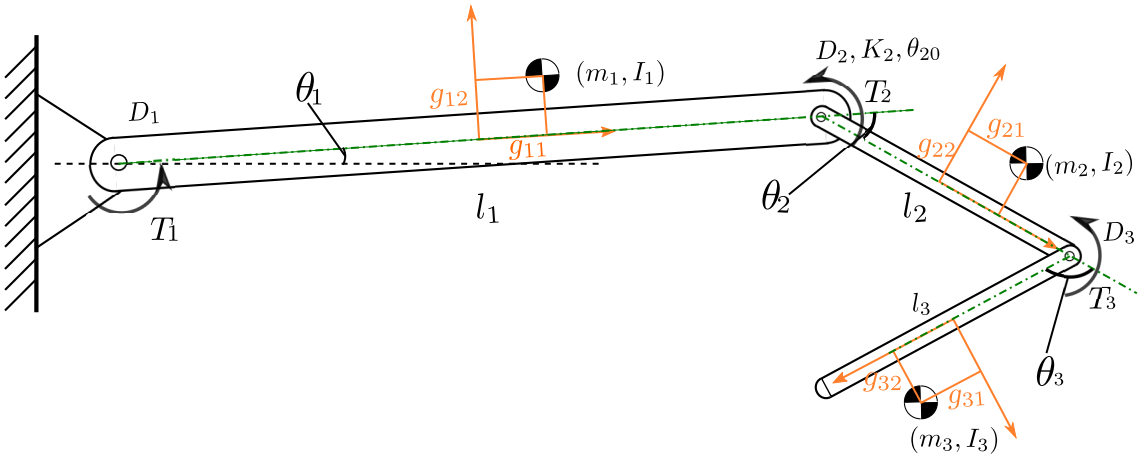

Figure 6.3: Mechanical system model diagram.

frame. The origins of these coordinates frame lie at the geometric centre of each link.

The motion equation for the system is modelled traditionally with standard Euler Lagrange equation like Equation 6.1.

$$\frac{\mathrm{d}}{\mathrm{d}t}\left(\frac{\partial L}{\partial \dot{q}_i}\right) - \frac{\partial L}{\partial q_i} = Q_i, \qquad i = 1...N \tag{6.1}$$

$$\mathbf{M}(\mathbf{q}) \cdot \ddot{\mathbf{q}} + \mathbf{C}(\mathbf{q}, \dot{\mathbf{q}}) + \mathbf{G}(\mathbf{q}) = \mathbf{Q_u} \tag{6.2}$$

$\mathbf{M}(\mathbf{q})$ is the $N \times N$ mass matrix, $\mathbf{C}(\mathbf{q}, \dot{\mathbf{q}})$ is an $N \times 1$ vector of centrifugal and coriolis term, $\mathbf{G}(\mathbf{q})$ is an $N \times 1$ vector of gravity term. q is the generated coordinates. N is the number of generated coordinates, here is 3.

The equation of motion can be written in the following form:

$$\left[\mathbf{M}(3 \times 3)\right] \begin{bmatrix} \ddot{\theta}_1 \\ \ddot{\theta}_2 \\ \ddot{\theta}_3 \end{bmatrix} = \begin{bmatrix} C_1 - D_1\dot{\theta}_1 \\ C_2 - K_2(\theta_2 - \theta_{20}) - D_2\theta_2 \\ C_3 - D_3\theta_3 \end{bmatrix} + \begin{bmatrix} Q_1 \\ Q_2 \\ Q_3 \end{bmatrix} \tag{6.3}$$

The detailed elements in mass matrix are presented in Appendix . Other parameters descriptions are shown in Table 6.1. A Simscape multibody model was also built for the 3 link robot. The graphics is shown in Figure 6.4.

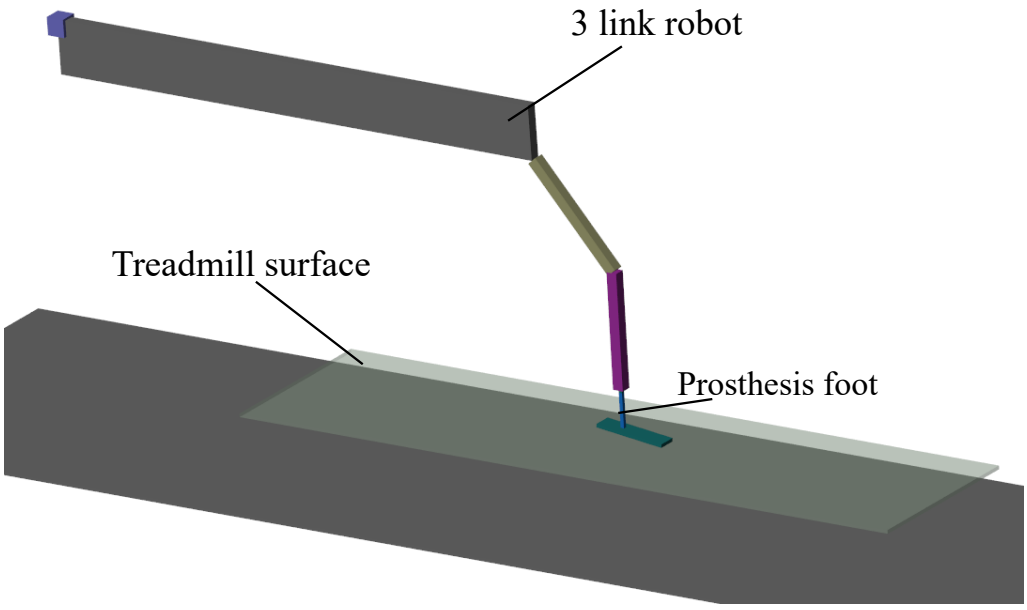

Figure 6.4: The mechanical model in Simscape Multibody.

Since some physical parameters are hard to measure. So unknown 17 physical parameters are identified. Parameter names and their identification results are presented in Table 6.1. A point to notice is that these physical parameters are redundant so that multiple optimal results are possible. For example, the position of

centre of mass can be equally effective of increase or decrease the mass. I use random position demand signals on the test rig and model. The difference between the measured forces on three joints and the forces in the model is minimised. Another group of motion is used to verify the optimisation result. It is shown in Figure 6.5. The relative low frequency range is modelled accurately, the high frequency is not captured well with the model.

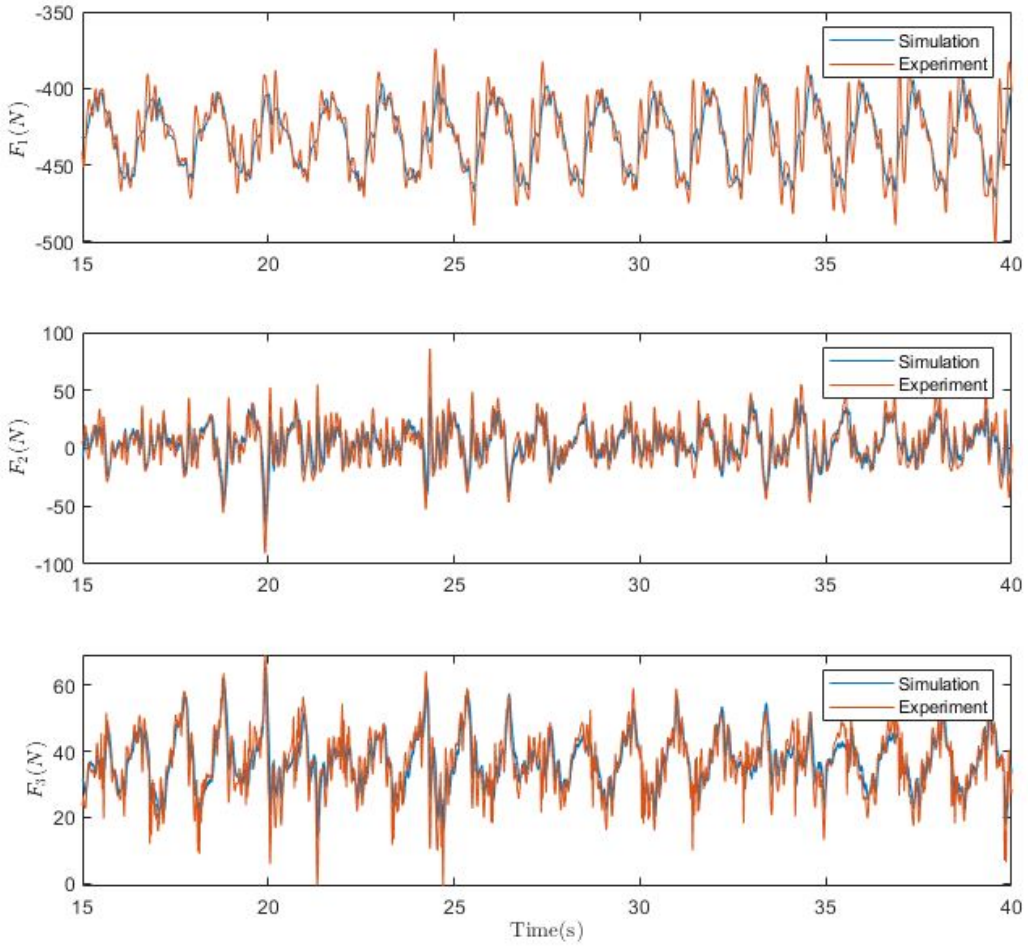

Figure 6.5: Simulated force and measured force on the same trajectory.

Prosthesis Model

In simulation, I modelled a prosthesis. The geometry is based on *Echelon* [114]. It has a main spring on the top of the foot. The simulated prosthesis has passive mode and active mode. For passive mode, the foot only has spring characteristics.

For active mode, the prosthesis has actuation on the top of the spring, see Figure 6.7. It will start to extend at time t_a after a gait cycle is started. The actuator will extend to its maximum position x_{max} with extend rate of b_a. The actuator will retract back to its original length at time t_b.

Table 6.1: System identification result of test rig physical parameters.

	Joint 1 result	
m_1	Link 1 mass	$20.00\,kg$
I_1	Link 1 Moment of Inertia	$26.56\,kg.m^2$
D_1	Joint 1 damping	$110.6\,N.s/rad$
g_{11}	Link 1 CoM location	$0.3352\,m$
g_{12}	Link 1 CoM location	$0.5\,m$
	Joint 2 result	
m_2	Link 2 mass	$1.455\,kg$
I_2	Link 2 Moment of Inertia	$0.0512\,kg.m^2$
D_2	Joint 2 damping	$1.109\,N.s/m$
g_{21}	Link 2 CoM location	$0.5045\,m$
g_{22}	Link 2 CoM location	$0.4501\,m$
K_2	Joint 2 stiffness	$8.2500\,N/rad$
θ_{20}	Joint 2 balanced angle	$0.8116\,rad$
	Joint 3 result	
m_3	Link 3 mass	$0.6594\,kg$
I_3	Link 3 Moment of Inertia	$0.0331\,kg.m^2$
D_3	Joint 3 damping	$0.3419\,N.s/rad$
g_{31}	Link 3 CoM location	$0.3014\,N.s/m$
g_{32}	Link 3 CoM location	$-0.5863\,N.s/m$

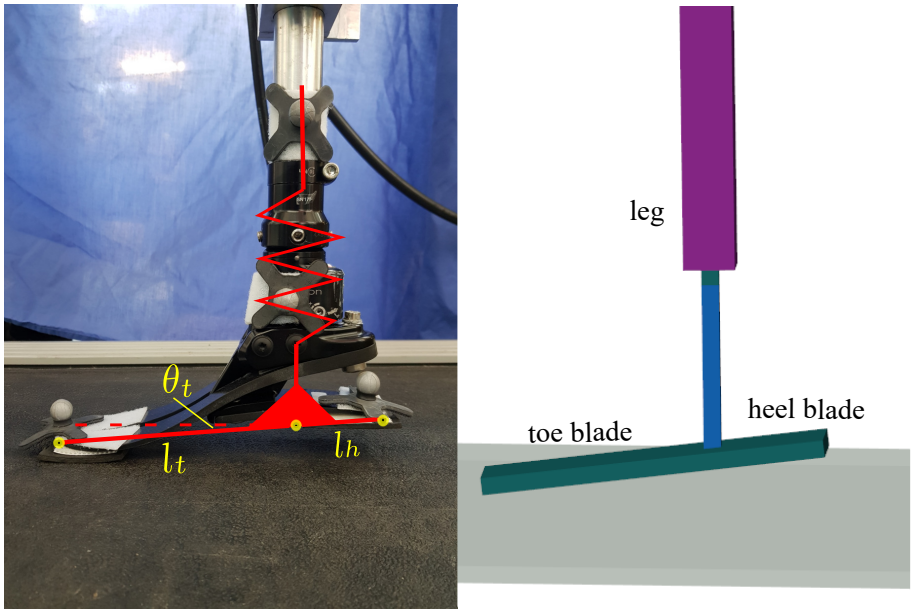

Figure 6.6: Echelon prosthesis foot (left) and prosthesis foot model in Simscape Multibody (right).

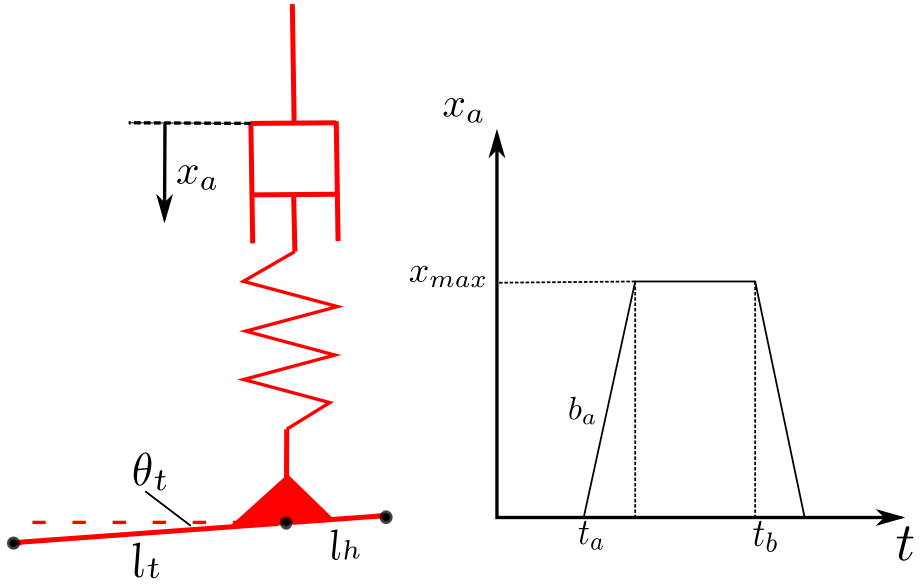

Figure 6.7: Echelon prosthesis foot model with active mode (left). The active push-off plot. (right)

The physical parameters are displayed in Table 6.2. These parameters doesn't need to be accurate. It represents a test prosthesis which parameters are assumed unknown.

Table 6.2: Prosthesis foot model parameters.

	Geometry	
l_t	Toe blade length	$0.1417\,m$
l_h	Heel blade length	$0.07\,m$
θk_{t0}	Toe spring rest angle	$70.65°$
θk_{h0}	Heel spring rest angle	$38.67°$
	Actuation and spring stiffness	
t_a	Extend time	$0.5\,s$
t_b	Retraction time	$1\,s$
x_{max}	Max extended distance	$0.01\,m$
b_a	Extend rate	$0.25\,m/s$
k_t	Foot main stiffness	$10000\,N/m$

Ground contact model

The foot contact model is a mainly based [115]. It is a nonlinear ground contact model. Normal force is calculated from Equation 6.4. z is the vertical displacement of ground deformation. x is the horizontal deformation. K_n, D_n, K_t, D_t are ground properties. The values of the ground properties used in our simulation are described in Table 6.3.

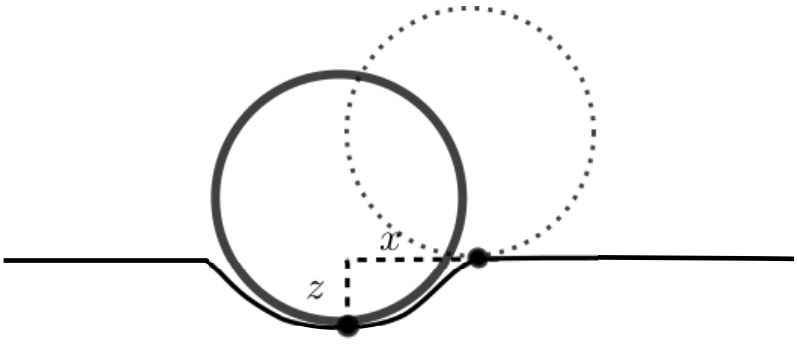

Figure 6.8: Single point contact schematic.

$$F_n(n) = K_n z^{\frac{3}{2}} + D_n z^{\frac{1}{2}} \dot{z} \tag{6.4}$$

Friction force is modelled as a spring and damper. f_{stick} represents the friction force if it lies inside the friction cone in Equation 6.6. The friction cone is defined

by f_{slip}.

$$f_{stick} = K_t x z^{\frac{1}{2}} + D_t \dot{x} z^{\frac{1}{2}} \tag{6.5}$$

$$f_{slip} = \mu f_y(n) \frac{f_{stick}(n)}{|f_{stick}(n)|} \tag{6.6}$$

$$F_f(n) = \begin{cases} f_{stick} & |f_{stick}| < |f_{slip}| \\ f_{slip} & |f_{stick}| \geq |f_{slip}| \end{cases} \tag{6.7}$$

In out model, there are three contact points, toe, heel and the middle of the foot. Total ground reaction force F_x and F_y is the sum of contact forces from the toe and the heel. The more the contact points is, the more realistic the simulation is. However, the simulation speed will be slow. In our simulation, I don't need the ground contact model to be accurate.

$$F_x = \sum_{n=1}^{3} F_n(n) \tag{6.8}$$

$$F_y = \sum_{n=1}^{3} F_f(n) \tag{6.9}$$

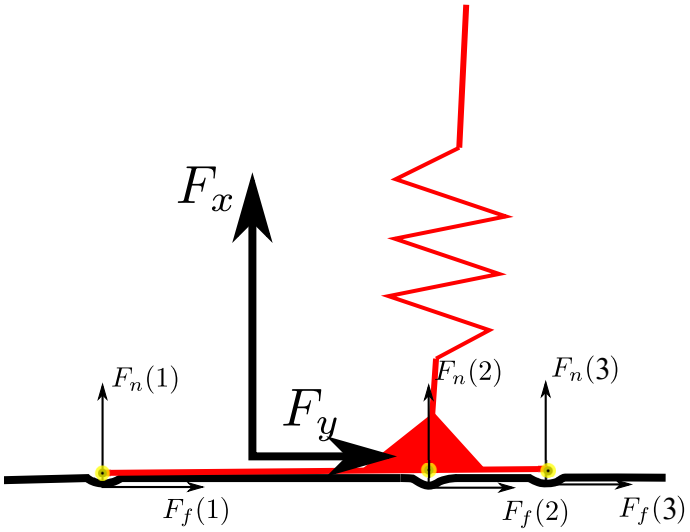

Figure 6.9: Foot contact schematic.

6.3 Hydraulic Model

The model schematic of an actuation system is presented in Figure 6.10. It mainly have three parts: Servo-valve model, actuator model and manifold model. The other two actuators with valve and manifold have the same configuration of model. The model assumes the system has a constant pressure supply and sufficient flow.

Table 6.3: Ground properties for contact model.

Ground properties			
K_n	D_n	K_t	D_t
8.5×10^6	3.1×10^3	12.75×10^6	3.1×10^3

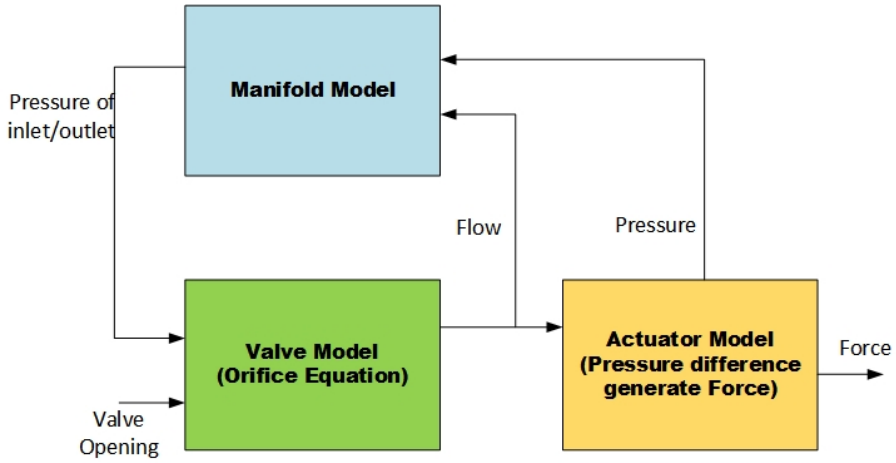

Figure 6.10: Actuator hydraulic system model overview. Cyan block is manifold model. Green block represents valve model. Yellow block represents actuator model.

Servo Valve

The spool dynamics is modelled as a second order transfer function.

$$\ddot{x} + 2\zeta\omega_n\dot{x} + x = K_{val}u \tag{6.10}$$

where x is the valve opening and u is the control signal (normalised from -100 % to +100 %).

The orifices in the valve are modelled mathematically as follows: For $x \geq 0$:

$$Q_1 = K_v x sign(P_s - P_1)\sqrt{P_s - P_1} \tag{6.11}$$
$$Q_2 = K_v x sign(P_s - P_2)\sqrt{P_2 - P_r} \tag{6.12}$$

For $x < 0$:

$$Q_1 = K_v x sign(P_1 - P_r)\sqrt{P_1 - P_r} \tag{6.13}$$
$$Q_2 = K_v x sign(P_s - P_2)\sqrt{P_s - P_2} \tag{6.14}$$

where P_s and P_r are supply pressure and return pressure. Q_1 and Q_2 are flow go through two channels. P_1 and P_2 are pressure of two flows. The valve coefficient is K_v. See Figure 6.11.

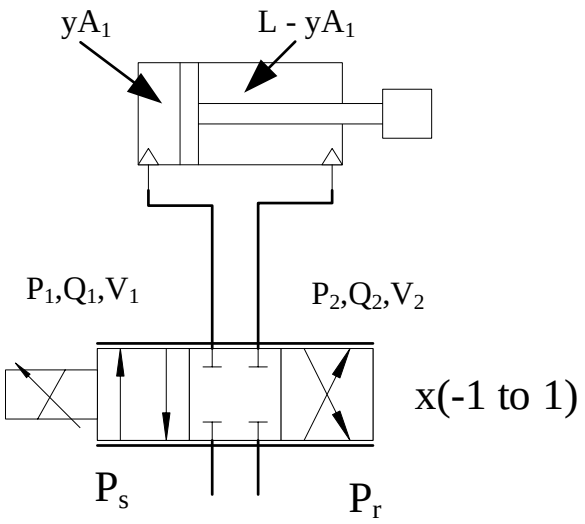

Figure 6.11: Hydraulic circuit for control valve modelling.

Actuator

The actuator is modelled driving the mass M of piston/grips, with the test specimen load considered as an external force F. The model includes fluid compressibility, leakage (across the piston) and the valve orifice equations. Piston force balance:

$$P_1 A_1 - P_2 A_2 - F = M\ddot{y} \tag{6.15}$$

Cylinder flow equations:

$$Q_1 = A_1\dot{y} + \frac{\dot{P}_1(A_1 y + V_1)}{B} + c_l(P_1 - P_2) \tag{6.16}$$

$$Q_2 = A_2\dot{y} - \frac{\dot{P}_2(A_2(L - y) + V_2)}{B} + c_l(P_1 - P_2) \tag{6.17}$$

where B is bulk modulus. c_l is the cross piston leakage coefficient. V_1 and V_2 are hoses volume on both sides of the actuators.

Manifold

The manifold consists of the flow paths in the block. Hydraulic hoses are connected between manifold block and actuator ports. Flow pressure characteristic of the manifold is modelled using orifice equation 6.18. The rated pressure, P_{mr} drop of $50\,L/m$ (Q_{mr})is set to be $70\,bar$.

$$Q_m = Q_r\sqrt{\frac{\Delta P_m}{\Delta P_r}} \tag{6.18}$$

6.4 Controller

The lower layer control of the HGS is a PI controller, which is shown in Figure 6.12. The PI gains are not optimised with ziegler nichols method. It is because in the upper layer controller, an ILC type of controller is used. The performance of a single loop tracking is not as important. On the contrary, a high very good position tracking may force the HGS to push test prosthesis to unachievable position so that the test prosthesis is damaged. Also, with external load from the ground during the stance phase, tracking error with a large integration gain will cause instability when the external load is suddenly released in the swing phase.

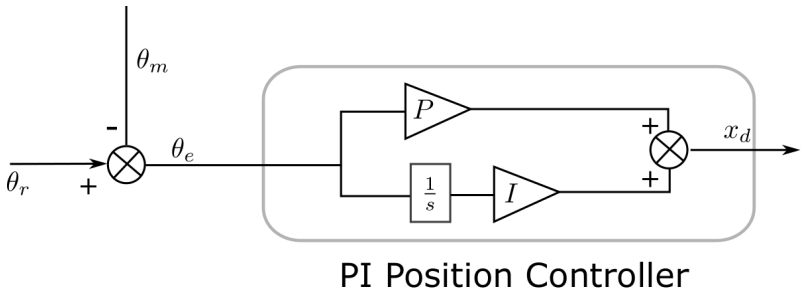

Figure 6.12: PI controller

Three joint controllers gains which are used for EILC experiments in simulation and experiments are shown in Table 6.4.

Table 6.4: PI controller gains

Ground properties			
K_n	Joint 1	Joint 2	Joint 3
P	7	15	20
I	1	7	5

Chapter 7

Model Validations and Simulation results

In this chapter, I first validate the model developed in the last chapter. Two difference mechanical model are verified with each other first. Then chirp signals are used in real test rig and simulation model to validate model accuracy.

In the second section, simulation results are presented to check the effectiveness of the proposed EILC ground reaction force controller. I have simulated 3 groups of test, which is following:

- Stationary ground GRF control with a passive prosthesis.
- Moving ground GRF control with a passive prosthesis.
- Moving ground GRF control with an active prosthesis.

The test results have shown that the proposed EILC on GRF is effective and robust.

7.1 Model validations

In this section, simulations without ground contact are carried out first. For mechanical models, the Lagrangian model and the Simscape (Matlab Multibody package) model are compared against each other to verify the correctness. Chirp signals are used to derive bode diagrams in simulation. The result bode diagrams are compared with experiment result to check simulation fidelity.

Compare models and track human walking kinematics

In the simulated models, the gait simulator robot was tested to swing in the air without the force disturbance. The base actuator is set to be fixed angle. The hip angle and knee angle are from human level walking knee and hip joints data. And the data is converted to hip and knee actuator position signals. Then the converted signals are used as inputs to control the actuators to mimic the same motion. A step period is assumed to be 1.2s. Desired angles and measured angles are showed in Figure 7.1. Lagrangian model result is on the top of Simscape model result. It proves that the Lagrangian model equation was correctly conducted.

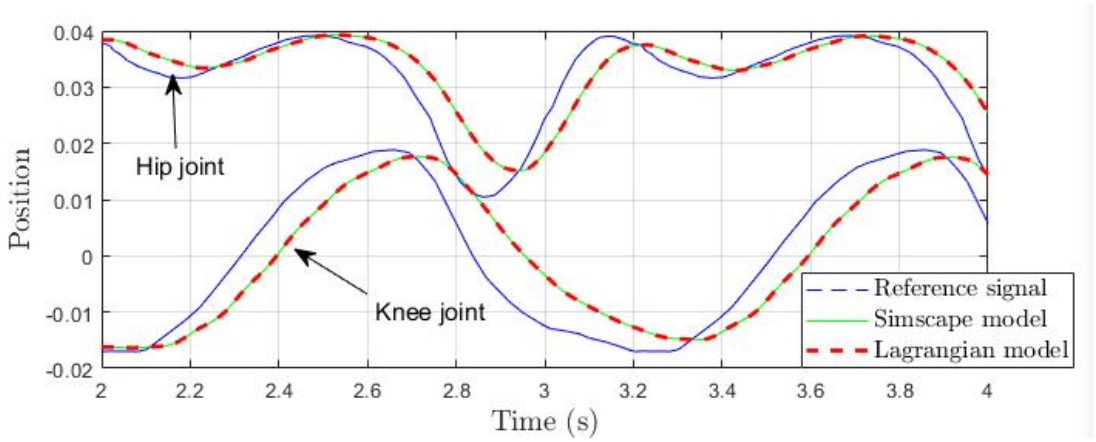

Figure 7.1: Compare Lagrangian and Simscape model via same tracking position demands. Blue line is desired trajectory, green line is Simmechanics model result and red dashed line is Lagrangian model result.

Also, the total flow rate is shown in Figure 7.2. The largest flow rate is just below $2\,L/min$. The flow rate plot gives guidance of choosing hydraulic powerpack.

Model Verification with Chirp Signal

Chirp signal is used to validate the simulated model with experimental test rig. The chirp signal start with $0.01\,Hz$ to $2.5\,Hz$. Each joint is tested with the chirp reference signal while the other two joints hold their positions. Simple proportional controller is used. The gains of three controller are shown in Table 7.1. With the same controller, the position tracking results are compared in Figure 7.3 to 7.8.

First, for the hip and knee joint simulation result and experiment are reasonable close. The knee joint has the closest bode diagram with experiment data under

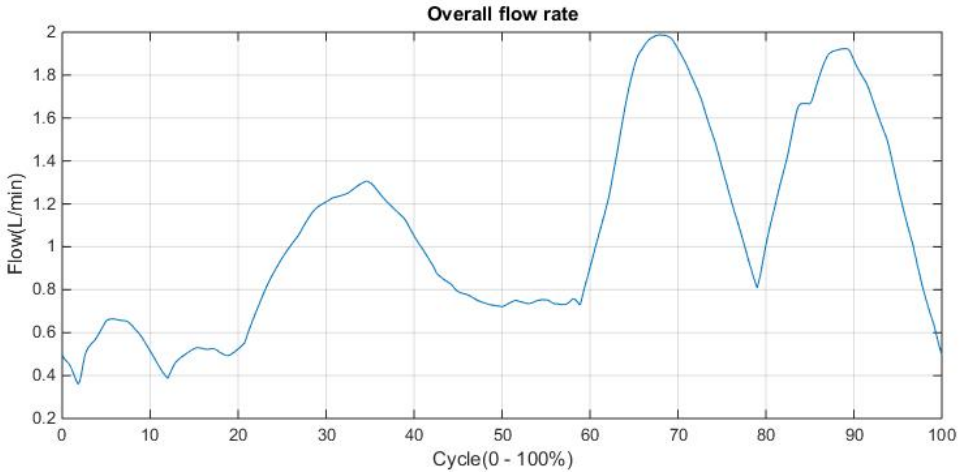

Figure 7.2: The flow rate of hydraulic system in swing test.

Table 7.1: Setting of joint position controller

Proportional gains		
Base joint P_1	Hip joint P_2	Knee joint P_3
7	15	10

2.5 Hz. The maximum amplitude ratio difference is 0.5 dB and phase lag difference is 5 ° in Figure 7.8. The hip joint has slightly larger difference, the maximum amplitude ratio difference is 1.5 dB and phase lag difference 10 ° in Figure 7.6. The difference is mainly caused by joint stiffness inaccuracy introduced by the hydraulic hose which is hard to capture in the simulation properties, because the stiffness will vary at different robot motion angle and speed. Having lighter hoses will help to improve the results. It proves the simulation model is able to represent the experiment system for these two joints roughly. Since the iterative learning control is used, the model doesn't need to be perfectly accurate. For the base joint, the experiment data doesn't match the simulation result. In experiment data, there is a obvious resonance frequency at around 2.3 Hz. It comes from the flexibility of the long beam. The simulation model doesn't include the mechanical stiffness of the beam, so that it is not able to represent test rig vibration on the beam However, the beam is not included in the EILC. The force control is applied only with the hip and the knee joints. The beam is providing vertical motion of the hip, it doesn't need to be fully accurate.

7.2 EILC simulation results

In Chapter 4, in order to test prosthesis, I proposed an extended iterative learning control on ground reaction force control. To demonstrate effectiveness of the proposed controller, the test rig model with ground contact simulation results are presented. The model includes the ground contact model. It requires very small

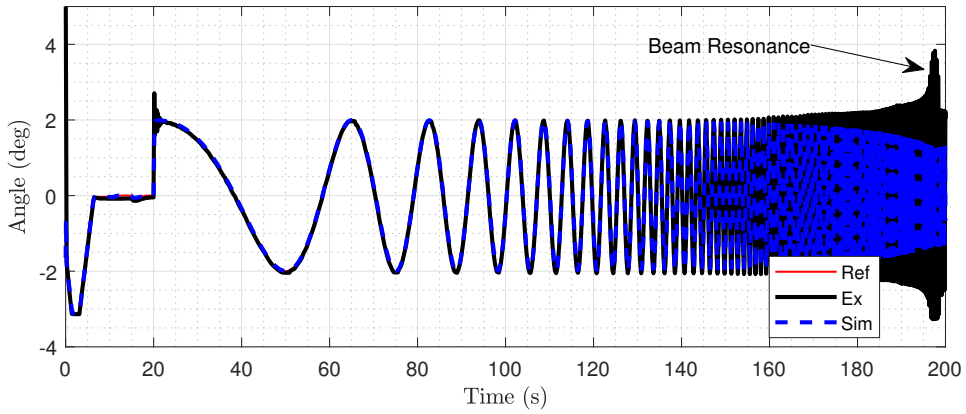

Figure 7.3: Base joint chirp signal position tracking.

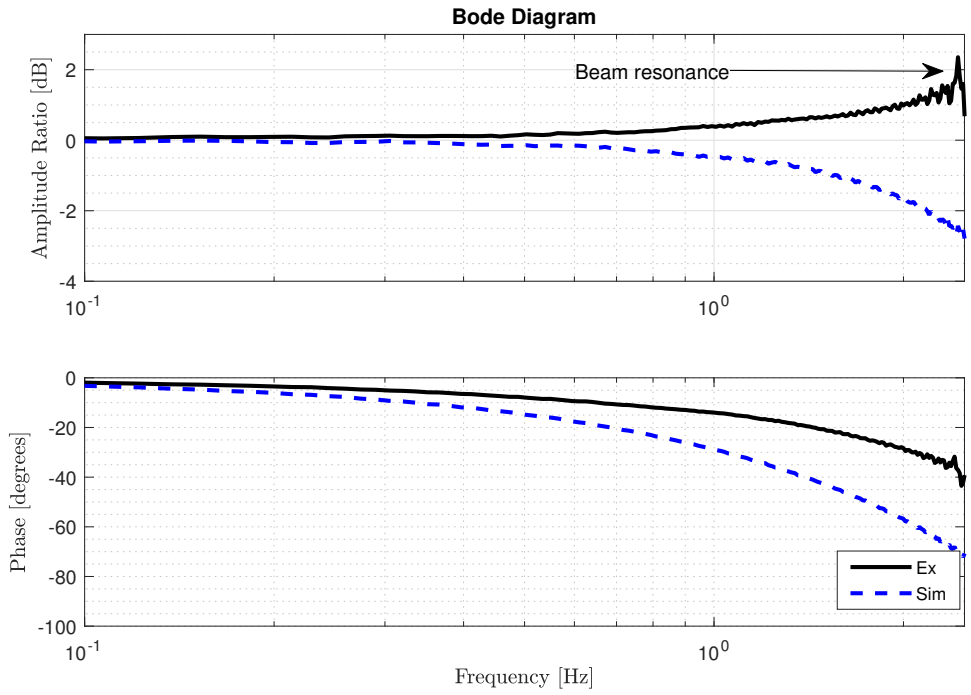

Figure 7.4: Base joint bode diagram.

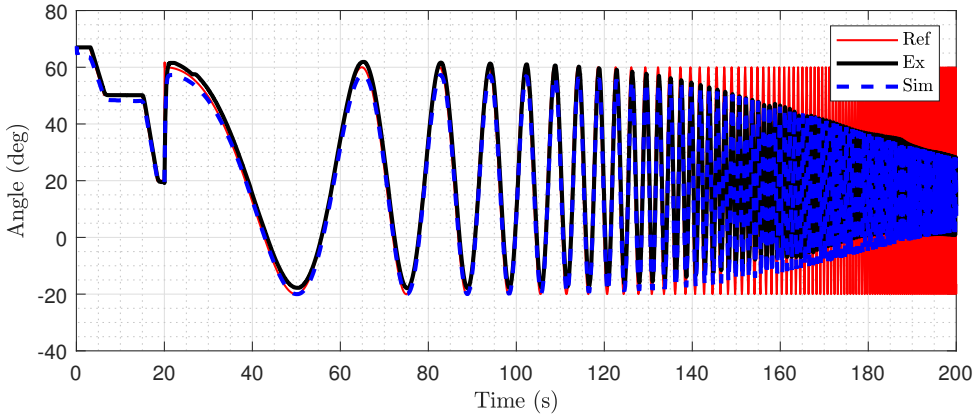

Figure 7.5: Hip joint chirp signal position tracking.

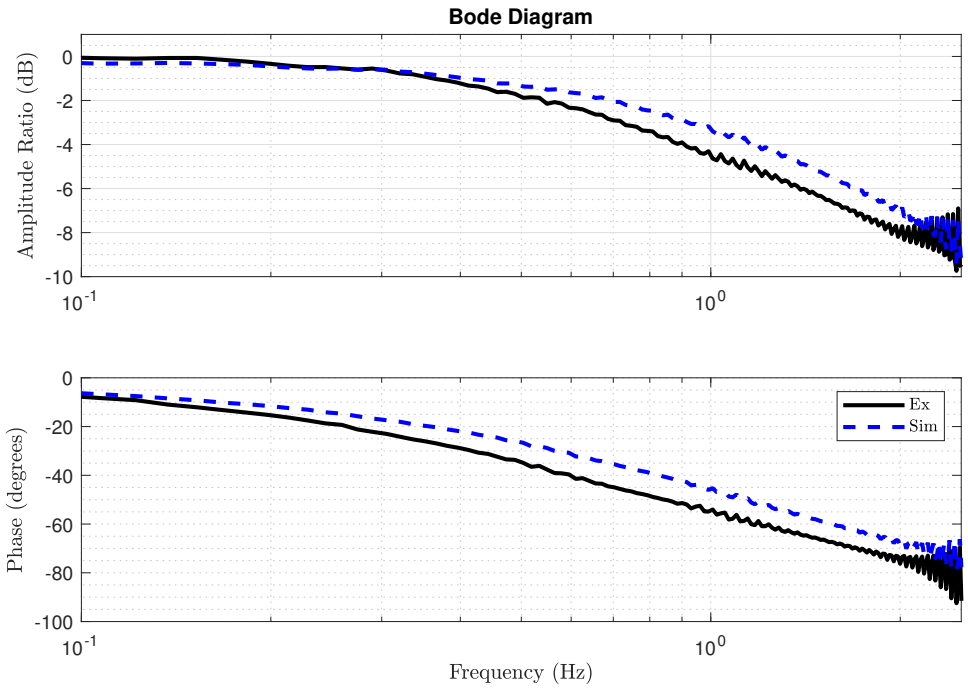

Figure 7.6: Hip joint bode diagram.

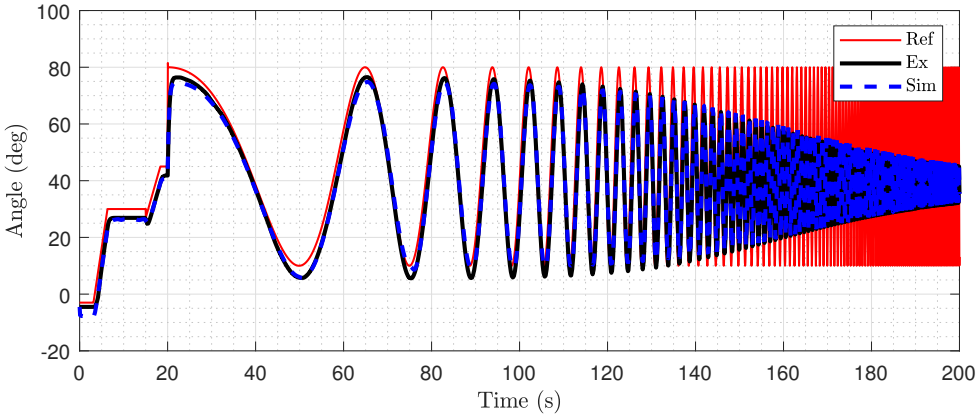

Figure 7.7: Knee joint chirp signal position tracking.

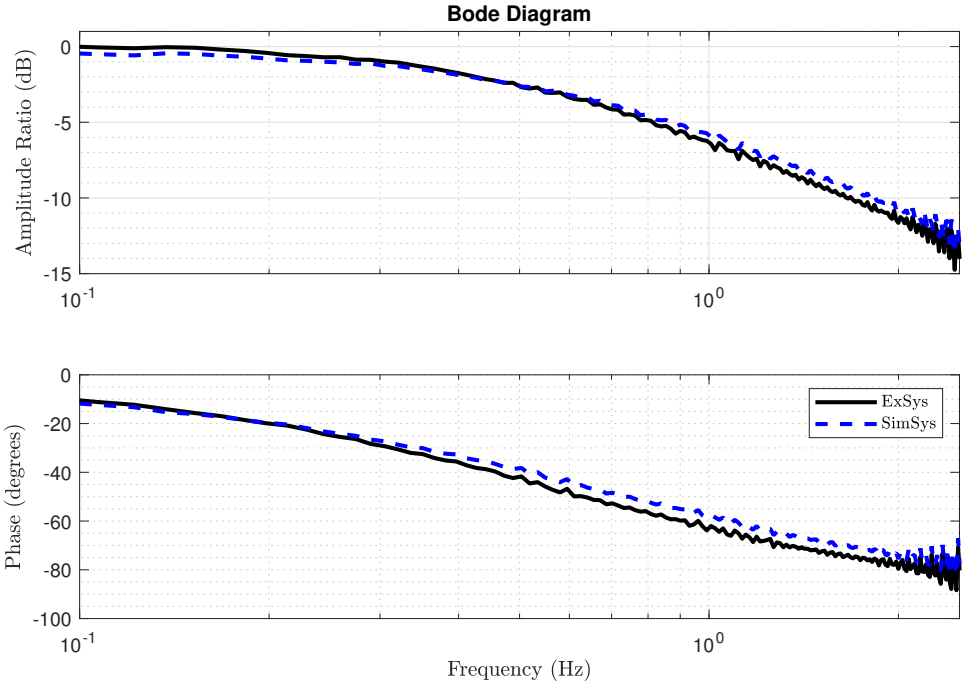

Figure 7.8: Knee joint bode diagram.

time step due to the high stiffness of the ground. To speed up the simulation and keep the simulation stable. A simplified model without hydraulic system is used. The actuation system uses first order transfer function to represent the real system. The solver used in the simulation is *ode*45 with relative error of 10^{-6}.

7.2.1 Stationary Ground Reaction Force Control

The stationary ground contact is simulated. The first iterative trajectory of the rig is the foot pushing down against the ground, referring to Figure 7.9. The desired horizontal and vertical forces come from Opensim model.

To set up a comparison, one dimensional force control experiments was carried out on the vertical force control (F_y). Joint 3 was controlled with a simple PD type of ILC. The proportional gain P is set to be 5×10^{-5}, the derivative gain D is set to be 1×10^{-4}.

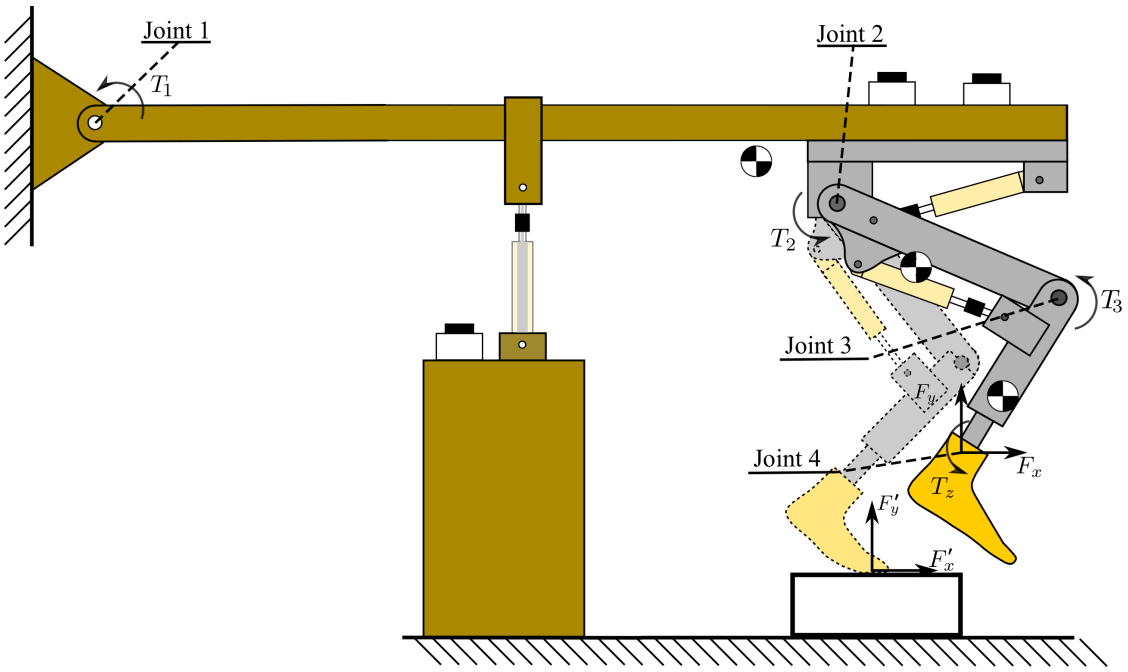

Figure 7.9: Simulated motion of the test rig.

From the simulation result in Figure 7.10, one can see that the final F_y becomes identical to the target force. For the horizontal force F_x. It is not converging to the required force. From the error RMS plot in Figure 7.11, the error RMS of F_x in one dimension force control remains around $50\,N$. The error RMS of F_y decreases consistently to almost zero.

Two dimensional force experiment was then carried out on horizontal and vertical force control (F_x and F_y) via controlling joint 2 and joint 3. The detailed gain are displayed in Table 7.2.

In the two dimension force simulation result, one can see that the shape of F_x and F_y are similar to the reference forces. The RMS error of both horizontal and vertical forces are decreased to around $20\,N$ within 3 cycles. Comparing two sets of

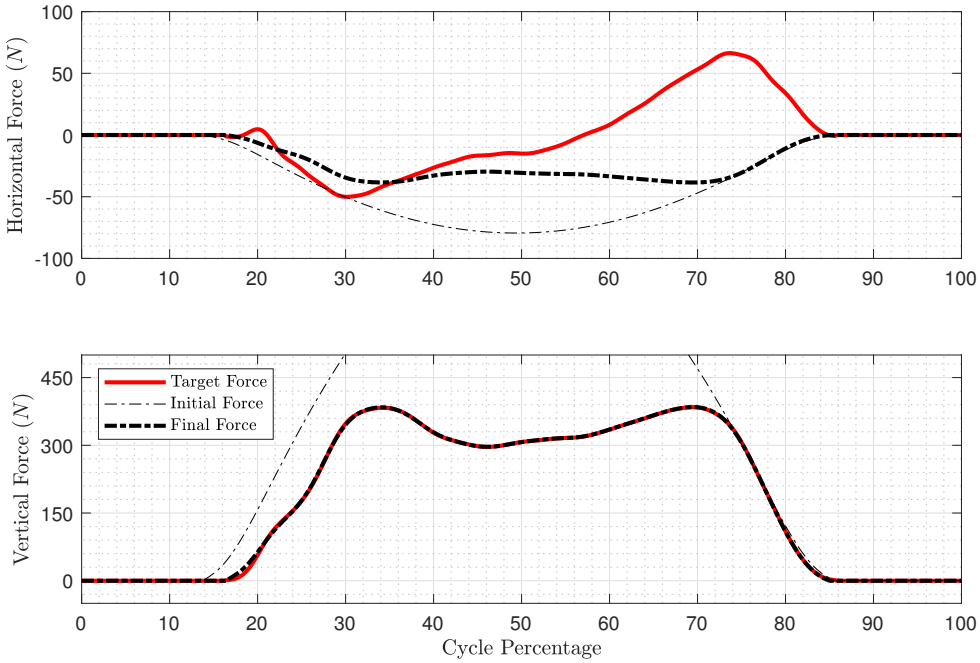

Figure 7.10: Simulated GRF of stationary GRF control. Only vertical force is controlled via joint 3.

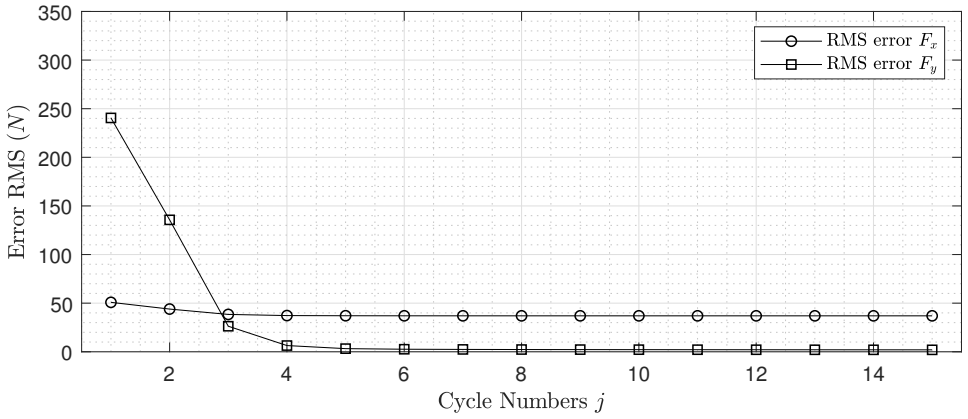

Figure 7.11: RMS error of stationary GRF control (Only vertical force control).

Gains of the EILC			
P_x	D_x	P_y	D_y
1×10^{-4}	1×10^{-4}	5×10^{-5}	1×10^{-4}

Table 7.2: The settings of EILC gains for stationary ground test.

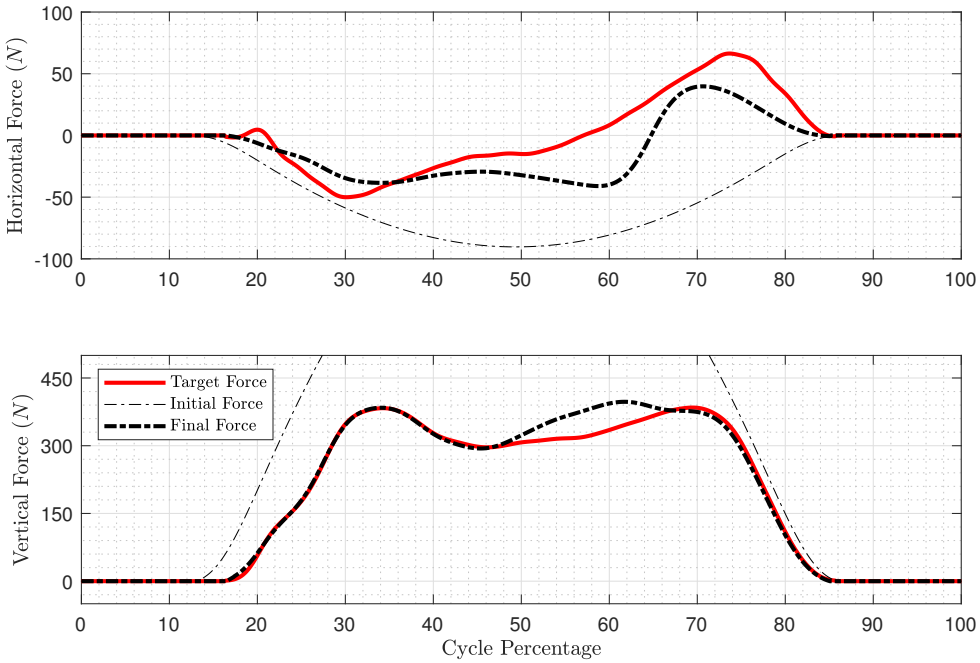

Figure 7.12: Simulated GRF in stationary GRF control (EILC active).

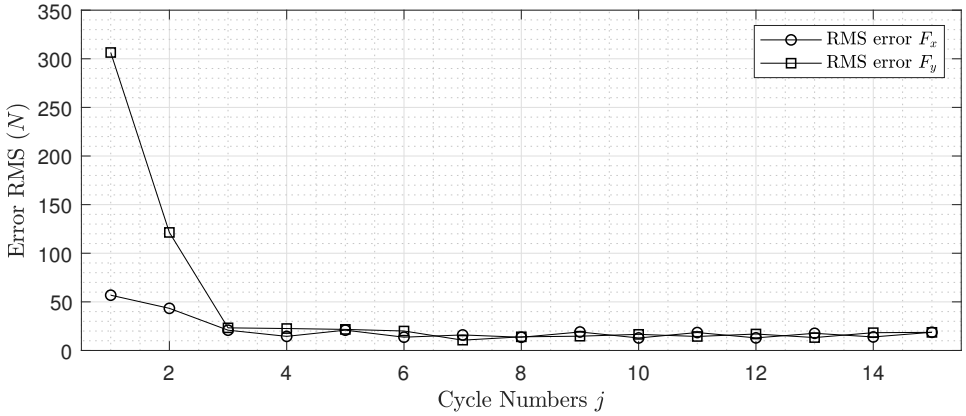

Figure 7.13: RMS error of stationary GRF control (EILC active).

simulation, one can see that the EILC is taking effect and the error of both forces are decreased on a stationary ground.

7.2.2 Moving Ground Reaction Force Control

To demonstrate the proposed ground reaction force control on a moving ground, two sets of simulation are carried out. Two dimension ground reaction force control EILC are used. In the first simulation, the horizontal error $\hat{e_{xj}}$ in is set to zero and $\delta\hat{u_{\theta 2j}}$ in Equation 4.14 is set to zero as well. So, only the command of joint 3 is updated.

$$\hat{e_{xj}} = \hat{F_{xtj}} - \hat{F_{xmj}} = \hat{0} \tag{7.1}$$

The detailed simulation parameters are displayed in Table 7.3. The horizontal gains are set to be zero. Only the vertical forces are effective. The reason the simple 1D ILC on a single joint cannot be used is that from the Jacobian matrix in Equation 4.12. The elements will change signs so that it won't work.

Gains of the EILC			
P_x	D_x	P_y	D_y
0	0	5×10^{-5}	1×10^{-4}

Table 7.3: The settings of EILC gains for moving ground vertical force control.

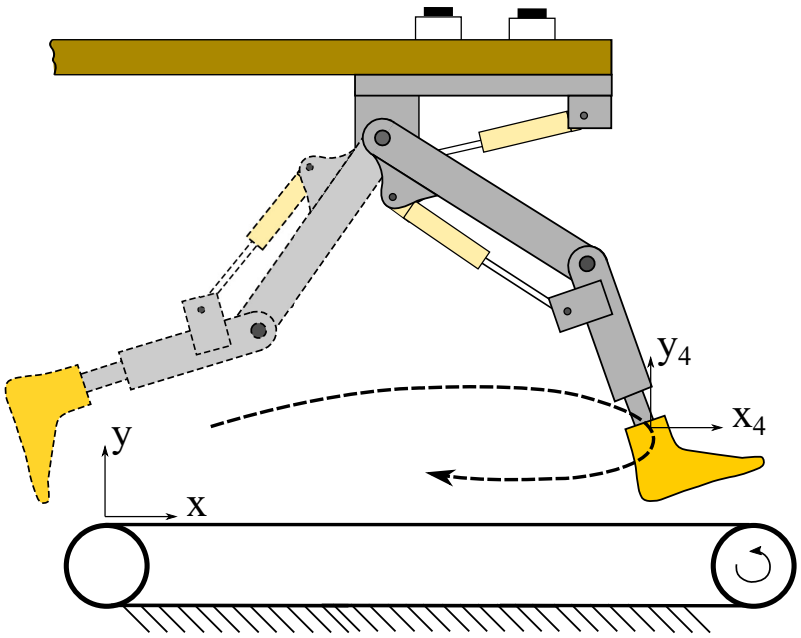

Figure 7.14: Simulated motion of the test rig running on a treadmill.

From the simulation result in Figure 7.18, one can see that the horizontal force F_x doesn't converge to reference force profile. The vertical force F_y converge to the

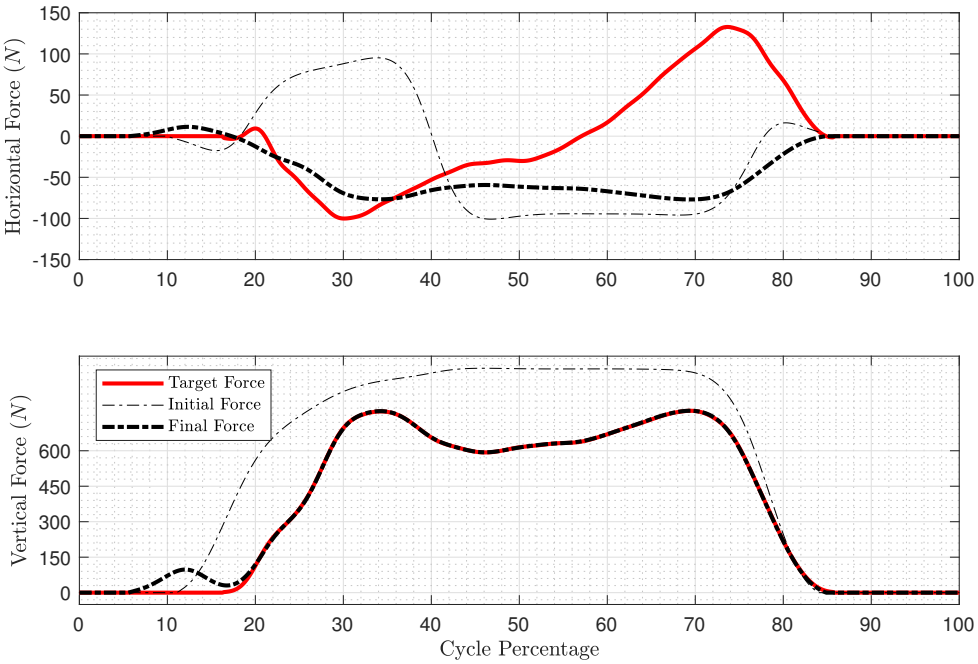

Figure 7.15: Simulated GRF of moving ground test when horizontal force is not controlled. Only vertical force is controlled via joint 3.

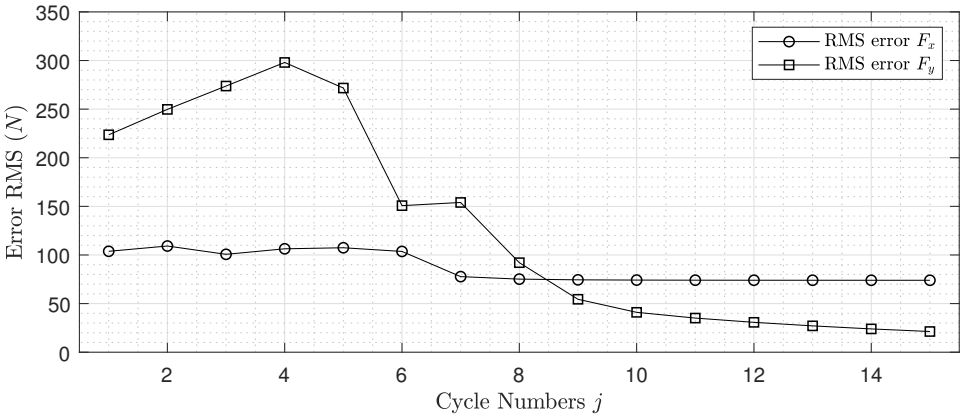

Figure 7.16: RMS error of GRF in moving ground GRF control (Only vertical force control).

reference force profile. There is a small force spike at 10 % in the vertical force plot. It is because the foot accidentally touch the ground. From the error RMS plot 7.16, the F_x error stays 90 N after 7 cycles. The F_y error goes down to below 20 N in the end despite an early increase before 4 cycles.

In the second simulation, the two dimension force control is implemented via joint 2 and joint 3. The detailed gains used for the EILC are the same with the stationary test in Table 7.2.

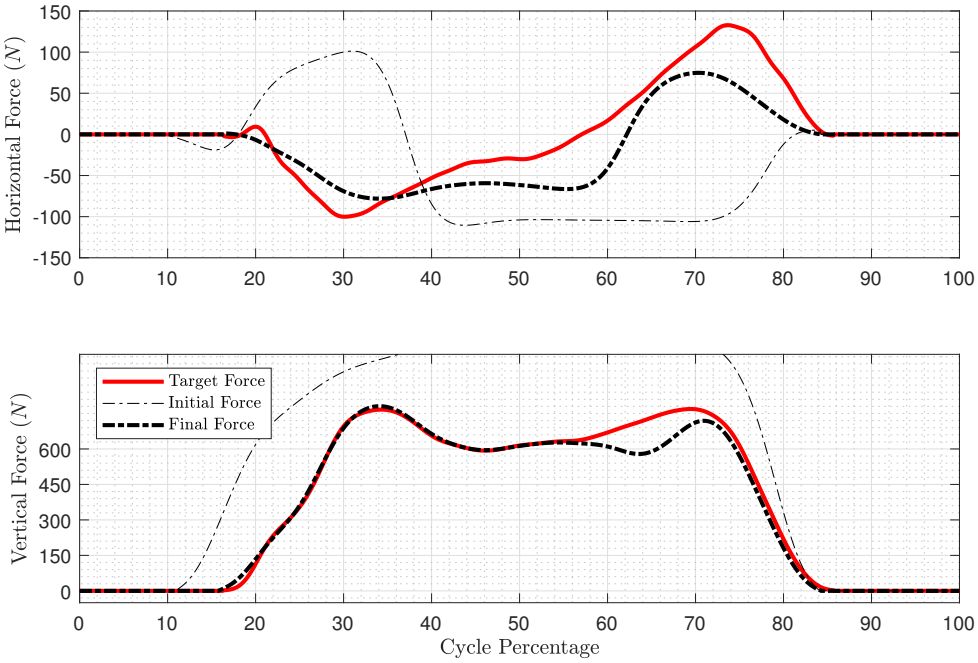

Figure 7.17: Simulated GRF of moving ground test (EILC active).

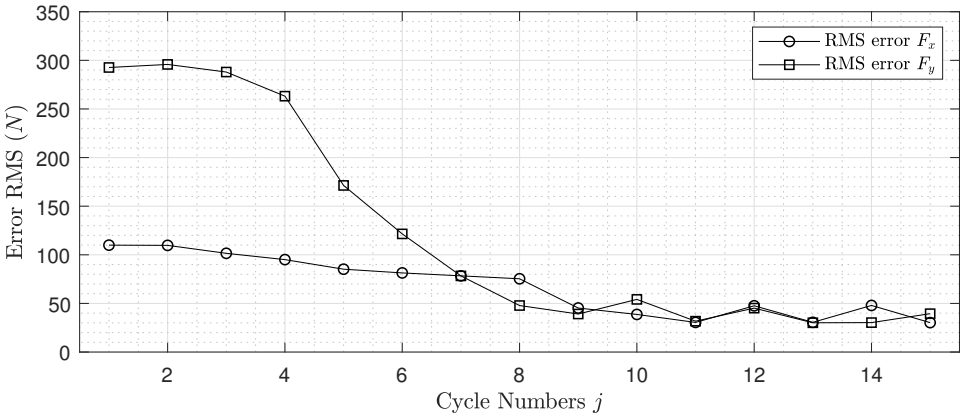

Figure 7.18: RMS error of GRF in moving ground GRF control (EILC active).

From the simulation result, one can see that the shape of both measured forces

are similar to the reference forces. From the error RMS plot, both error of F_x and F_y are decreased to around $50\,N$.

7.2.3 Active prosthesis testing

The EILC performance when an active prosthesis is used is simulated. The detailed active prosthesis model is presented in Section 6.2. The gains used for the EILC are the same with the stationary test in Table 7.2.

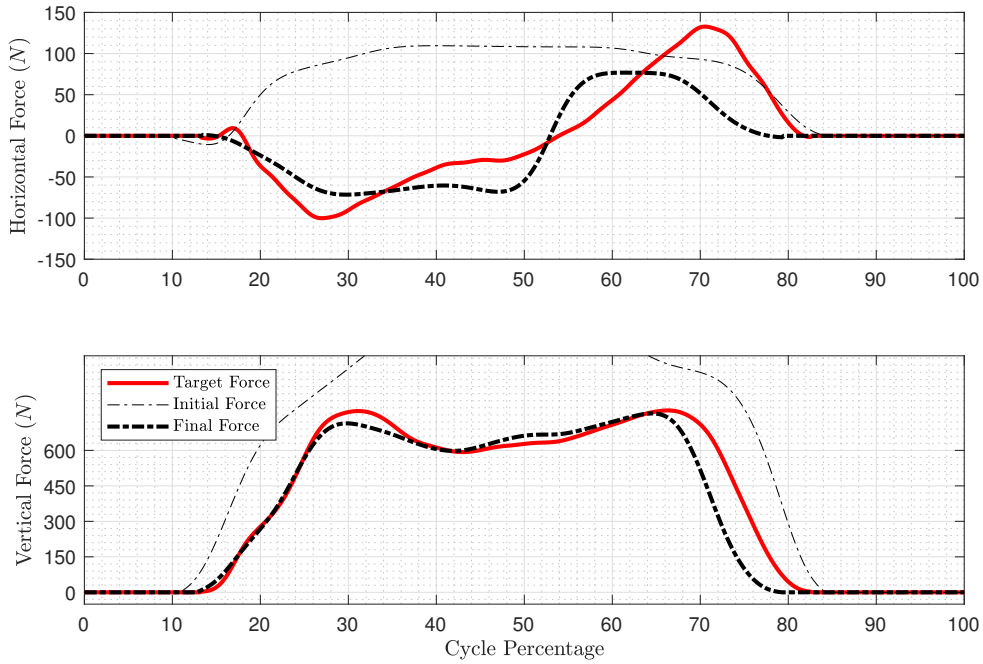

Figure 7.19: Simulated GRF of moving ground test with active prosthesis (EILC active).

In Figure 7.19, the horizontal force has changed closer to the target force shape The horizontal force error decreases from around $100\,N$ to $30N$ in 10 cycles. The vertical force error decreases to $70\,N$ from $30\,N$ in 10 cycles.

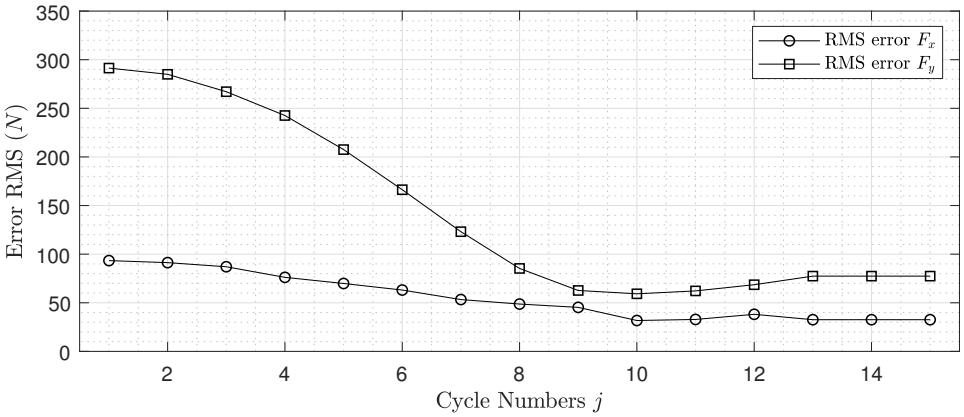

Figure 7.20: RMS error of GRF in moving ground GRF control with active prosthesis (EILC active).

Chapter 8

Experiment Results

In this chapter, experimental results are presented and discussed. In the first section, Extended Iterative Learning Control (EILC) on Ground Reaction Force (GRF) is validated. Four sets of experiment results are presented:

- Stationary ground vertical force control result with a passive prosthesis.
- Stationary ground 2D force control result with a passive prosthesis.
- Moving ground 2D force control result with a passive prosthesis.
- Moving ground 2D force control result with an active prosthesis.

In the second section, testing a passive prosthesis *Echelon* from Blatchford is demonstrated. The result of the test is discussed. Two sets of experiment results are presented:

- Different damping settings
- Different foot Initial Ankle Angle (IAA)

8.1 EILC Results

8.1.1 Stationary Ground Reaction Force Control

The stationary GRF control test is carried out with a 6 axis ATI force sensor. The first iterative trajectory of the rig is the foot (end effector) pushing down against the force sensor, referring to Figure 8.1. The desired horizontal and vertical forces come from Opensim skeleton model and they are scaled down to 50% of the original forces. To set up a comparison, two sets of experiments were carried out. The first test was on the vertical force control (F_y) only. Joint 2 is controlled with a simple integration type of ILC. The proportional gain P is set to be 5×10^{-5}.

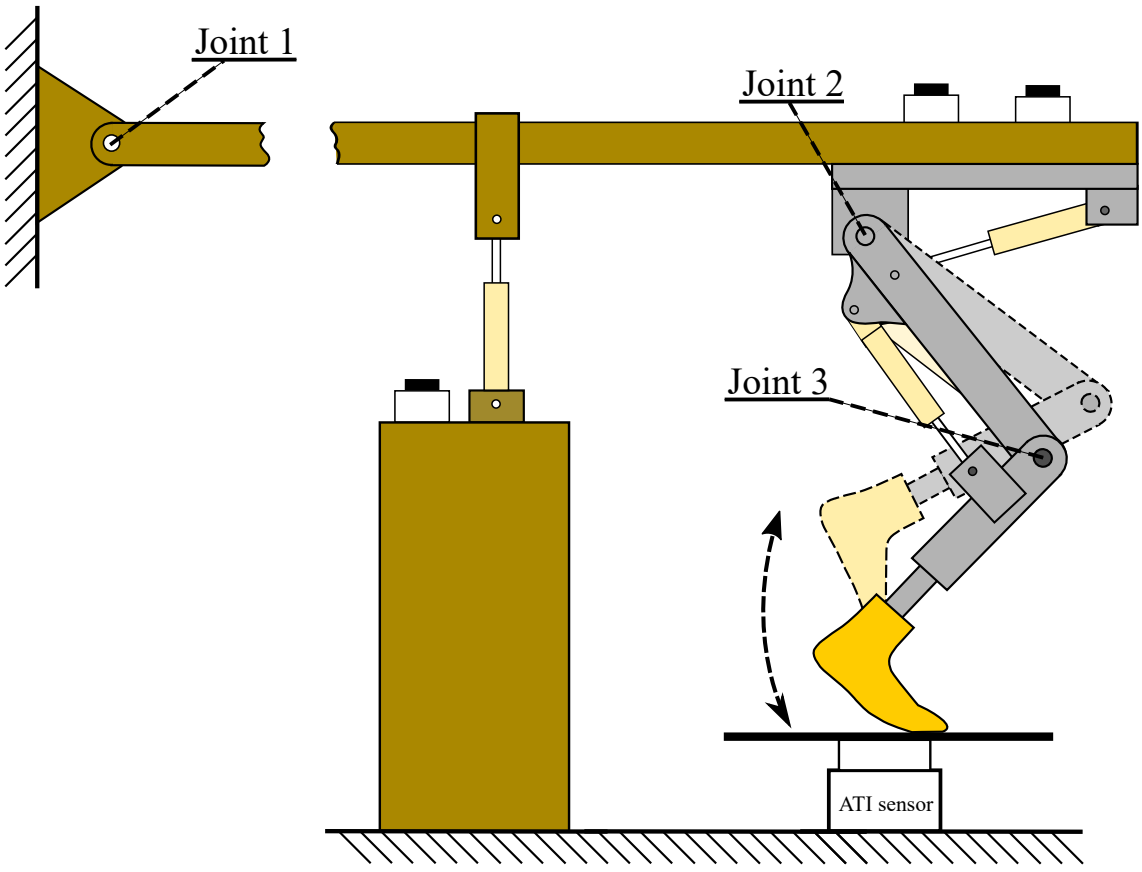

Figure 8.1: The HGS push down against the 6 axis force sensor.

From the experiment result in Figure 8.2 and 8.3, one can see that the final F_y becomes identical to the target force but the F_x doesn't. F_y converges in about 7 cycles. However, the horizontal force diverges. The grey area on the curve is the measured result with 1 standard deviation. It shows that the test rig results are more consistent than human test.

Two dimensional force experiment is then carried out on horizontal and vertical force control (F_x and F_y) via controlling joint 2 and joint 3. The gains of the EILC are set in the same with simulation gains in Table 7.2.

In Figure 8.4, the difference between the final force and the target force in both

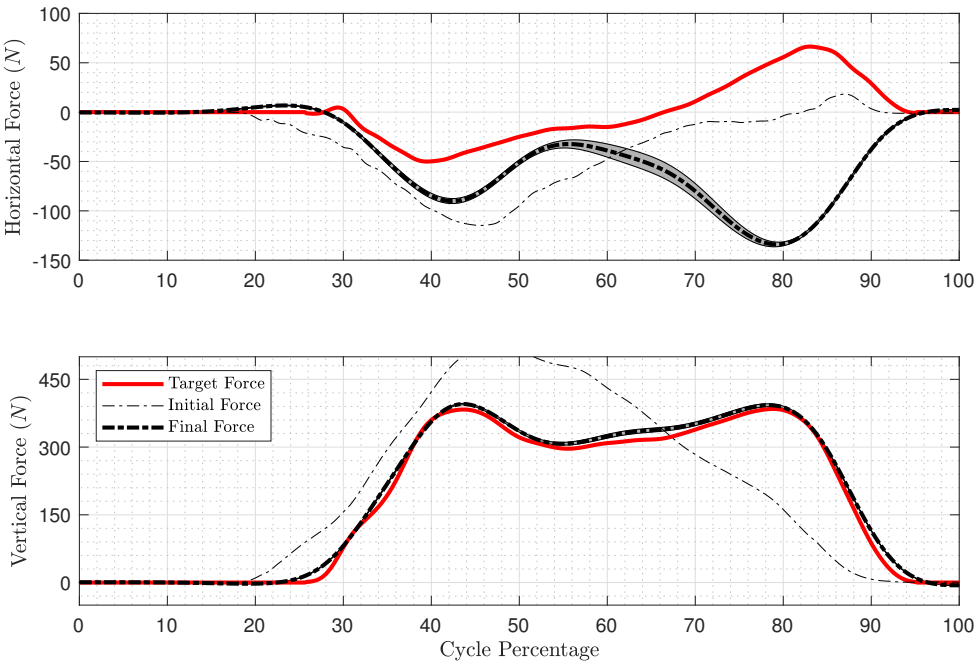

Figure 8.2: Stationary GRF control result (Only vertical force is controlled).

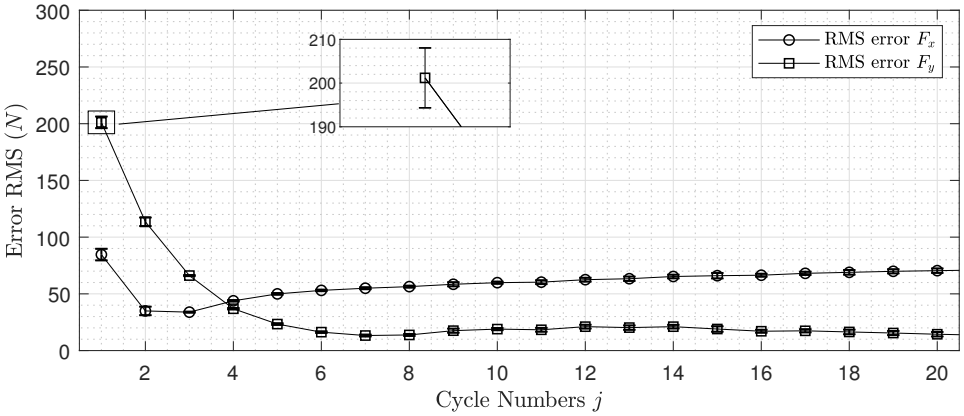

Figure 8.3: Stationary GRF control RMS error plot (Only vertical force is controlled).

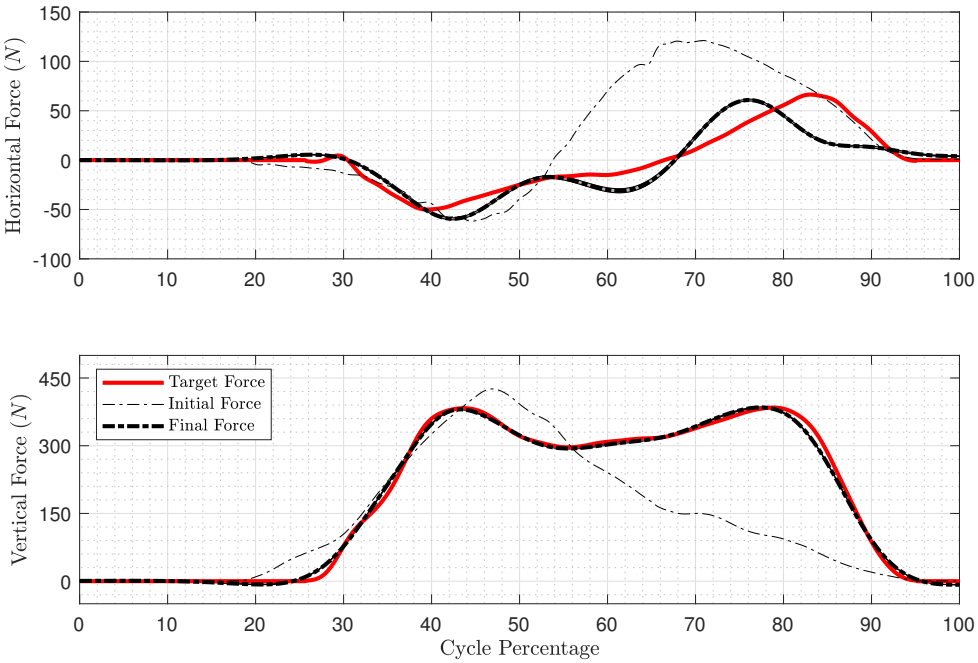

Figure 8.4: Stationary GRF control result (EILC active).

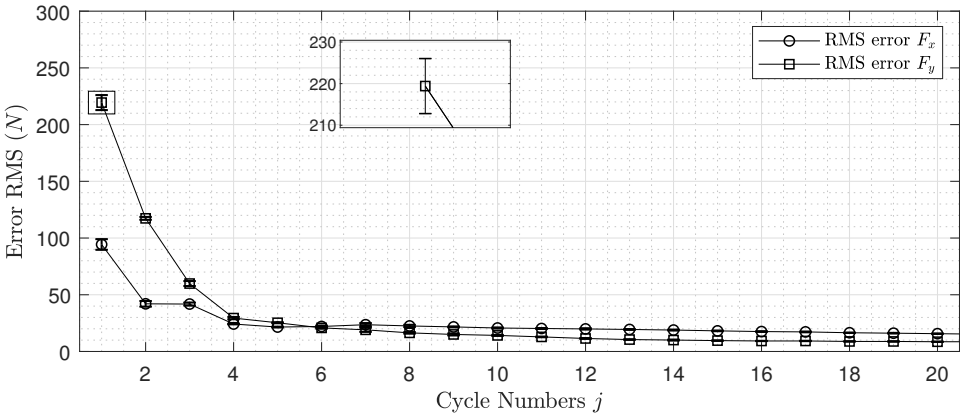

Figure 8.5: Stationary GRF control RMS error plot (EILC active).

F_x and F_y are deceased to around 20 N. In Figure 8.5, both F_x and F_y converges in about 5 cycles.

8.1.2 Moving Ground Reaction Force Control

The proposed EILC GRF control on a moving surface is demonstrated. Experiment is carried out on a treadmill. Since the forces generated are related to the relative motion between the foot and the ground, on a moving surface, the HGS adapts foot horizontal moving speed to the treadmill speed. The gains of the EILC are the same with Table 7.2. In Figure 8.6, it shows a similar force reduction in 2D stationary ground test. In Figure 8.7, despite a slight early increase of RMS in F_x, two directional force RMS decreases overall and are reduced to roughly 50 N after 6 cycles. It is further reduced to around 25 N after 15 cycles.

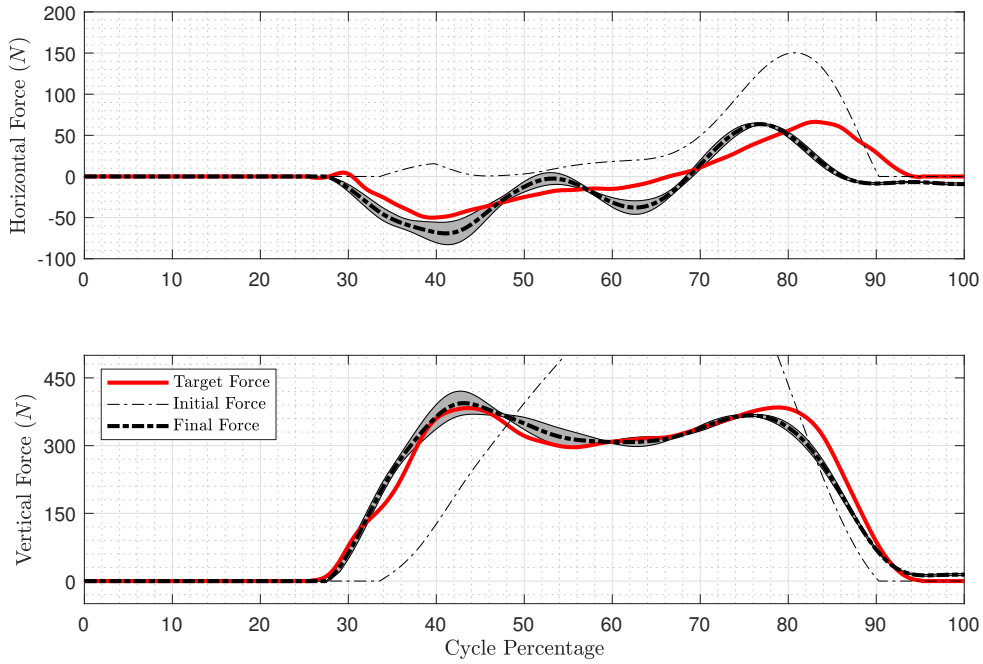

Figure 8.6: Treadmill GRF control result (EILC active).

8.1.3 Moving Ground Reaction Force Control with active prosthesis

The proposed EILC GRF control on a moving surface with an active prosthesis is demonstrated. The active device is able to provide a plantar push-off through a hydraulic circuit. The push-off timing is calculated with a constant delay respect to the average cycle time. The push-off timing of this demonstration is set to be 0.27 s after the leg has reached the front position.

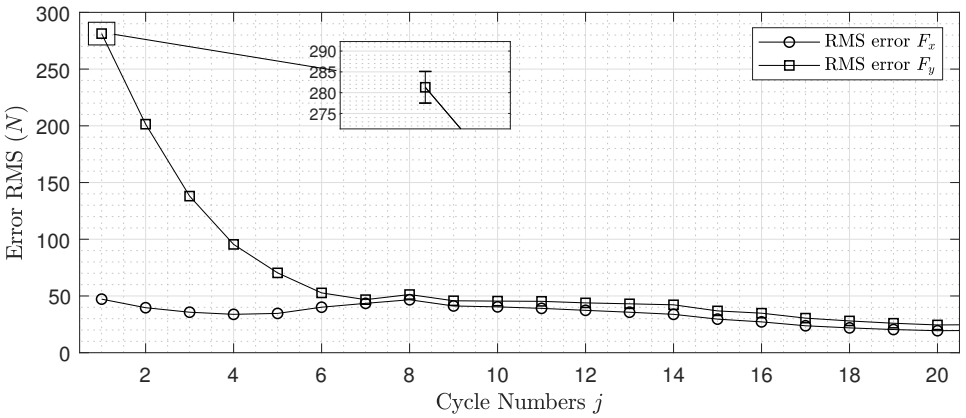

Figure 8.7: Treadmill GRF control result force error RMS (EILC active).

The horizontal and vertical forces converges in 6 cycles. However, compare to the passive mode. The final forces in Figure 8.8 shows higher std, it is because of the active device causes larger vibrations of the rig. The learning process is not monotonic for F_x.

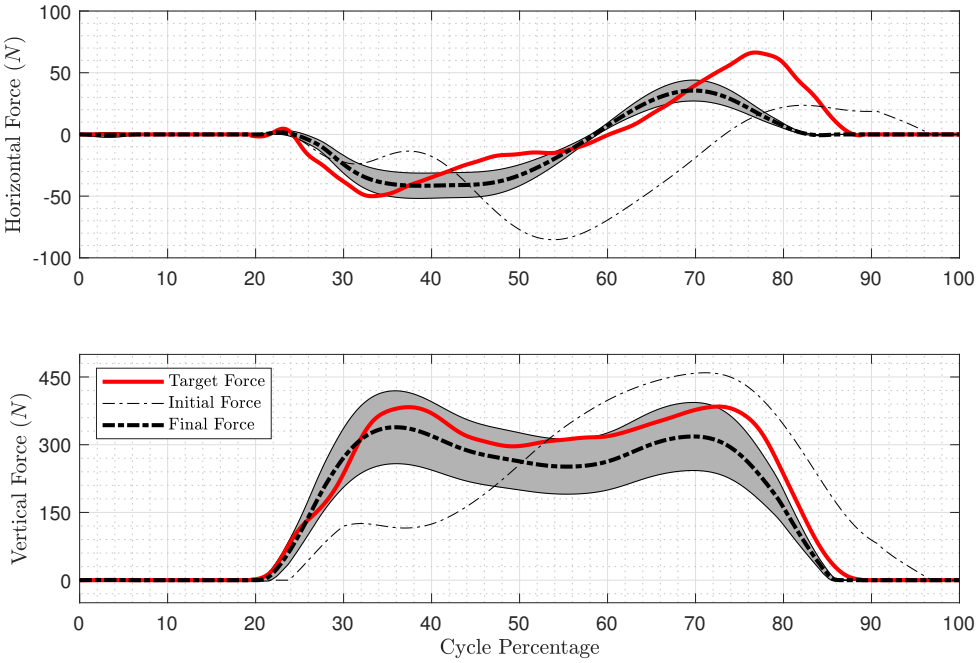

Figure 8.8: Treadmill GRF control result with active prosthesis (EILC active).

Overall, these results proves that with the proposed control method EILC, the HGS is able to simulate a desired force profile on a treadmill. Also, the EILC works both for passive and active prosthesis. This gives the foundation of performing a Inverse Dynamic Approach (IDA) type of prosthesis testing.

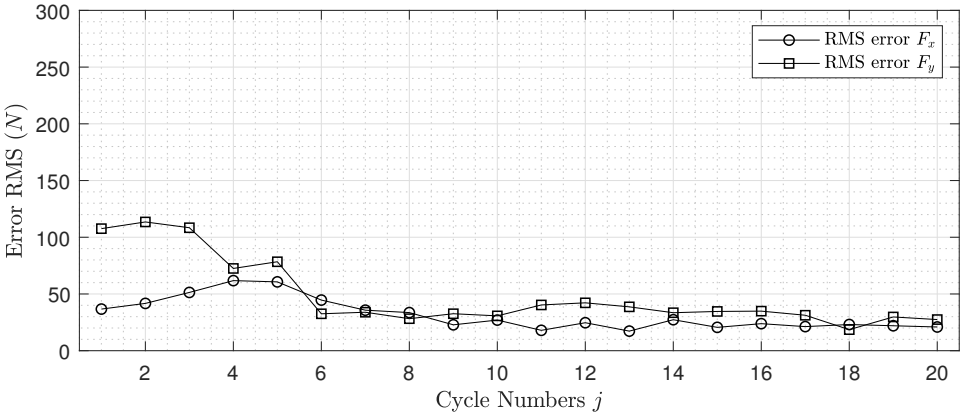

Figure 8.9: Treadmill GRF control result force error RMS with active prosthesis (EILC active).

8.2 Passive Ankle Prosthesis Testing

8.2.1 Define Stance Phase Subsections of Prostheses

To analyse the gait of a tested prosthesis, it is important to define biomechanical key point of a gait. Based on the moving direction of the ankle, the motion of ankle movement are called dorsiflexion and plantarflexion, which dorsiflexsion means the toe moves close to the shank and plantarflexsion refers to the other direction. The stance phase can be divided into three subsections: Controlled Plantarflexsion (CP), Controlled Dorsiflexion (CD) and Powered Plantarflexion (PP). These three subsections of a natural gait are described as below:

- Controlled Plantarflexion (CP): This subsection starts from heel touch down on the ground, and ends at ankle reaches the maximum plantarflexsion position. In this phase, the body is slowed down and stabilized.
- Controlled Dorsiflexion(CD): This subsection starts at the maximum plantarflexsion and ends at maximum dorsiflexsion. The shank rotates around the ankle joint during this phase.
- Powered Plantarflexion(PP): This subsection starts after the maximum plantarflexion is reached. The ankle starts plantarflexion and propels the body.

As shown in Figure 8.10: Five timing points are shown: 1 - Heel Strike, 2 - Foot Flat, 3 - Heel Off, 4 - Fully Loaded ,5 - Toe Off. In the conventional definition of a human gait [20], there isn't a 4 - Fully Loaded point. The relationships between these timing and stance phase subsections are: 1-2 is CP, 2-4 is CD and 4-5 represents PP.

8.2.2 Passive Prosthesis - Echelon

To give a demonstration of performing a test, I examined a commercial passive prosthesis *Echelon*. *Echolon* is developed by Blatchford ltd [114]. It has two pieces

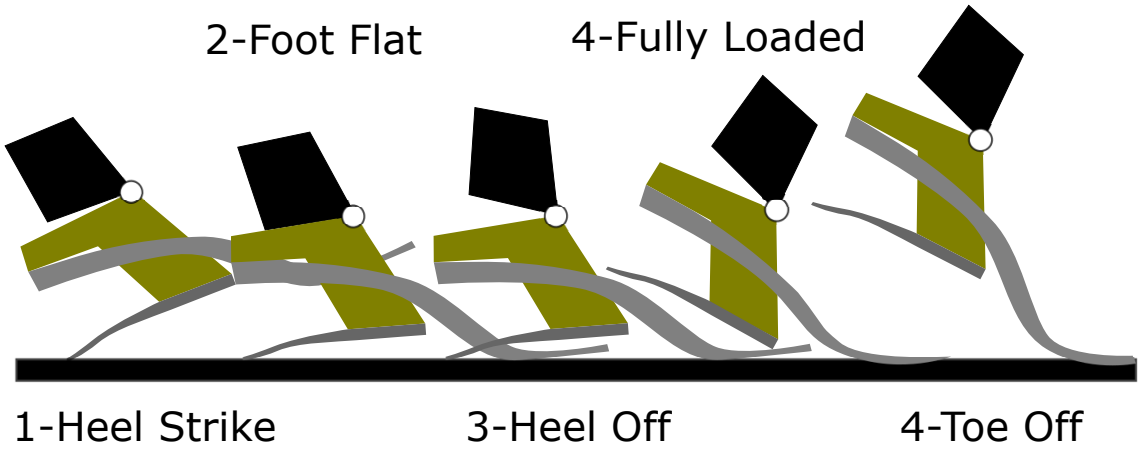

Figure 8.10: Definition of subsections of prosthesis gait stance phase.

of springs on toe and heel to absorb energy when landing and provide push-off at the end of stance phase. *Echelon* is a passive prosthesis which can move about 10 deg in dorsiflexion and plantarflexion. It is achieved by a pivot point connected to hydraulic circuit. On both direction of motion, flow restrictor valves are used to adjust the flow rate which is equivalent to damping, see Figure 8.11b.

The prosthesis is installed under distal pyramid interface. It is able to change the angle of connection over 10 deg. The product is expected to wear a cosmetic prosthesis cover and a shoe. However, in order to observe the bending of heel and toe spring, I used a bare prosthesis. Without a cosmetic prosthesis cover and a shoe, there is more space between the heel and the treadmill when the shank is at vertical position. Optcam was used to capture the HGS motion and prosthesis ankle angle. Reflective markers are located at hip, knee, shank, ankle, toe and heel position (The heel is higher). I estimated the ankle angle from the angle of shank (DE) and the ankle of foot (AB). The ankle angle during the initial swing phase is defined as initial ankle angle (IAA). IAA can be tuned by changing the connection angle of the top interface. To prevent the prosthesis slip on the treadmill, two pieces of rubber were attached under the heel and toe.

8.2.3 Experiment with Different Damping Settings

I start the HGS with a manually designed ellipse trajectory with hip joint and knee joint. The required hip height is from Opensim model and it is normalised according to the robot leg length. The simulated human walking gait parameters is displayed in Table 8.1.

Table 8.1: Simulated Gait Parameters for experiments.

Simulated Gait Parameters				
Body Weight	Leg Length	IAA	Damping	Walking Speed
53.41 kg	0.7 m	1°	Soft/Medium/Hard	0.84 m/s

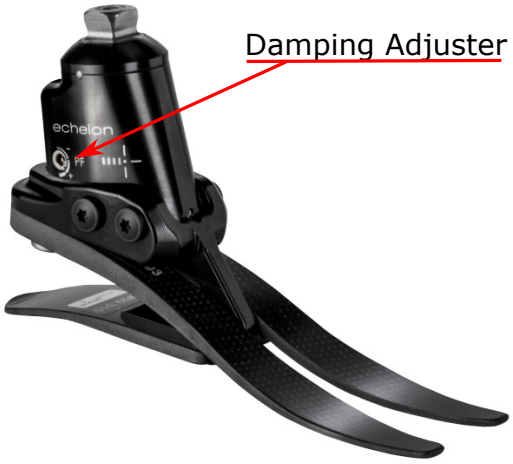

(a) Echlon Passive Ankle Prosthesis.

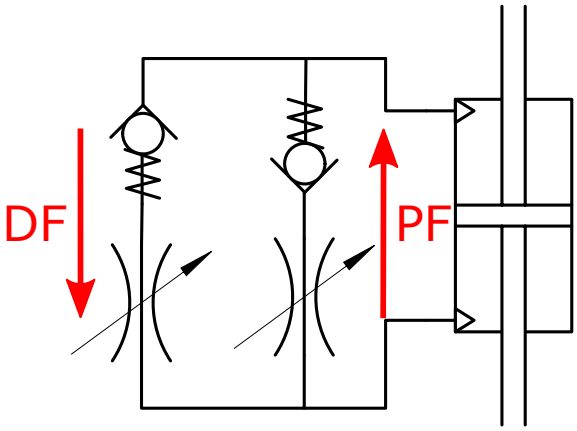

(b) Hydrualic Circuit.

Figure 8.11: (a) *Echelon* Passive Ankle Prosthesis. It has damping adjuster on two sides of the prosthesis. (b) Hydrualic Circuit. The ankle is connected with the cylinder on the right. Two restrictor valve along with one directional valve are used to adjust the damping.

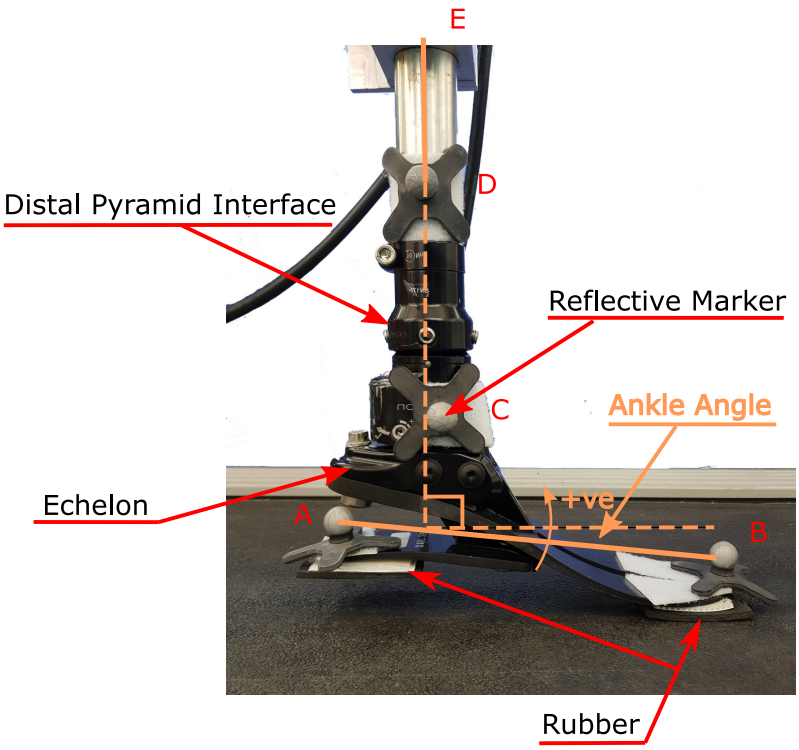

Figure 8.12: Installation of *Echelon* prosthesis. The *Echelon* is connected with the HGS through a distal pyramid interface. Markers are placed on A-heel, B-toe, C-ankle, D-shank, E-knee. (E Marker is not shown in the figure).

I changed the damping coefficients of PF and DF of *Echelon* at the same time to three levels: Soft, Medium and Hard, which means the restrictor valves are fully open, half open and almost closed respectively. Same starting position and same required GRF were provided. The gait cycle is divided into swing phase and stance phase. The stance phase is focused only.

The experiment results including ankle angle, normalised ankle moment and normalised ankle power are shown in Figure 8.13.

First, the ankle angles are compared. The prosthesis ankle angle has the same IAA with able-body ankle angle. In the CP phase, the prosthesis plantar flex 8°to 10°while the able-body rotates 3°. With higher damping, the ankle has less plantarflexion. During the CD phase, the able-body rotates the ankle more linearly than the prosthesis does. The prosthesis ankle angle change is different because that it is caused not only pivot rotation but also spring compression. In the PP phase, able-body ankle rotates from 14°to 6°, which is doubled of prosthesis's angle change. Without active control, the passive prosthesis is only able to return to the IAA. The large plantarflexed angle in the able-body group ensures enough energy to propel the body.

Then, the ankle moments are compared. One can observe that the prosthesis ankle moments are larger than able-body moment in the CP phase due to the PF damping of the prosthesis. With higher damping setting, the moment is larger. During the CD phase, the moment of prosthesis increase positively faster than able-body moment, which corresponds to the ankle angle change. Due to the lack of

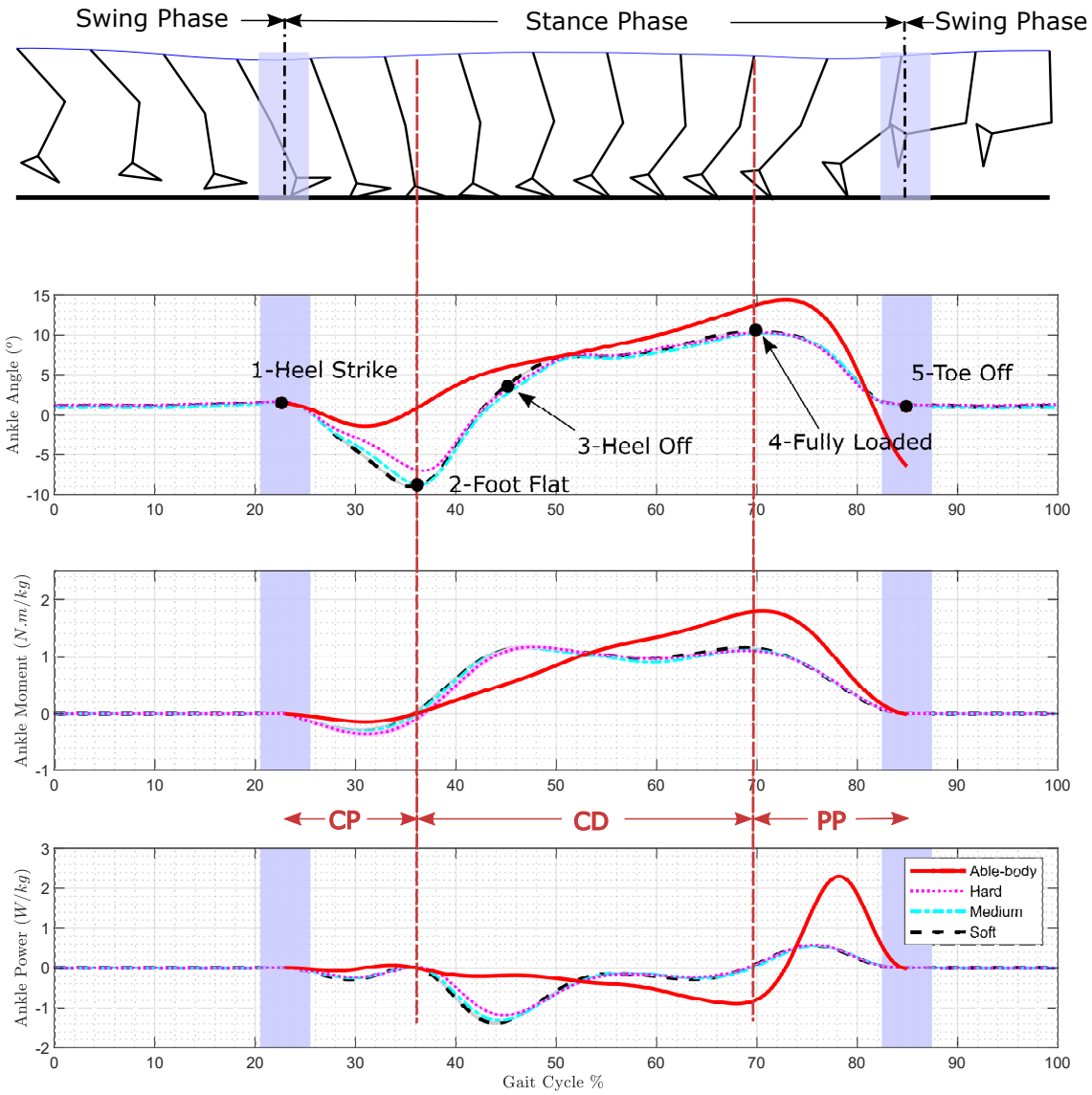

Figure 8.13: The average result of the prosthesis testing and the able-body data. On the top, the captured motion from OptCam is presented. Top plot is ankle dorsiflexion angle. Middle plot is the normalized ankle extension moment. Bottom plot is the normalized ankle extension power. Solid red line is an able-body reference result from Opensim model.

active motion ability, the passive prosthesis has less moment than able-body.

In the end, the ankle powers are compared. Different from able-body, passive prosthesis absorb the early landing contact between the foot and the ground. During CD phase, the able-body ankle gradually increases the negative power and stores energy in the ankle. For the *Echelon* ankle, negative power is used to overcome the ankle DF damping and store energy. In the PP phase, the able-body ankle plantarflexs and the peak power is almost 4 times of the peak power from *Echelon*.

The proportions of each subsections are presented in Table 8.2. The CP phase of *Echelon* ankle has 7 % more of the total stance phase. The CD phase is 12 % more, and the PP phase is 5 % less. One can see that the proportions of each subsections don't vary much with different damping settings. The std shows that the experiment data is consistent which is better than human testing.

Table 8.2: Comparison of the stance phase subsections duration of different prosthesis damping settings.

Stance Phase 100 %			
Group	CP	CD	PP
Able-body	13.0 %	67.7 %	19.3 %
Soft	20.7 ± 0.29 %	55.3 ± 0.46 %	24.0 ± 0.37 %
Medium	21.6 ± 0.27 %	54.2 ± 0.26 %	23.2 ± 0.33 %
Hard	22.3 ± 0.24 %	54.3 ± 0.36 %	23.4 ± 0.42 %

The energy cost of each subsections are shown in Figure 8.14. Compare three damping settings, in the CP phase, they have same amount of energy dissipation. During the CD phase, slight more energy is dissipated or stored for the soft setting. The energy generation of PP phase for three settings is similar. Assuming spring energy is fully stored in the CD phase and released in the PP phase, the dissipated energy from the damping in CD phase can be roughly estimated from the energy difference between CD and PP. One can conclude that lower damping dissipates more energy than higher damping, which is due to the larger angle change. It means the lower damping is less efficient. Compare the prosthesis data to the able-body energy data, the biggest differences are the CP phase and PP phase. The able-body ankle doesn't absorb energy during the CP phase, and it provides almost 3 times energy of the *Echelon*.

In our test, the damping setting of the ankle is concluded that a harder setting is better, because it reduces the energy waste. However, hard setting of ankle damping might cause discomfort to the user due to a rougher touch down. The moment of ankle in hard setting during the touch down is higher. It means the connection of socket will cause more stress at the socket surface. A compromise of comfort and efficiency is needed.

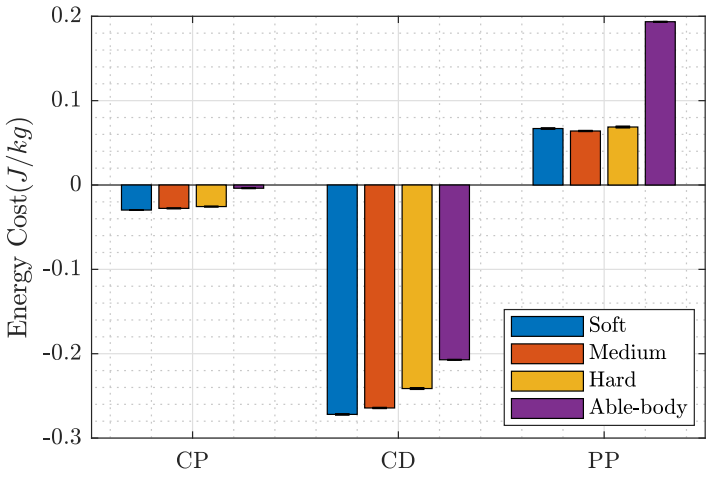

Figure 8.14: Subsection ankle energy cost of testing different damping setting of Echelon during the stance phase.

8.2.4 Experiment of Different Foot Connection Angle

Similar to previous Section 8.2.3, I start the HGS with a manually designed ellipse trajectory with hip joint and knee joint. The damping setting of DF and PF remains the same in medium level. The distal pyramid interface is set to be Dorsi, Neutral and Plantar, which is equivalent of changing the IAA angle, see Figure 8.15. The detailed simulated parameters is shown is Table 8.3. Same starting position and same required GRF were provided.

Table 8.3: Simulated Gait Parameters

Simulated Gait Parameters				
Body Weight	Leg Length	IAA	Damping	Walking Speed
$53.41\,kg$	$0.7\,m$	6°/-1°/-7°	Medium	$0.84\,m/s$

The result of prosthesis ankle angle, ankle moment and ankle power are shown in Figure 8.16.

First, the ankle angles are analysed. During the CP phase, with more dorsiflexed IAA, the prosthesis rotates more. More plantarflexed IAA leads to earlier foot flat. In the CD phase, the toe spring of the Plantar group is compressed earlier than the other two groups. In the PP phase, three groups plantar flexed over similar angle and they are all half of the angle of the Able-body group. This means IAA doesn't change how much the prosthesis rotates in the PP phase. The dominate factor is the toe spring.

Then, the ankle moments are checked. In the CP phase, group Dorsi has the largest negative moment. All three groups return to 0 moment in the end of their CP phase which corresponds with foot flat. In the CD phase, group Dorsi increases positive moment, while group Neutral keeps roughly similar moment and group

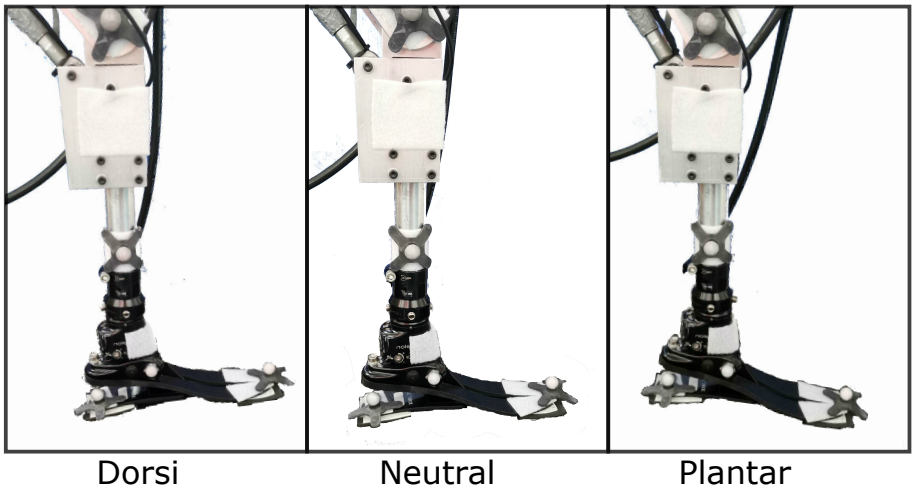

Figure 8.15: *Echelon* is installed at with different IAA. The IAA of Dorsi is 6°, Neutral is -1°and Plantar is -7°.

Plantar decreases positive moment. It is because that the moment mainly comes from the vertical force, the arm of the moment is related to the ankle angle. One can see the ankle moment corresponds with the ankle angle.

For the power plot, the biggest difference comes from the CP phase. Group Plantar has very little negative power, it is closest to group Able-body. In the CD phase, three groups all overcome the DF damping and compress foot springs. In the PP phase, three groups show not enough power are provided comparing to group Able-body.

The proportions of each subsections are presented in Table 8.4. The group Plantar has the most similar proportions comparing to the Able-body group. With more dorsi flexed IAA, CP phase and PP phase is longer. CD phase is increased if IAA is more plantar flexed.

Table 8.4: Comparison of the stance phase subsections duration of different prosthesis IAA.

Stance Phase 100 %			
Group	CP	CD	PP
Able-body	13.0 %	67.7 %	19.3 %
Plantar	12.7 ± 0.42 %	66.2 ± 0.44 %	21.1 ± 0.28 %
Neutral	20.7 ± 0.22 %	56.6 ± 0.45 %	22.7 ± 0.50 %
Dorsi	30.6 ± 0.36 %	41.5 ± 0.30 %	28.1 ± 0.31 %

The subsection ankle energy cost in the stance phase is shown in Figure 8.17. In CP phase, group Dorsi dissipates most energy in CP phase. It means a softer touchdown is able to be achieved. Although the group Plantar has the similar energy cost in CP phase, little energy dissipation might cause discomfort at the socket connection to amputees. Larger energy cost is observed for group Dorsi in the CD phase. Assuming the energy released in the PP phase comes from the stored energy

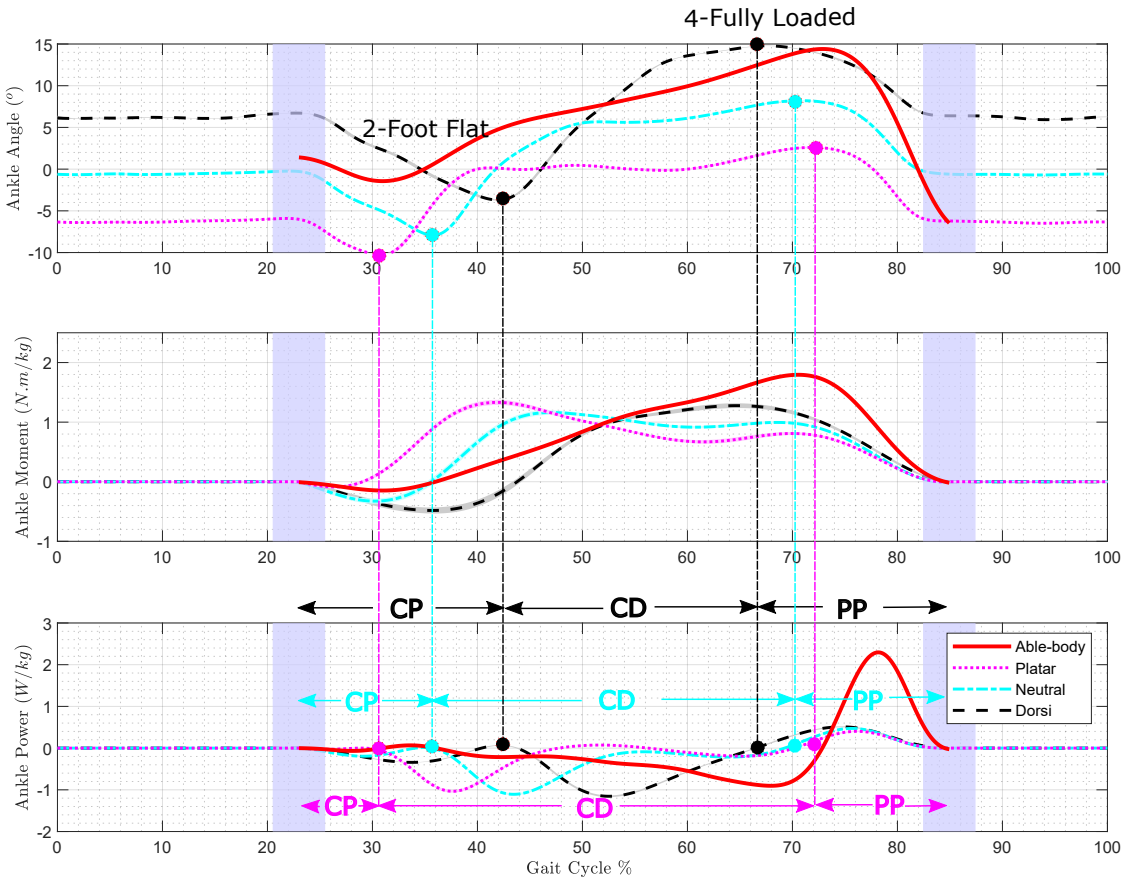

Figure 8.16: The test results of different IAA with *Echelon*. Top plot is ankle dorsiflexion angle. Middle plot is the normalized ankle extension moment. Bottom plot is the normalized ankle extension power. Solid red line is an able-body reference result from Opensim model.

only in the CD phase, the energy cost in CD phase to overcome the DF damping is roughly the same, which agrees with the same damping setting. Although the PP phase peak power is similar for three groups (Figure 8.17), group Dorsi has the highest energy released, it is because of the longer PP time (Table 8.4).

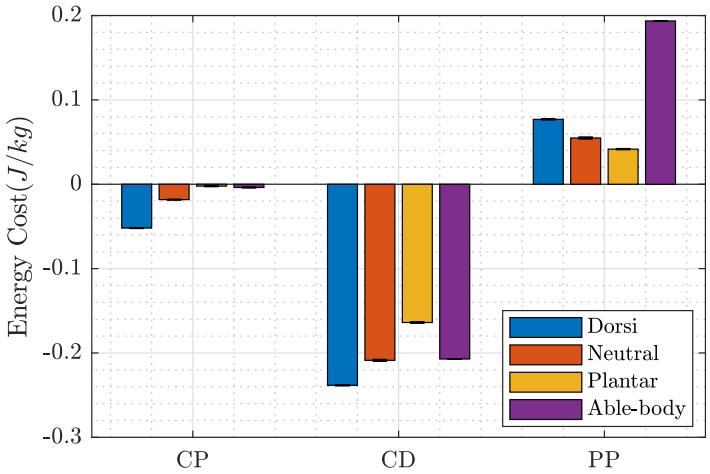

Figure 8.17: Subsection ankle energy cost of different IAA installation groups during stance phase.

The subsection ankle energy cost in the stance phase is shown in Figure 8.17. In CP phase, group Dorsi dissipates most energy in CP phase. It means a softer touch-down is able to be achieved. Although the group Plantar has the similar energy cost in CP phase, little energy dissipation might cause discomfort at the socket connection to amputees. Larger energy cost is observed for group Dorsi in the CD phase. Assuming the energy released in the PP phase comes from the stored energy only in the CD phase, the energy cost in CD phase to overcome the DF damping is roughly the same, which agrees with the same damping setting tests. Although the PP phase peak power is similar for three groups (Figure 8.17), group Dorsi has the highest energy released, it is because of the longer PP time (Table 8.4).

In this test, the Dorsi group has the best performance from the energy cost perspective. The Plantar group has the most similar subsections with Able-body group. In the user install instructions of *Echelon* [114], the initial installation socket angle is closest to the Dorsi group. The difference in the subsection durations may be because our tests were conducted without a cosmetic foot cover and a shoe.

8.2.5 Energy Contribution from the HGS

For the same two group of tests, different prosthesis damping and different foot connect angles, the energy cost of the hydraulic test rig HGS is calculated and discussed in this section.

Experiment with Different Damping Settings

The overall energy cost of the test during the stance phase are shown in Figure 8.18. As one can expect, the passive prosthesis ankle joint is dissipating energy because of its damping effect. The ankle joint in the able-body group has small energy dissipation overall.

In other two joints, compared to Able-body group, the hip joint spends much less energy and knee joint spends 6 times more energy for all three groups. A small difference can be seen between different damping groups. It shows that the gait is different from the human natural gait. The knee joint for human is very efficient because the knee locks itself during the stance phase. For the robot generated gait in this test, the knee contributes some energy which is originally supposed to be generated by the hip. The damping can only influence a little of the energy cost.

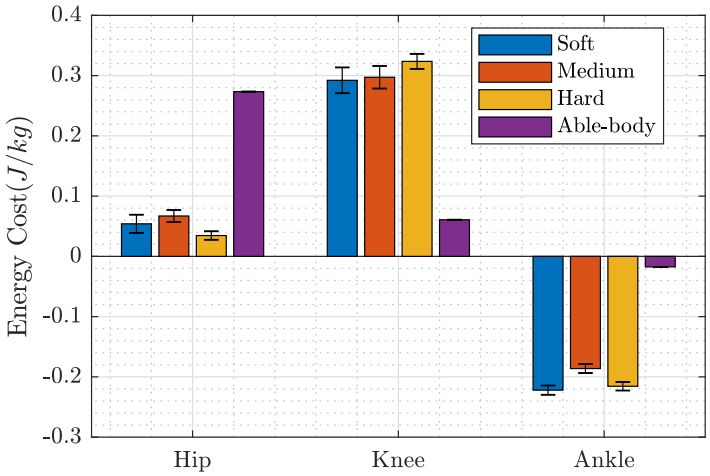

Figure 8.18: Energy cost of the HGS leg for different damping setting test.

Experiment with Different Foot Connection Angle

Experiment with different foot connection angle shows very different energy change for each angle groups. In Figure 8.19, as IAA increases (towards upright position), the overall ankle energy dissipation increases, it is mainly because the foot rotates more in the CP and CD phase phase compare to the other groups. For the hip and knee joint energy, as IAA increases, the hip joint cost more energy and knee joint cost less energy. The Dorsi group has the closest performance compare to the Able-body group.

Limitations of Energy Analysis

It is important to notice that the energy match to able body group doesn't entirely means a product setting is better. Our energy analysis is staying in the mechanical level. The energy cost due to the muscle stretching or the metabolic energy cost is ignored. The total energy liberation for each muscle, $\dot{E}$ is the sum of activation

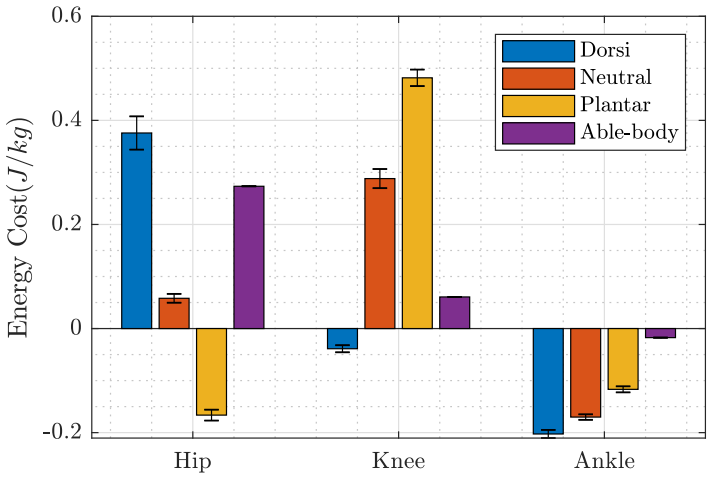

Figure 8.19: Energy cost of the HGS leg for different IAA.

($\dot{h_A}$), maintenance ($\dot{h_M}$), and shortening/lengthening ($\dot{h_{SL}}$) heat rates, as well as the mechanical work rate ($\dot{W_{CE}}$) of the contractile element Equation 8.1. A large moment at joints could also leads to high energy cost for the gait, due to the maintenance ($\dot{h_M}$). These part of energy cost could be estimated potentially by joint force impulses.

$$\dot{E} = \dot{h_A} + \dot{h_M} + \dot{h_{SL}} + \dot{W_{CE}} \tag{8.1}$$

8.3 Experiments Conclusion

In this chapter, we first checked the effectiveness of the proposed EILC on stationary ground and moving surface. On stationary ground, the EILC was demonstrated to control the GRF in horizontal and vertical directions. The error for both direction was reduced to around $10\,N$ which is $2\,\%$ of the maximum vertical force reference. On the moving surface, the method was successfully implemented with passive and active prostheses. The error for both direction was reduced to $25\,N$ which is $5\,\%$ of the maximum vertical force reference. The results give the foundation to implement the IDA type of prosthesis testing.

The passive *Echelon* was tested as a study case. The first group of test used different damping setting and fixed Initial Ankle Angle (IAA). The generated gait was different from human gait. The Controlled Dorsiflexion (CD) phase is $12\,\%$ shorter and Powered Plantarflexion (PP) phase is 5% longer than Able-body phases. The prosthesis was not providing enough push-off power in the PP phase, which was only 1/3 to the Able-body push-off power. Compared within the group, only a little difference was observed. With harder damping, the prosthesis has less energy absorption during Controlled Plantarflexion (CP) and CD phase. For the robot leg energy of the Hydraulic Gait Simulator (HGS), the generated gait has 6 times energy on knee joint and much less energy at hip joint comparing to the Able-body

data.

The second group of test used different IAA and medium damping. The IAA change showed an effective change of the generated gait. Larger IAA resulted in longer PP, CP phase and shorter CD phase. It also made greater energy dissipation in CP and CD phase. The Dorsi group was found to provide the most power during the PP phase. For the robot leg energy of the HGS, the generated gait has the closest energy distribution to the Able-body data in the Dorsi group.

The proposed IDA method has been demonstrated to be able to generate a walking gait with the test prosthesis. Changing prosthesis settings were proven to have effect on gait parameters, especially IAA. From the prosthesis ankle joint and the HGS energy results, the Dorsi group gait was found the closest to the Able-body gait, and the corresponding setting is similar with the setting from the original *Echelon* user install instruction. It proved that the IDA method has the potential to help adjust the prosthesis settings to replace human.

Chapter 9

Conclusions and Future Work

9.1 Conclusions

The conventional lower limb prostheses test methods: model-based testing and human-based testing both have their drawbacks. model-based testing lacks fidelity while direct human-based testing is not safe. Research has been carried out to fill the gap between model-based testing and human-based testing. Several gait simulators have been developed. Most of them are only able to replicate human gait motion. Few literature has covered the prosthesis settings change during a test. I aimed at proposing a new test approach to evaluate a lower limb prosthesis and assist in improving its performance.

The study began with an investigation of applying Hardware-in-the-Loop (HIL) in testing lower limb prostheses. The HIL was hard to achieve. The main challenge has been identified on the compensate of the very stiff ground contact discontinuity. I then developed a Hydraulic Gait Simulator (HGS) to test lower limb prostheses. Both simulation and experimental studies on the HGS were carried out. The Inverse Dynamic Approach (IDA) of test prostheses was chosen. In order to achieve Ground Reaction Force (GRF) control, I derived an Extended Iterative Learning Control (EILC) algorithm to control horizontal and vertical contact force (forces in sagittal plane). The algorithm was proven to be effective on both passive and active prostheses when used on stationary and moving ground.

For the simulation studies, the HGS has been modelled in MATLAB/Simulink and MATLAB/Multibody environment. The model accuracy was validated by comparing results of simulation and experiment results with chirp signal commands. A series of tests were carried out to validate the proposed control algorithm. With the EILC force controller, the GRF was controlled in both horizontal and vertical directions successfully.

For the experimental studies, the experimental tests were undertaken on the xPC Target real-time control platform. The EILC force controller was validated experimentally. Then, demonstrations of testing passive ankle prosthesis *Echelon* were carried out. Through two series of tests, the HGS was used to evaluate the performance of *Echelon* when the damping setting is changed and the install angle is changed. These parameters influence the ankle angle, ankle moment and ankle

power testing result. One can improve the test result by tuning the settings of the prosthesis.

The HGS has been proven to be useful in developing ankle prostheses. For other types of prostheses, the HGS can be modified to test them. The idea of Forward Dynamic Approach (FDA), Inverse Dynamic Approach (IDA) and Hybrid Approach (HA) tests can be a guide line for future gait simulator tests. For *Echelon* itself, I observed that during the Controlled Dorsiflexion (CD) phase, more energy was cost to overcome the damping for *Echelon* comparing to able-body. Consistent with previous research, a passive ankle prosthesis is not able to provide enough push-off power during the PP phase [8], [14], [20]).

To make the generated gait more similar to human gait, two possible changes can be addressed for *Echelon*:

- Reduce the Dorsiflexion (DF) damping or assist ankle rotate in the Controlled Dorsiflexion (CD) phase. It can be done with active control of damping.

- More push-off power is required in the Powered Plantarflexion (PP) phase.

9.2 Final comments and Future work

Throughout the research, the gap mentioned in the literature is filled. The research has expanded the knowledge in lower limb prostheses testing in the Robot-based Testing category. The developed HGS is able to generate a gait that achieves expected walking GRF in both vertical and anterior direction. Lower limb prostheses performance can be evaluated in a systematical and quantified manner by checking ankle joint kinematics, dynamics and the HGS energy. The biggest limitation of the research is that the HGS was built from HyQ leg. Although I have kept the upper and lower leg length ratio similar to human anthropometric leg ratio, the absolute leg lengths are shorter than adult legs. The leg lengths may influence the test result when it comes to knee joint and hip joint analysis. Our analysis is staying on the mechanical level. Muscle activities are ignored. It is a disadvantage compare to skeletal system model study. I have given recommendations for improving the *Echelon* through the HGS test on it. The recommendations of improving the *Echelon* will need to be verified with *vivo* testing.

In the future, there are a number of potential areas that can be explored:

- Explore more in HIL testing on prostheses. The very stiff ground contact compensation can be further investigated. From the model point of view, skeleton model provides the most useful information, but efficiency of the model needs to be improved to satisfy real time test. The criterion to evaluate performance needs more thinking.

- Improve the HGS physical design. The current configuration brings a problem of vibrations due to the long beam over the robot leg. It can be improved by changing the beam to shift the natural frequency higher or introducing control methods to reduce the vibration.

- Extend the current test plane to 3D. The current test is limited in the sagittal plane. Consider other plane will make the test closer to realistic human usage.
- Improve the ILC to continuous motion learning process. In our research, I applied EILC offline. This means after each cycle, the HGS stops the motion. I am not able to investigate the prosthesis influence on the swing phases. In reality, the ankle prostheses usually has the problem of not creating enough space during the swing phase. It will trip the user up.
- Investigate a humanoid robot with an unfamiliar prosthetic foot. It will be very interesting to see how a humanoid robot learns to balance itself, walk or run. The optimisation problem might show some similarity with human gait learning.
- Investigate other position controllers in the low level control. For example, impedance control is a type of controller suitable for lower limb prosthesis testing. It will prevent an unexpected large load applied on the test prostheses.
- Experimental test with more parameters. In our research, I have only demonstrated the different damping settings and Initial Ankle Angle (IAA). Different walking speed, ground inclination can be investigated. Active prostheses push-off timing, power level can also be investigated.

References

[1] K. Ziegler-Graham, E. J. MacKenzie, P. L. Ephraim, T. G. Travison, and R. Brookmeyer, "Estimating the Prevalence of Limb Loss in the United States: 2005 to 2050," *Archives of Physical Medicine and Rehabilitation*, vol. 89, no. 3, pp. 422–429, Mar. 2008, ISSN: 0003-9993.

[2] F. Guillemin, J. Paysant, K. Demet, J.-M. AndrÉ, and N. Martinet, "Health related quality of life and related factors in 539 persons with amputation of upper and lower limb," *Disability and Rehabilitation*, vol. 25, no. 9, pp. 480–486, 2003, ISSN: 0963-8288.

[3] R. Sinha and W. J. A. V. D. Heuvel, "Factors affecting quality of life in lower limb amputees," 2011.

[4] M. Colette and S. Gerry, "Amputation and rehabilitation," *Surgery(Oxford)*, vol. 28, no. 6, pp. 284–287, 2010, ISSN: 0263-9319.

[5] S. K. Au, J. Weber, and H. Herr, "Biomechanical design of a powered ankle-foot prosthesis," *2007 IEEE 10th International Conference on Rehabilitation Robotics, ICORR'07*, vol. 00, no. c, pp. 298–303, 2007, ISSN: 03642348.

[6] J. Zhu, Q. Wang, and L. Wang, "On the design of a powered transtibial prosthesis with stiffness adaptable ankle and toe joints," *IEEE Transactions on Industrial Electronics*, vol. 61, no. 9, pp. 4797–4807, 2014, ISSN: 02780046.

[7] F. Sup, A. Bohara, and M. Goldfarb, "Design and Control of a Powered Transfemoral Prosthesis.," *The International journal of robotics research*, vol. 27, no. 2, pp. 263–273, 2008, ISSN: 1741-3176. arXiv: NIHMS150003.

[8] T. Yu, A. Plummer, and P. Iravani, "The design of a powered ankle prosthesis with electrohydrostactic actuation," *ASME/BATH 2015 Symposium on Fluid Power and Motion Control*, pp. 6–11, 2015.

[9] T. Yu, A. R. Plummer, P. Iravani, J. Bhatti, S. Zahedi, and D. Moser, "The Design, Control, and Testing of an Integrated Electrohydrostatic Powered Ankle Prosthesis," *IEEE/ASME Transactions on Mechatronics*, vol. 24, no. 3, pp. 1011–1022, 2019, ISSN: 10834435.

[10] International Organization for Standardization, *Prosthetics – Structural testing of lower-limb prostheses – Requirements and test methods ISO 10328:2006*, 2006.

[11] ——, *Prosthetics - Testing of ankle-foot devices and foot units - Requirements and test methods. ISO 22675:2006*, 2006.

[12] E. P. Grabke and J. Andrysek, "Applications of Musculoskeletal Modelling And Simulation For Lower-Limb Prosthesis Design Optimization," *ASME 2018 International Design Engineering Technical Conferences and Computers and Information in Engineering Conference*, pp. 1–9, 2018.

[13] T. Lenzi, M. Cempini, L. Hargrove, and T. Kuiken, "Design, development, and testing of a lightweight hybrid robotic knee prosthesis," *International Journal of Robotics Research*, vol. 37, no. 8, pp. 953–976, 2018, ISSN: 17413176.

[14] P. Malcolm, R. Quesada, E, and J. M. Caputo, "The influence of push-off timing in a robotic ankle-foot prosthesis on the energetics and mechanics of walking," *Journal of NeuroEngineering and Rehabilitation*, vol. 12, no. 21, 2015.

[15] M. W. D Levine, J Richards, *Whittle's Gait Analysis*, Fifth Edit. 2012, pp. 32–33.

[16] M. Ackermann, *Dynamics and Energetics of Walking with Prostheses*, July. P.hD. Thesis of University of Stuttgart, 2007, pp. 192–193, ISBN: 9783832267186.

[17] M. P. Kadaba, H. K. Ramakrishnan, and M. Wootten, "Measurement of lower extremity kinematics during level walking," *Journal of Orthopaedic Research*, pp. 397–398, 1990, ISSN: 07360266.

[18] M. P. Murray, "Gait as a total pattern of movement," *American journal of physical medicine*, vol. 46 1, pp. 290–333, 1967.

[19] A. Thorstensson and H. Roberthson, "Adaptations to changing speed in human locomotion: speed of transition between walking and running," *Acta Physiologica*, vol. 131, no. 2, pp. 211–214, 1987.

[20] J. J. Rice, J. M. Schimmels, and S. Huang, "Design and Evaluation of a Passive Ankle Prosthesis With Powered Push-Off," *Journal of Mechanisms and Robotics*, vol. 8, no. 2, p. 021 012, 2015, ISSN: 1942-4302.

[21] E. Y. Chao, R. K. Laughman, E. Schneider, and R. N. Stauffer, "Normative data of knee joint motion and ground reaction forces in adult level walking," *Journal of Biomechanics*, vol. 16, no. 3, pp. 219–233, 1983, ISSN: 00219290.

[22] C. Richards, "Evaluation of abnormal gait patterns by intermittent light photography and electromyography," *Scand J rehab Med*, pp. 61–68, 1974.

[23] R. Riener, M. Rabuffetti, and C. Frigo, "Stair ascent and descent at different inclinations," *Gait and Posture*, vol. 15, no. 1, pp. 32–44, 2002, ISSN: 09666362.

[24] S. Lajpah, R. Kamnik, and M. Munih, "Kinematics based sensory fusion for wearable motion assessment in human walking," *Computer Methods and Programs in Biomedicine*, vol. 116, no. 2, pp. 131–144, 2014, ISSN: 18727565.

[25] D. Sutherland, "The development of mature gait," *Gait and Posture*, vol. 6, no. 2, pp. 163–170, 1997, ISSN: 0966-6362.

[26] V. Macellari, C. Giacomozzi, and R. Saggini, "Spatial-temporal parameters of gait: Reference data and a statistical method for normality assessment," *Gait and Posture*, vol. 10, no. 2, pp. 171–181, 1999, ISSN: 09666362.

[27] B. M. A. House, T. Square, D. Crisan, H. Boedihardjo, and L. Don, "Spatio-temporal parameters of gait measured by an ambulatory system using miniature gyroscopes," *Journal of Biomechanics*, vol. 35, pp. 689–699, 2002, ISSN: 00219290. arXiv: `arXiv:1011.1669v3`.

[28] N. Sekiya and H. Nagasaki, "Reproducibility of the walking patterns of normal young adults: Test-retest reliability of the walk ratio (step-length/step-rate)," *Gait and Posture*, vol. 7, no. 3, pp. 225–227, 1998, ISSN: 09666362.

[29] D. Winter, *Biomechanics and Motor Control of Human Movement*. 2009, vol. 2nd, p. 277, ISBN: 0470398183.

[30] D. A. Winter, "Overall principle of lower limb support during stance phase of gait," *Journal of Biomechanics*, vol. 13, no. 11, pp. 923–927, 1980, ISSN: 00219290.

[31] A. Hof, "On the interpretation of the support moment," *Gait and Posture*, 2000, ISSN: 0022-4812.

[32] K. Masani, M. Kouzaki, and T. Fukunaga, "Variability of ground reaction forces during treadmill walking," *Journal of Applied Physiology*, vol. 92, no. 5, pp. 1885–1890, 2002, ISSN: 8750-7587.

[33] A. Protopapadaki, W. I. Drechsler, M. C. Cramp, F. J. Coutts, and O. M. Scott, "Hip, knee, ankle kinematics and kinetics during stair ascent and descent in healthy young individuals," *Clinical Biomechanics*, vol. 22, no. 2, pp. 203–210, 2007, ISSN: 02680033.

[34] B. McFadyen and D. Winter, "An Integrated Biomechanical Analysis of Normal Stair Asecent and Descent," *Journal of Biomechanics*, vol. 21, no. 9, pp. 733–744, 1988, ISSN: 0021-9290.

[35] D. D. D'Lima, B. J. Fregly, S. Patil, N. Steklov, and C. W. Colwell, "Knee joint forces: Prediction, measurement, and significance," *Proceedings of the Institution of Mechanical Engineers, Part H: Journal of Engineering in Medicine*, vol. 226, no. 2, pp. 95–102, 2012, ISSN: 09544119.

[36] A. H. Vrieling, H. G. van Keeken, T. Schoppen, E. Otten, J. P. Halbertsma, A. L. Hof, and K. Postema, "Gait initiation in lower limb amputees," *Gait and Posture*, vol. 27, no. 3, pp. 423–430, 2008, ISSN: 09666362.

[37] F. Farahmand, T. Rezaeian, R. Narimani, and P. H. Dinan, "Kinematic and dynamic analysis of the gait cycle of above-knee amputees," *Scientia Iranica*, vol. 13, no. 3, pp. 261–271, 2006, ISSN: 10263098.

[38] D. J. Sanderson and P. E. Martin, "Lower extremity kinematic and kinetic adaptations in unilateral below-knee amputees during walking," *Gait and Posture*, vol. 6, no. 2, pp. 126–136, 1997, ISSN: 09666362.

[39] I. Kovač, V. Medved, and L. Ostojić, "Ground reaction force analysis in traumatic transtibial amputees' gait," *Collegium Antropologicum*, vol. 33, no. SUPPL.2, pp. 107–114, 2009, ISSN: 0350-6134.

[40] R. J. Zmitrewicz, R. R. Neptune, J. G. Walden, W. E. Rogers, and G. W. Bosker, "The Effect of Foot and Ankle Prosthetic Components on Braking and Propulsive Impulses During Transtibial Amputee Gait," *Archives of Physical Medicine and Rehabilitation*, vol. 87, no. 10, pp. 1334–1339, 2006, ISSN: 00039993.

[41] M. L. Van Der Linden, S. E. Solomonidis, W. D. Spence, N. Li, and J. P. Paul, "A methodology for studying the effects of various types of prosthetic feet on the biomechanics of trans-femoral amputee gait," *Journal of Biomechanics*, vol. 32, no. 9, pp. 877–889, 1999, ISSN: 00219290.

[42] A. M. Grabowski and S. D'Andrea, "Effects of a powered ankle-foot prosthesis on kinetic loading of the unaffected leg during level-ground walking," *Journal of NeuroEngineering and Rehabilitation*, vol. 10, no. 49, pp. 1–11, 2013, ISSN: Journal of NeuroEngineering and Rehabilitation.

[43] D. W. Heitzmann, F. Salami, A. R. De Asha, J. Block, C. Putz, S. I. Wolf, and M. Alimusaj, "Benefits of an increased prosthetic ankle range of motion for individuals with a trans-tibial amputation walking with a new prosthetic foot," *Gait and Posture*, vol. 64, no. December 2017, pp. 174–180, 2018, ISSN: 18792219.

[44] H. M. Herr and A. M. Grabowski, "Bionic ankle-foot prosthesis normalizes walking gait for persons with leg amputation.," *Proceedings. Biological sciences / The Royal Society*, vol. 279, no. 1728, pp. 457–64, 2012, ISSN: 1471-2954.

[45] H. Miranda, E. Perez, E. Fernandez, F. Rosselot, J. F. Vergara, W. W. Wolstenholme, and A. Zuazo, "Androgens and effects of opioids and catecholamines on the smooth muscle of the rat vas deferens1," *Pharmacology*, vol. 30, no. 3, pp. 168–180, 2003, ISSN: 14230313.

[46] H. Geyer, A. Seyfarth, and R. Blickhan, "Compliant leg behaviour explains basic dynamics of walking and running.," *Proceedings. Biological sciences / The Royal Society*, vol. 273, no. 1603, pp. 2861–2867, 2006, ISSN: 0962-8452.

[47] J. Rummel, Y. Blum, and A. Seyfarth, "Robust and efficient walking with spring-like legs," *Bioinspiration & Biomimetics*, vol. 5, no. 4, p. 046 004, 2010, ISSN: 1748-3182.

[48] H. Hong, S. Kim, C. Kim, S. Lee, and S. Park, "Spring-like gait mechanics observed during walking in both young and older adults," *Journal of Biomechanics*, vol. 46, no. 1, pp. 77–82, 2013, ISSN: 00219290.

[49] C. K. Jung and S. Park, "Compliant bipedal model with the center of pressure excursion associated with oscillatory behavior of the center of mass reproduces the human gait dynamics," *Journal of Biomechanics*, vol. 47, no. 1, pp. 223–229, 2014, ISSN: 00219290.

[50] B. R. Whittington and D. G. Thelen, "A Simple Mass-Spring Model With Roller Feet Can Induce the Ground Reactions Observed in Human Walking," *Journal of Biomechanical Engineering*, vol. 131, no. 1, p. 011 013, 2008, ISSN: 01480731.

[51] H. Lim, H. Park, and S. Park, "Compliant walking model with a curvy foot reflecting the position of ankle on reproducing the ankle torque profile," *Journal of Mechanical Science and Technology*, vol. 29, no. 6, pp. 2307–2311, 2015, ISSN: 1738494X.

[52] H. Lim and S. Park, "Kinematics of lower limbs during walking are emulated by springy walking model with a compliantly connected, off-centered curvy foot," *Journal of Biomechanics*, vol. 71, pp. 119–126, 2018, ISSN: 18732380.

[53] T. McGeer, "Passive Dynamic Walking," *The International Journal of Robotics R*, 1990.

[54] J. Sushko, C. Honeycutt, and K. B. Reed, "Prosthesis design based on an asymmetric passive dynamic walker," *Proceedings of the IEEE RAS and EMBS International Conference on Biomedical Robotics and Biomechatronics*, pp. 1116–1121, 2012, ISSN: 21551774.

[55] S. Srinivasan, I. A. Raptis, and E. R. Westervelt, "Low-Dimensional Sagittal Plane Model of Normal Human Walking," *Journal of Biomechanical Engineering*, vol. 130, no. 5, p. 051 017, 2008, ISSN: 01480731.

[56] S. Srinivasan, E. R. Westervelt, and a. H. Hansen, "A Low-Dimensional Sagittal-Plane Forward-Dynamic Model for Asymmetric Gait and Its Application to Study the Gait of Transtibial Prosthesis Users," *Journal of Biomechanical Engineering*, vol. 131, no. 3, p. 031 003, 2009, ISSN: 01480731.

[57] Y. Suzuki, "Dynamic optimization of transfemoral prosthesis during swing phase with residual limb model," *Prosthetics and Orthotics International*, vol. 34, no. 4, pp. 428–438, 2010, ISSN: 03093646.

[58] J. Markowitz, P. Krishnaswamy, M. F. Eilenberg, K. Endo, C. B. Chris, and H. Herr, "Speed adaptation in a powered transtibial prosthesis controlled with a neuromuscular model," *Philosophical Transactions of the Royal Society B: Biological Sciences*, vol. 366, no. 1570, pp. 1621–1631, 2011, ISSN: 14712970.

[59] N. P. Fey, G. K. Klute, and R. R. Neptune, "Optimization of Prosthetic Foot Stiffness to Reduce Metabolic Cost and Intact Knee Loading During Below-Knee Amputee Walking: A Theoretical Study," *Journal of Biomechanical Engineering*, vol. 134, no. 11, p. 111 005, 2012, ISSN: 0148-0731.

[60] N. Thatte and H. Geyer, "Towards local reflexive control of a powered transfemoral prosthesis for robust amputee push and trip recovery," *IEEE International Conference on Intelligent Robots and Systems*, no. Iros, pp. 2069–2074, 2014, ISSN: 21530866.

[61] ——, "Toward Balance Recovery With Leg Prostheses Using Neuromuscular Model Control," *IEEE Transactions on Biomedical Engineering*, vol. 63, no. 5, pp. 904–913, 2015, ISSN: 0018-9294.

[62] R. J. Zmitrewicz, R. R. Neptune, and K. Sasaki, "Mechanical energetic contributions from individual muscles and elastic prosthetic feet during symmetric unilateral transtibial amputee walking: A theoretical study," *Journal of Biomechanics*, vol. 40, no. 8, pp. 1824–1831, 2007, ISSN: 00219290.

[63] A. K. Silverman and R. R. Neptune, "Muscle and prosthesis contributions to amputee walking mechanics: A modeling study," *Journal of Biomechanics*, vol. 45, no. 13, pp. 2271–2278, 2012, ISSN: 00219290.

[64] N. T. Pickle, A. M. Grabowski, J. R. Jeffers, and A. K. Silverman, "The Functional Roles of Muscles, Passive Prostheses, and Powered Prostheses During Sloped Walking in People With a Transtibial Amputation," *Journal of Biomechanical Engineering*, vol. 139, no. 11, p. 111 005, 2017, ISSN: 0148-0731.

[65] S. K. Au, J. Weber, and H. Herr, "Powered ankle-foot prosthesis improves walking metabolic economy," *IEEE Transactions on Robotics*, vol. 25, no. 1, pp. 51–66, 2009, ISSN: 15523098.

[66] A. D. Segal, K. E. Zelik, G. K. Klute, D. C. Morgenroth, M. E. Hahn, M. S. Orendurff, P. G. Adamczyk, S. H. Collins, A. D. Kuo, and J. M. Czerniecki, "The effects of a controlled energy storage and return prototype prosthetic foot on transtibial amputee ambulation," *Human Movement Science*, vol. 31, no. 4, pp. 918–931, 2012, ISSN: 01679457. arXiv: `NIHMS150003`.

[67] J. M. Caputo and S. H. Collins, "A universal ankle-foot prosthesis emulator for human locomotion experiments.," *Journal of biomechanical engineering*, vol. 136, no. 3, p. 035 002, 2014, ISSN: 1528-8951.

[68] M. Kim, T. Chen, T. Chen, and S. H. Collins, "An ankle-foot prosthesis emulator with control of plantarflexion and inversion-eversion torque," *IEEE Transactions on Robotics*, vol. 34, no. 5, pp. 1183–1194, 2015, ISSN: 15523098.

[69] T. Ramakrishnan and K. Reed, "Asymmetric Unilateral Transfemoral Prosthetic Simulator," *Master degree thesis*, vol. 1554006, no. May, p. 73, 2014, ISSN: 0717-6163. arXiv: `arXiv:1011.1669v3`.

[70] N. A. Sharkey and A. J. Hamel, "A dynamic cadaver model of the stance phase of gait: performance characteristics and kinetic validation," *Clinical Biomechanics*, vol. 13, no. 6, pp. 420–433, 1998, ISSN: 02680033.

[71] P. M. Aubin, M. S. Cowley, and W. R. Ledoux, "Gait simulation via a 6-DOF parallel robot with iterative learning control," *IEEE Transactions on Biomedical Engineering*, vol. 55, no. 3, pp. 1237–1240, 2008, ISSN: 00189294.

[72] P. M. Aubin, E. Whittaker, and W. R. Ledoux, "A robotic cadaveric gait simulator with fuzzy logic vertical ground reaction force control," *IEEE Transactions on Robotics*, vol. 28, no. 1, pp. 246–255, 2012, ISSN: 15523098.

[73] T. Natsakis, K. Peeters, F. Burg, G. Dereymaeker, J. V. Sloten, and I. Jonkers, "Specimen-specific tibial kinematics model for in vitro gait simulations," *Proceedings of the Institution of Mechanical Engineers, Part H: Journal of Engineering in Medicine*, vol. 227, no. 4, pp. 454–463, 2013, ISSN: 09544119.

[74] K. Peeters, T. Natsakis, J. Burg, P. Spaepen, I. Jonkers, G. Dereymaeker, and J. Vander Sloten, "An in vitro approach to the evaluation of foot-ankle kinematics: Performance evaluation of a custom-built gait simulator," *Proceedings of the Institution of Mechanical Engineers, Part H: Journal of Engineering in Medicine*, vol. 227, no. 9, pp. 955–967, 2013, ISSN: 09544119.

[75] Q. Guo, G. Shi, D. Wang, C. He, J. Hu, and W. Wang, "Iterative learning based output feedback control for electro-hydraulic loading system of a gait simulator," *Mechatronics*, vol. 54, no. August 2017, pp. 110–120, 2018, ISSN: 09574158.

[76] E. De Raeve, T. Saey, L. Muraru, and L. Peeraer, "The use of a robotic gait simulator for the development of an alignment tool for lower limb prostheses," *Journal of Foot and Ankle Research*, vol. 7, no. S1, pp. 2–3, 2014.

[77] M. P. McGrath, J. Gao, J. Tang, P. Laszczak, L. Jiang, D. Bader, D. Moser, and S. Zahedi, "Development of a residuum/socket interface simulator for lower limb prosthetics," *Proceedings of the Institution of Mechanical Engineers, Part H: Journal of Engineering in Medicine*, vol. 231, no. 3, pp. 235–242, 2017, ISSN: 20413033.

[78] H. Richter, D. Simon, W. a. Smith, and S. Samorezov, "Dynamic modeling, parameter estimation and control of a leg prosthesis test robot," *Applied Mathematical Modelling*, vol. 39, no. 2, pp. 559–573, 2015, ISSN: 0307904X.

[79] J. Thiele, S. Gallinger, P. Seufert, and M. Kraft, "The Gait Simulator For Lower Limb Exoprostheses fffdfffdfffd Overview And First Measurements for Comparison of Microprocessor Controlled Knee Joints fffdfffdfffd," *Preliminary report*, vol. 13, pp. 193–203, 2015.

[80] H. Richter and D. Simon, "Robust Tracking Control of a Prosthesis Test Robot," *Journal of Dynamic Systems, Measurement, and Control*, vol. 136, no. 3, p. 031 011, 2014, ISSN: 0022-0434.

[81] R. Davis, H. Richter, D. Simon, and A. Van Den Bogert, "Evolutionary optimization of ground reaction force for a prosthetic leg testing robot," *Proceedings of the American Control Conference*, pp. 4081–4086, 2014, ISSN: 07431619.

[82] V. Azimi, S. Abolfazl Fakoorian, T. Tien Nguyen, and D. Simon, "Robust Adaptive Impedance Control With Application to a Transfemoral Prosthesis and Test Robot," *Journal of Dynamic Systems, Measurement, and Control*, vol. 140, no. 12, p. 121 002, 2018, ISSN: 0022-0434.

[83] D. Simon, "Biogeography-based optimization," *IEEE Transactions on Evolutionary Computation*, vol. 12, no. 6, pp. 702–713, 2008, ISSN: 1089778X.

[84] J. Thiele, B. Westebbe, M. Bellmann, and M. Kraft, "Designs and performance of microprocessorcontrolled knee joints," *Biomedizinische Technik*, vol. 59, no. 1, pp. 65–77, 2014, ISSN: 00135585.

[85] H. Giberti, C. Marinelli, P. Milano, P. Milano, and P. Milano, "Design and control of an active humanoid leg for testing lower-limb prostheses," *Proceedings of the ASME 2014 12th Biennial Conference on Engineering Systems Design and Analysis*, pp. 1–7, 2016.

[86] C. Marinelli, H. Giberti, and F. Resta, "Conceptual design of a gait simulator for testing lower-limb active prostheses," *2015 16th International Conference on Research and Education in Mechatronics (REM)*, pp. 314–320, 2015.

[87] A. Arami, N. V. Martins, and K. Aminian, "Locally linear neuro-fuzzy estimate of the prosthetic knee angle and its validation in a robotic simulator," *IEEE Sensors Journal*, vol. 15, no. 11, pp. 6271–6278, 2015, ISSN: 1530437X.

[88] J. Zhang, L. Shen, L. Shen, and A. Li, "Gait analysis of powered bionic lower prosthesis," *2010 IEEE International Conference on Robotics and Biomimetics, ROBIO 2010*, pp. 25–29, 2010.

[89] a. R. Plummer, "Model-in-the-loop testing," *Proceedings of the Institution of Mechanical Engineers, Part I: Journal of Systems and Control Engineering*, vol. 220, no. 3, pp. 183–199, 2006, ISSN: 0959-6518.

[90] H. K. Fathy, Z. S. Filipi, J. Hagena, and J. L. Stein, "Review of Hardware-in-the-Loop Simulation and Its Prospects in the Automotive Area," *Modeling and Simulation for Military Applications*, vol. 6228, 62280E–62280E–20, 2006, ISSN: 0277786X.

[91] G. Cai, B. M. Chen, T. H. Lee, and M. Dong, "Design and implementation of a hardware-in-the-loop simulation system for small-scale UAV helicopters," *Mechatronics*, vol. 19, no. 7, pp. 1057–1066, 2009, ISSN: 09574158.

[92] V. Rajaram and S. C. Subramanian, "Design and hardware-in-loop implementation of collision avoidance algorithms for heavy commercial road vehicles," *Vehicle System Dynamics*, vol. 54, no. 7, pp. 871–901, 2016, ISSN: 0042-3114.

[93] T. Horiuchi and M. Nakagawa, "Development of a Real-time Hybrid Experimental System with Actuator Delay Compensation," *Eleventh World Conference on Earthquake Engineering*, 1996.

[94] T. Horiuchi, M. Inoue, T. Konno, and Y. Namita, "Real-time hybrid experimental system with actuator delay compensation and its application to a piping system with energy absorber," *Earthquake Engineering and Structural Dynamics*, vol. 28, no. 10, pp. 1121–1141, 1999, ISSN: 00988847.

[95] C. T. Freeman, "Robust ILC design with application to stroke rehabilitation," *Automatica*, vol. 81, pp. 270–278, 2017, ISSN: 00051098.

[96] L. Blanken, J. Willems, S. Koekebakker, and T. Oomen, "Design Techniques for Multivariable ILC: Application to an Industrial Flatbed Printer," *IFAC-PapersOnLine*, vol. 49, no. 21, pp. 213–221, 2016, ISSN: 24058963.

[97] H.-s. Ahn, Y. Chen, and K. L. Moore, "Iterative learning control : brief survey and categorization 1998 fffdfffdfffd 2004," *IEEE Control Systems*, vol. 37, no. 435, pp. 1–54, 2004.

[98] D. A. Bristow, T. Marina, and G. A. Andrew, "Survey of iterative learning control," *IEEE control systems magazine*, vol. 20, no. 9, pp. 961–966, 2006, ISSN: 10010920.

[99] A. Suguru, "A Brief History of Iteraative Learning Control," *Springer*, 1998.

[100] X. F. Li and J. X. Xu, "Lifted system framework for learning control with different trial lengths," *International Journal of Automation and Computing*, vol. 12, no. 3, pp. 273–280, 2015, ISSN: 17518520.

[101] Y. Liu and S. Liu, "An iterative learning control method for nonlinear systems with randomly varying trial lengths," *Proceedings of the 2015 27th Chinese Control and Decision Conference, CCDC 2015*, pp. 1100–1104, 2015.

[102] T. Seel, T. Schauer, and J. Raisch, "Iterative Learning Control for Variable Pass Length Systems," *The International Federation of Automatic Control*, 2011, ISSN: 00160032.

[103] D. Meng and K. L. Moore, "Robust iterative learning control for nonrepetitive uncertain systems," *IEEE Transactions on Automatic Control*, vol. 62, no. 2, pp. 907–913, 2017, ISSN: 00189286.

[104] W. He, T. Meng, X. He, and S. S. Ge, "Unified iterative learning control for flexible structures with input constraints," *Automatica*, vol. 96, pp. 326–336, 2018, ISSN: 00051098.

[105] A. Madady, "PID Type Iterative Learning Control with Optimal Gains," *International Journal of Control, Automation, and Systems*, vol. 6, no. 2, pp. 194–203, 2008, ISSN: 15986446.

[106] S. C. Burgess and A. C. Etoundi, "Performance maps for a bio-inspired robotic condylar hinge joint," *Journal of Mechanical Design, Transactions of the ASME*, vol. 136, no. 11, pp. 1–7, 2014, ISSN: 10500472.

[107] C. Semini, *HyQ - Design and Development of a Hydraulically Actuated Quadruped Robot*, April. P.hD. Thesis of University of Genoa, 2010, p. 210.

[108] C. Semini, N. G. Tsagarakis, E. Guglielmino, M. Focchi, F. Cannella, and D. G. Caldwell, "Design of HyQ -A hydraulically and electrically actuated quadruped robot," *Proceedings of the Institution of Mechanical Engineers. Part I: Journal of Systems and Control Engineering*, vol. 225, no. 6, pp. 831–849, 2011, ISSN: 20413041.

[109] P. De Leva, "Adjustments to zatsiorsky-seluyanov's segment inertia parameters," *Journal of Biomechanics*, vol. 29, no. 9, pp. 1223–1230, 1996, ISSN: 00219290. arXiv: 0021-92909600178-6.

[110] S. A. Gard and D. S. Childress, "The effect of pelvic list on the vertical displacement of the trunk during normal walking," *Gait and Posture*, vol. 5, no. 3, pp. 233–238, 1997, ISSN: 09666362.

[111] Keller. (2019). Keller pa-21y pressure transducer, [Online]. Available: http://www.keller-druck.com/home_e/paprod_e/21y_e.asp.

[112] ATI. (2019). Ati ip65/ip68 6 axis transducer, [Online]. Available: https://www.ati-ia.com/products/ft/ft_models.aspx?id=Omega160+IP65%2FIP68.

[113] B. Ding, A. Plummer, and P. Iravani, "A Study of a Compliant Hydraulic Actuator for Running Robots," *2018 Global Fluid Power Society PhD Symposium, GFPS 2018*, pp. 1–6, 2018.

[114] Blatchford. (2019). Echelon prosthesis, [Online]. Available: https://www.blatchford.co.uk/products/echelon/.

[115] M. Azad and R. Featherstone, "Modeling the contact between a rolling sphere and a compliant ground plane," in *Proceedings of the 2010 Australasian Conference on Robotics and Automation, ACRA 2010*, 2010, ISBN: 9780980740417.

Appendix

Mass matrix

The elements of Mass matrix $\mathbf{M(3 \times 3)}$ in Equation 6.3 is described.

$$\begin{aligned} M(1,1) = I_1 + I_2 + g_1^2 m_1 + g_2^2 m_2 + g_3^2 m_3 + l_1^2 m_2 + l_1^2 m_3 + l_2^2 m_3 \\ +2g_2 l_1 m_2 cos(\theta_2 + \theta_{c2}) + 2g_3 l_2 m_3 cos(\theta_3 + \theta_{c3}) + 2l_1 l_2 m_3 cos(\theta_2) \\ +2g_3 l_1 m_3 cos(\theta_2 + \theta_3 + \theta_{c3}) \end{aligned} \tag{9.1}$$

$$\begin{aligned} M(1,2) = m_2 g_2^2 + l_1 m_2 cos(\theta_2 + \theta_{c2}) g_2 + m_3 g_3^2 + 2m_3 cos(\theta_3 + \theta_{c3}) g_3 l_2 \\ +l_1 m_3 cos(\theta_2 + \theta_3 + \theta_{c3}) g_3 + m_3 l_2^2 + l_1 m_3 cos(\theta_2) l_2 + I_2 \end{aligned} \tag{9.2}$$

$$M(1,3) = g_3^2 m_3 + g_3 l_2 m_3 cos(\theta_3 + \theta_{c3}) + g_3 l_1 m_3 cos(\theta_2 + \theta_3 + \theta_{c3}) \tag{9.3}$$

$$\begin{aligned} M(2,1) = m_2 g_2^2 + l_1 m_2 cos(\theta_2 + \theta_{c2}) g_2 + m_3 g_3^2 + 2m_3 cos(\theta_3 + \theta_{c3}) g_3 l_2 \\ +l_1 m_3 cos(\theta_2 + \theta_3 + \theta_{c3}) g_3 + m_3 l_2^2 + l_1 m_3 cos(\theta_2) l_2 + I_2 \end{aligned} \tag{9.4}$$

$$M(2,2) = m_2 g_2^2 + m_3 g_3^2 + 2m_3 cos(\theta_3 + \theta_{c3}) g_3 l_2 + m_3 l_2^2 + I_2 \tag{9.5}$$

$$M(2,3) = m_3 g_3^2 + l_2 m_3 cos(\theta_3 + \theta_{c3}) g_3 \tag{9.6}$$

$$M(3,1) = g_3^2 m_3 + g_3 l_2 m_3 cos(\theta_3 + \theta_{c3}) + g_3 l_1 m_3 cos(\theta_2 + \theta_3 + \theta_{c3}) \tag{9.7}$$

$$M(3,2) = m_3 g_3^2 + l_2 m_3 cos(\theta_3 + \theta_{c3}) g_3 \tag{9.8}$$

$$M(3,3) = m_3 g_3^2 + I3 \tag{9.9}$$

In these equations, g_1, g_2 and g_3 are calculated from Equation 9.10. Also, θ_{c1}, θ_{c2} and θ_{c3} are calculated from Equation 9.11.

$$\begin{cases} g_1^2 = g_{11}^2 + g_{12}^2 \\ g_2^2 = g_{21}^2 + g_{32}^2 \\ g_3^2 = g_{31}^2 + g_{33}^2 \end{cases} \tag{9.10}$$

$$\begin{cases} \theta_{c1} = \arctan \frac{g_{12}}{g_{11} + \frac{l_1}{2}} \\ \theta_{c2} = \arctan \frac{g_{22}}{g_{21} + \frac{l_2}{2}} \\ \theta_{c3} = \arctan \frac{g_{32}}{g_{31} + \frac{l_3}{2}} \end{cases} \tag{9.11}$$

Centrifugal and coriolis term

Elements of Centrifugal and coriolis vector $\mathbf{C}\left(\mathbf{q}, \dot{\mathbf{q}}\right)$ in Equation 6.3 is defined below:

$$\begin{aligned} C(1) = \dot{\theta_2}^2 g_2 l_1 m_2 sin(\theta_2 + \theta c2) - g g_1 m_1 cos(\theta_1 + \theta_{c1}) - g l_1 m_2 cos(\theta_1) - g l_1 m_3 cos(\theta_1) \\ - g g_2 m_2 cos(\theta_1 + \theta_2 + \theta_{c2}) - g g_3 m_3 cos(\theta_1 + \theta_2 + \theta_3 + \theta_{c3}) + \dot{\theta_3}^2 g_3 l_2 m_3 sin(\theta_3 + \theta_{c3}) \\ + \dot{\theta_2}^2 l_1 l_2 m_3 sin(\theta_2) + \dot{\theta_2}^2 g_3 l_1 m_3 sin(\theta_2 + \theta_3 + \theta_{c3}) + \dot{\theta_3}^2 g_3 l_1 m_3 sin(\theta_2 + \theta_3 + \theta_{c3}) \\ + 2\dot{\theta_1}\dot{\theta_2} g_2 l_1 m_2 sin(\theta_2 + \theta_{c2}) + 2\dot{\theta_1}\dot{\theta_3} g_3 l_2 m_3 sin(\theta_3 + \theta_{c3}) + 2\dot{\theta_2}\dot{\theta_3} g_3 l_2 m_3 sin(\theta_3 + \theta_{c3}) + \\ 2\dot{\theta_1}\dot{\theta_2} l_1 l_2 m_3 sin(\theta_2) + 2\dot{\theta_1}\dot{\theta_2} g_3 l_1 m_3 sin(\theta_2 + \theta_3 + \theta_{c3}) + 2\dot{\theta_1}\dot{\theta_3} g_3 l_1 m_3 sin(\theta_2 + \theta_3 + \theta_{c3}) \\ + 2\dot{\theta_2}\dot{\theta_3} g_3 l_1 m_3 sin(\theta_2 + \theta_3 + \theta_{c3}) \end{aligned} \tag{9.12}$$

$$\begin{aligned} C(2) = \dot{\theta_3}^2 g_3 l_2 m_3 sin(\theta_3 + \theta_{c3}) - g l_2 m_3 cos(\theta_2 + \theta_3) - g g_2 m_2 cos(\theta_1 + \theta_2 + \theta_{c2}) \\ - \dot{\theta_1}^2 g_2 l_1 m_2 sin(\theta_2 + \theta_{c2}) - g g_3 m_3 cos(\theta_1 + \theta_2 + \theta_3 + \theta_{c3}) - \dot{\theta_1}^2 l_1 l_2 m_3 sin(\theta_2) \\ - \dot{\theta_1}^2 g_3 l_1 m_3 sin(\theta_2 + \theta_3 + \theta_{c3}) + 2\dot{\theta_1}\dot{\theta_3} g_3 l_2 m_3 sin(\theta_3 + \theta_{c3}) + 2\dot{\theta_2}\dot{\theta_3} g_3 l_2 m_3 sin(\theta_3 + \theta_{c3}) \end{aligned} \tag{9.13}$$

$$\begin{aligned} C(3) = - g g_3 m_3 cos(\theta_1 + \theta_2 + \theta_3 + \theta_{c3}) - g l_2 m_3 cos(\theta_2 + \theta_3) - \dot{\theta_1}^2 g_3 l_2 m_3 sin(\theta_3 + \theta_{c3}) \\ - \dot{\theta_2}^2 g_3 l_2 m_3 sin(\theta_3 + \theta_{c3}) - \dot{\theta_1}^2 g_3 l_1 m_3 sin(\theta_2 + \theta_3 + \theta_{c3}) - 2\dot{\theta_1}\dot{\theta_2} g_3 l_2 m_3 sin(\theta_3 + \theta_{c3}) \end{aligned} \tag{9.14}$$

Jacobian Matrix

The Jacobian matrix appears in Equation 5.23. S and C represent *sin* and *cos* respectively.

$$\mathbf{J} = \begin{bmatrix} J_{11} & J_{12} & J_{13} \\ J_{21} & J_{22} & J_{23} \\ J_{31} & J_{32} & J_{33} \end{bmatrix} \tag{9.15}$$

The elements of the matrix are shown below.

$$
\begin{aligned}
J_{11} &= -l_1 S(\theta_1) - l_2 S(\theta_1 + \theta_2) - l_3 S(\theta_1 + \theta_2 + \theta_3) \\
J_{12} &= -l_2 S(\theta_1 + \theta_2) - l_1 S(\theta_1 + \theta_2 + \theta_3) \\
J_{13} &= -l_1 S(\theta_1 + \theta_2 + \theta_3) \\
J_{21} &= l_1 C(\theta_1) + l_2 C(\theta_1 + \theta_2) + l_3 C(\theta_1 + \theta_2 + \theta_3) \\
J_{22} &= l_2 C(\theta_1 + \theta_2) + l_3 C(\theta_1 + \theta_2 + \theta_3) \\
J_{23} &= l_3 C(\theta_1 + \theta_2 + \theta_3) \\
J_{31} &= 1 \\
J_{32} &= 1 \\
J_{33} &= 1
\end{aligned}
$$